(U-Th)/He thermochronology of the Ottawa Embayment, Eastern Canada: the temperature-time history of an ancient, intracratonic rift basin

Rebecca Hardie

Supervisor: David Schneider, University of Ottawa

A thesis submitted to the Faculty of Graduate and Postdoctoral Studies in partial fulfillment of the requirements for the degree of
Master of Science in Earth Sciences

University of Ottawa
Ottawa, Canada
August 2016

Abstract

The Ottawa Embayment is a intracratonic rift basin that preserves a unique and eventful history through deep time. Its evolution records opening of the Iapetus Ocean with the break-up of Rodinia, followed by the formation of a continental passive margin, trapping siliciclastic sediments eroded from the adjacent Grenville Province. Samples were collected from a transect across the crystalline rift flank and through the embayment. We investigate the influence of crystallinitiy and non-ideal crystal chapes on He diffusion and resulting zircon (U-Th)/He age with the use of zircon (U-Th)/He thermochronometry, raman spectroscopy and x-ray micro-computed tomography. We then integrate our thermochronology data with regional geology to utilize multi-sample numerical modelling to improve our understanding of the thermal history of the Ottawa Embayment and the evolution of intracratonic rift basins. The works collected within defines a comprehensive temperature-time history for the basin and rift flank from the Late-Mesoproterozoic to present day.

Table of Contents

Acknowledgements

I would like to thank my supervisor, Dr. David A. Schneider, for the guidance, encouragement and advice he has provided throughout my time as his student. Thank you for introducing me to thermochronology and for providing the tools and the means to undertake this research. A special thanks goes out to Dr. John I. Garver (Union College) for his expertise, valuable comments and support throughout the course of this project. To Fred Gaidies (Carleton University) for his assistance with X-ray micro-tomography, Rebecca Flowers and James Metcalf (University of Colorado-Boulder) for their assistance with (U-Th)/He dating, Nancy Joyce and Dawn Kellett (Geological Survey of Canada) for their assistance with $^{40}Ar/^{39}Ar$ analysis, Dave Lowe (University of Ottawa) for his insight on the Potsdam Group, and Jeremy Powell (University of Ottawa) for thoughtful discussions and assistance with numerical modeling. Thanks to the Faculty of Graduate and Postdoctoral Studies and the Department of Earth and Environmental Science at the University of Ottawa. This work was supported by an NSERC Discovery grant to DAS and an AAPG Grants-in-Aid, Peter Warren Gester Memorial Grant to RAH. Finally, this work would not have been possible without the help and support from my friends and family. Thank you for providing an escape from my studies, and for helping to keep things in perspective.

(U-Th)/He thermochronology of the Ottawa Embayment, Eastern Canada: the temperature-time history of an ancient, intracratonic rift basin

R.A. Hardie[1], D.A. Schneider[1], J.I. Garver[2]
[1]*Department of Earth and Environmental Sciences, University of Ottawa, Canada*
[2]*Department of Geology, Union College, USA*

Abstract

The Ottawa Embayment is an intracratonic rift basin that preserves a unique and eventful history through deep time: the evolution records rifting and opening of the Iapetus Ocean during the break-up of Rodinia. Samples were collected from a 250 km long transect across the crystalline rift flank and through the sedimentary sequences of the embayment. We investigate the influence of zircon crystallinity and non-ideal crystal shapes on He diffusion and (U-Th)/He dates through the application of thermochronometry, Raman spectroscopy and x-ray micro-computed tomography. We integrate our thermochronology data with regional geology to utilize numerical modelling to improve our understanding of the thermal history of the Ottawa Embayment and the evolution of intracratonic rift basins. Our data show that detrital zircon have crystalline through upper transitional states with Raman peaks of 1007-1005.5 cm^{-1}, which are more retentive exhibiting a positive age-damage relationship, and lower transitional states with peaks <1005.5 cm^{-1} that are more diffusive with a negative age-damage relationship. The thermochronology defines a comprehensive temperature-time history for the rift flank and basin from the Late Mesoproterozoic to present day. The rift flank experienced a monotonic cooling history (0.1-2°C/m.y.) with little evidence of rifting in the cooling signature. Advancements in modelling have made it possible to simultaneously explore the unique pre- and post-basin fill histories of the basement and overlying sedimentary unit of the embayment. The basement of the embayment experienced a more complicated history, including Late

Neoproterozoic re-heating during rifting followed by rapid cooling during opening of the Iapetus Ocean at ca. 550. Progressive Cambro-Ordovician sedimentation into the basin (<1 km) was followed by minor re-heating during the Devonian, related to Acadian collision. Despite evidence on the southern portion of the embayment, the low temperature cooling histories do not record passage of the ca. 120 Ma Great Meteor hotspot.

Key words: Zircon (U-Th)/He, Thermochronology, Raman Spectroscopy, Ottawa Embayment.

Word count: ~11,600 body, ~17,000 paper total (body + references + captions), ~4, 300 Appendix total.

Table 1; Figures 11; supplementary files: Tables 5, Figures 8.

1. Introduction

The development of tensional forces in the Earth's lithosphere is a global tectonic phenomenon and when initiated in continental lithosphere, can propagate continental rifts (Olsen, 1995). Continental rift systems around the world have been extensively studied (e.g., Richardson and Arthur 1988; Macgregor 2015) and are known to develop rift basins, which can contain valuable economic resources. Rift basins are complex features that preserve important thermal overprinting and sedimentary sequences, providing valuable insight into the timing of distinct rift phases and the style of rifting from initiation to eventual continental breakup (e.g., Ebinger and Scholz 2011).

For this study, intracratonic rift basins are defined as those that form within stabilized continental masses as a primary result of extensional forces, resulting in a normal-fault bounded basin, floored by a paleo-rift structure in the axial zone (e.g., Schutz 1994; Songnian et al. 2002). The Ottawa Embayment of the St. Lawrence Rift System is an intracratonic rift basin related to the ca. 620-570 Ma opening of the Iapetus Ocean (Kumarapeli and Saull 1966; Keppie et al. 2001; Miller and Bar 2004), followed by the formation of the well-developed continental passive margin. Siliciclastic sediments eroded from the adjacent uplifted Neoproterozoic Grenville basement were trapped in the basin. As syn-rift and early post-rift sedimentary rocks are mostly non-fossiliferous, timing constraints for rift models must be based on radiometric dating.

Thermochronology has become a powerful and commonly used tool that continues to evolve with an expanding range of applications. It can provide information about the thermal history of a sample, which has implications for characterizing the tectonics of the

surrounding region. Unlike geochronology, it can be used to resolve both temporal and thermal aspects of geological processes (Reiners et al. 2005).

In an effort to resolve the thermal history of the Ottawa Embayment, we conducted apatite and zircon (U-Th)/He thermochronology integrated with single- and multi-sample numerical modeling across the exposed crystalline rift flank of the Grenville Laurentian Arch into the sedimentary sequence of the embayment. This investigation was conducted to improve our understanding of the evolution of intracratonic rift basins by resolving the timing and thermal evolution of the Ottawa-Bonnechere Graben (OBG) rift flank and the Ottawa Embayment. In (U-Th)/He dating, the shape, size, and internal radiation damage in grains affect the interpretation of resulting ages. During grain selection, we applied X-ray micro computed tomography and Raman spectroscopy to examine the effects of radiation damage and non-ideal crystal shapes on zircon He diffusion kinetics and resulting (U-Th)/He age for both detrital and crystalline samples.

Integrated with regional stratigraphic relationships, provenance studies and local geology, our data define a monotonic post-orogenic (Grenville) cooling history for the rift flank. A more complex thermal history for the embayment is illuminated with significant heating in the Ediacaran followed by a cooling phase before Cambrian sedimentation and minor heating in the Devonian.

2. Geological setting

2.1. Pre-rift history

The Grenville Province of eastern North America (**Figure 1**) is one of the largest Proterozoic orogenic belts in the world (Bell 1981) and is a result of a protracted sequence

of collisional events including the Ezleviran, Shawnigan, Ottawan and Rigolet phase, uniting Laurentia with another continent (likely Amazonia) from ca. 1300-1000 Ma. (Hoffman 1991; Carr et al. 2000; Cawood and Pisarevski 2006; Bickford et al. 2008 Li et al. 2008; Rivers 2008). The Grenville orogeny (Burke and Dewey 1973; Tollo et al. 2004) is associated with the assembly of the supercontinent Rodinia and culminated in peak amphibolite to granulite facies metamorphism (Rivers 2008). The Grenville Province in Canada is a broad and continuous segment of deformation belts, spanning ~300-400 km in width and extending ~3000 km northeastward from Lake Huron, along the St. Lawrence River to the coast of Labrador (Wynne-Edwards 1972; Davidson 1998).

The temporal and spatial scale of the orogen indicates that the Grenville was a large, hot and protracted orogeny (Rivers et al. 2010). Late orogenic collapse in the lower crust has been proposed for local regions of the orogen within Ontario and Québec (Culshaw et al. 1994; Martignole and Reynolds 1997; Ketcham et al. 1998; Schneider et al. 2013). Geochronologic investigations focusing on the post-orogenic thermotectonic history of the Grenville Province commonly associate their data with post-orogenic rifting and magmatic events along the margin of Laurentia (e.g., Kumarapeli et al. 1989; Kamo et al. 1995; Heizler and Harrison 1998; Cawood et al. 2001; O'Brien and van de Pluijm 2012). In southwestern Québec, Martignole and Reynolds (1997) conducted $^{40}Ar/^{39}Ar$ analyses on samples collected along a 400 km transect through the orogen to gain insight on the moderate temperature cooling history. Their study targeted all first order tectonic units, spanning the Grenville Front to the St. Lawrence Lowlands. The southernmost crustal block contains Mont-Tremblant, one of the tallest peaks in the southern Laurentians, and an important segment of our study area. $^{40}Ar/^{39}Ar$ hornblende cooling (T_c ~550°C) ages

from the region are ca. 1010 Ma, and Martignole and Reynolds (1997) determined that their data revealed distinct cooling histories for each tectonic terrane. Few published $^{40}Ar/^{39}Ar$ studies have been conducted in the region surrounding Mont-Tremblant and no low temperature thermochronologic data to date have been derived from the mountain.

In general, the Grenville Province is characterized by a complicated mosaic of asynchronous geological sub-belts, terranes and shear zones, divided by age and structural trends, recording the tectonic evolution of the Laurentian margin and supercontinent Rodinia (Wynne-Edwards 1972; Rivers 1997; Davidson 1998; Gower and Krogh 2002; Rivers et al. 2010).

2.2. Iapetan rifting and sedimentation

Extension and subsequent breakup of Rodinia resulted in the formation of the Pacific and Iapetus oceans, the latter of which formed as Amazonia rifted from Laurentia during a series of extensional events. The first major break up along the western margin of Laurentia may have occurred as early as ca. 750 Ma (Li et al. 2008). Nascent rifting between the Amazonia craton and the southeastern margin of Laurentia is proposed to have started at approximately the same time, but only resulted in continental break-up after ca. 600 Ma (Li et al. 2008). Consequently, two pulses of rifting have been suggested: the first was a minor event from ca. 760-700 Ma in the south and central Appalachians, and the second was a major event from ca. 620-550 Ma in the central to northern Appalachians (Aleinikoff et al. 1995; Cawood et al. 2001). It was during this time that the St. Lawrence rift system likely formed (**Figure 1**). The rift system is a NE-SW trending graben system, characterized by Late Proterozoic to Early Paleozoic mafic dikes and listric faults that roughly follow the northern shore of the St. Lawrence River (Kumarapeli 1985; Adams

and Basham 1989). The rift is still seismically active, with magnitude 5 earthquakes not uncommon (e.g., Ma and Audet 2014). The rift system represents a half-graben structure linking the Ottawa-Bonnechere and Saguenay grabens, two NW-SE trending structures, both interpreted as Late Proterozoic Iapetan failed arms of an RRR triple junction, possibly the Sutton Mountain triple junction (Kumarapeli et al. 1989). The aulacogen extends into the Grenville terrane, and initial rifting was likely induced by a mantle plume (Kumarapeli and Saull 1966; Burke and Dewey 1973; Kumarapeli 1985).

Emplacement of the 590 Ma Grenville dike swarm was parallel to the rifted continental margin and syntectonically with the development of the OBG (Kumarapeli and Isachsen 1991; Kumarapeli 1995). Structurally, the OBG acts as the central axis of the Ottawa Embayment and rift-related faults extend into the craton interior and mark the contact between the Cambro-Ordovician sedimentary rocks of the embayment and the Grenville Province to the northwest (Kumarapeli 1985; Gbadeyan and Dix 2013).

The Ottawa Embayment (**Figure 1**) is a WSW-ENE intracratonic rift basin bound on all sides by Precambrian arches, highland areas separating basinal or elevated areas, including: the Frontenac to the west, the Laurentian to the north and the Oka-Beauharnois to the east (Sanford and Arnott 2010). It is filled with siliciclastic rocks deposited in a rift to well-developed continental passive margin environment, followed by relatively- shallow water carbonates and then deep-water foreland basin deposits related to the Taconic orogeny, associated with the widespread epeiric sea on-lapping the basement (Sanford 1993; Sanford and Arnott 2010; Dix and Jolicoeur 2011; Gbadeyan and Dix 2013). The Precambrian basement is separated from the overlying Paleozoic sedimentary rocks by an erosional unconformity (Bernstein 1991; Sanford et al. 1993; Lavoie 1994).

The oldest Paleozoic sequence in the embayment is the Cambro-Ordovician Potsdam Group, which was deposited in a marginal marine environment. It consists of a 20-700 m thick unit of conglomerate and sandstone, spanning from the Frontenac Arch to eastern limit of the embayment. The group is proposed to be derived directly from the surrounding uplifted Precambrian terrane, transported into the region by fluvial processes (Wilson 1946; Sanford 1993; Sanford and Arnott 2010). The Potsdam is composed of three formations: the Late Neoproterozoic to Lower Cambrian Abbey Dawn and Covey Hill formations, consisting of non-marine conglomerate and sandstone with a combined thickness of up to ~600 m, and the Upper Cambrian to Lower Ordovician Nepean Formation, comprised of shallow marine quartz arenite with a thickness of up to ~110 m The three formations are not preserved in all areas along the length of the basin (Sanford 1993; Sanford and Arnott 2010).

The Lower to Upper Ordovician portion of the basin fill consists of Beekmantown Group sandstone and carbonate, and Ottawa Group carbonates and deep-water shales associated with westward transgression (Sanford and Arnott, 2010; Sanford 1993). The overall cumulative stratigraphic thickness within the basin is ~1 km (Sanford and Arnott 2010). The sedimentary units are intersected by steeply dipping normal faults likely belonging to a Late Proterozoic fracture system (Williams et al. 1995), perhaps reactivated from Late Neoproterozoic rifting and Ordovician to Devonian orogenic activity (Knight et al. 1995).

2.3. Syn- and post-Iapetan rifting events

A number of studies have used radiometric dating techniques to resolve and identify prevalent tectonothermal events and make local correlations within the region surrounding

our study area. Zircon U-Pb and fission track ages from the Potsdam Group and Grenville basement along the west, south and east sides of the Adirondack Mountains in New York provide information about the crystallization and thermal history of source rocks (Montario and Garver 2009). In their study, the U-Pb data identified a dominant 1200-950 Ma age population, supporting Grenville provenance of the Potsdam Group. Fission track ages yielded component populations of ca. 1200 Ma, 780 Ma and 540 Ma, predating deposition and possibly indicative of cooling of the Grenville source rock. The fission track ages do not indicate any widespread post-depositional heating that may have occurred in the Taconic (or other Appalachian) accretionary events, and thus these events were either too short lived or too cool to anneal fission tracks in zircon.

The St. Lawrence rift system and the Ottawa Embayment are lacking rock younger than Ordovician in age, consequently it is difficult to identify timing of post-Ordovician tectonism and fault movement. Numerous studies have proposed brittle faulting or fault reactivation episodes within the St. Lawrence rift system, which are relevant to, or may have had influence on, the study area. These include: (1) a Late Precambrian to Cambrian event, based on $^{40}Ar/^{39}Ar$ ages of pseudotachylytes from the Montmorency fault within Québec City, interpreted as timing of rifting and initial opening of the Iapetus Ocean (O'Brien and van de Pluijm 2012); (2) a Silurian to Early Devonian reactivation event, determined from K-Ar dating of clay rich gouge rock from the Montmorency, Saint-Laurent and Anse-aux-Vaches faults extending from Québec City to Charlevoix, Québec, interpreted as concurrent with subsidence of the nearby Appalachian foreland (Sasseville et al. 2012); and (3) a Triassic to Early Jurassic normal faulting event, based on apatite fission-track dating of hanging wall and footwall basement rocks of St. Lawrence and

Saguenay River faults (Tremblay et al. 2013). Roden-Tice et al. (2012) collected Grenville basement and Potsdam Group sandstone samples from transects across faults within the OBG for apatite fission track analysis and identified an Early Triassic to Middle Jurassic cooling event associated with unroofing of the graben and the absence of any Mesozoic fault reactivations.

The Mesozoic Great Meteor hotspot track lies northeast of the Ottawa Embayment and may have been an important regional Jura-Cretaceous thermal event. It has been traced through eastern North America by the documentation of kimberlites, plutons, and ultramafic intrusions. As the North American continent moved northwestward, the hotspot tracked across the embayment during the Late Jurassic to Early Cretaceous (Crough 1981; Sleep 1990; Heaman and Kjarsgaard 2000). Hotspots have been known to cause elevated geothermal gradients, dynamic uplift and exhumation over large region as asthenosphere replaces mantle lithosphere (e.g., Crough 1981; Taylor and Fitzgerald 2011). A few regional thermochronology studies have associated their data to the influence of the hotspot, including: (1) a heating event in the Early Cretaceous determined by apatite fission track (AFT) and (U-Th)/He ages within the eastern Adirondacks of northern New York, interpreted as a result of an elevated geothermal gradient with passing of the hotspot (Taylor and Fitzgerald 2011); (2) Early to Late Cretaceous AFT and (U-Th)/He ages from the Adirondacks in New York, Vermont, Massachusetts, Connecticut, and New Hampshire, interpreted to correspond to areas of thin lithosphere and remnant heating caused by passage of the hotspot (Roden-Tice and Tice 2005); and (3) Cretaceous cooling within the Northern Appalachians, determined from AFT ages of crystalline rocks from Vermont, New Hampshire and Maine, interpreted as a result of regional extension and

unroofing due to passing of the hotspot (Roden-Tice et al. 2009).

3. Sampling strategy and thermochronology methodology

A total of fifteen samples were collected along a ~250 km NE-SW transect, oblique to the axis of the rift, from Mont-Tremblant, Québec (~900 masl) through the central axis of the Paleozoic rift to Perth, Ontario, located within the St. Lawrence Lowlands (~65 masl; **Figure 2**). Samples of the crystalline basement and the Upper Cambrian to Lower Ordovician Nepean Formation of the Potsdam Group were collected from unaltered surface outcrops and road cut exposures that can be easily separated into two geologically defined regions: (1) the exposed crystalline rift flank; and (2) the Ottawa Embayment.

(1) Seven of the fifteen samples were collected along a 48 km NE-SW traverse spanning the exposed crystalline rift flank within the Laurentian Mountains, northwest of Montréal and within the Morin terrane of the Grenville Province (**Figure 2**). To assess age-elevation relationships, four of the seven basement samples (002RH, 003RH, 007RH, 012RH) were acquired along a 650 m vertical transect utilizing the natural relief of Mont-Tremblant for the development of a vertical profile. The top sample was collected at a elevation of 876 masl (002RH) and the base sample was collected at 234 masl (012RH), covering over 2400 m of horizontal distance. The remaining three samples were collected in the adjacent distal regions to the northeast (010RH) and southwest towards Papineauville, Québec (014RH and M_RH).

(2) Eight samples were collected at four locations along a 200 km NE-SW transect through the Ottawa Embayment, from Gatineau, Québec to Perth, Ontario (**Figure 1B** and **2**). Samples were collected at elevations from 130 masl to 65 masl across the northern edge

of the basin. The four sample locations consisted of outcrops with well-exposed and visible unconformities between the Precambrian crystalline rock and the overlying Cambro-Ordovician Nepean Formation of the Potsdam Group. The older Abbey Dawn and Covey Hill formations of the Potsdam Group were not present at these outcrops. Samples of the basement (01P, 02P, 03P, 04P) and the Nepean Formation (01S, 02S, 03S, 04S) were collected at each location (basement sample numbers are followed by "P," sedimentary sample numbers are followed with an "S").

Each sample was crushed with a jaw crusher and sieved to obtain a 106-150 μm size fraction. Samples were passed over a water table to obtain an initial heavy mineral fraction and further separated using acetone diluted methylene-iodide (MI, density 3.0 g/cm^3) and then washed with acetone and then water. More than 25 of the most pristine grains (with regards to shape and size, lack of inclusions, zoning, and fractures) of zircon and apatite were manually picked under a binocular microscope. Samples from the Mont-Tremblant rift flank transect were collected as an initial phase of the project and dated using zircon and apatite (U-Th)/He thermochronology. Samples from the Ottawa Embayment were collected during a second phase, and zircons from these samples, along with additional zircon from the peak (02RH) and base (012RH) samples of Mont-Tremblant, were analyzed and evaluated using X-ray micro-computed tomography (XR-μCT) and Raman spectroscopy before (U-Th)/He dating. Apatites from the embayment samples (when present) were also dated. To illuminate the moderate temperature-time (T-t) history to ~300°C, biotite was extracted from a number of the basement rift flank samples for $^{40}Ar/^{39}Ar$ geochronology.

$^{40}Ar/^{39}Ar$ analysis of four Mont-Tremblant samples yielded ages from 928 ± 4 Ma

to 977 ± 4 Ma, and this information will be utilized for our numerical models. Detailed $^{40}Ar/^{39}Ar$ methods and results are provided in the appendix.

4. Zircon and apatite (U-Th)/He thermochronology

The (U-Th)/He method utilizes the accumulation of radiogenic ^{4}He, produced through α-decay of the parent isotopes ^{238}U, ^{235}U and ^{232}Th; a negligible amount of ^{4}He is also produced through ^{147}Sm decay (Farley 2002; Harrison and Zeitler 2005). ^{4}He diffuses out of a mineral at a rate determined by the temperature and the diffusivity of the mineral. By measuring the parent/daughter isotopic ratios, the bulk cooling age, or the time at which a mineral passes through its closure temperature (T_c) can be determined (Dodson 1973). When minerals are at temperatures above their T_c, they behave as an open system with ^{4}He readily diffusing out, maintaining an effective cooling age of zero. As the mineral cools, ^{4}He retention gradually increases as the mineral passes through a broad range of temperatures, known as the helium partial retention zone (PRZ), eventually becoming a closed system with respect to ^{4}He diffusion (Wolf et al. 1998; Reiners and Brandon 2006). This study employs both the zircon and apatite (U-Th)/He systems, two low temperature thermochronometers that constrain the thermal histories of rock at depths of <10 and <4 km, respectively, assuming a geothermal gradient of 25-30°C/km (Ehlers and Farley 2003; Reiners 2005).

Zircon is abundant in a wide range of lithotypes and is resistant to physical and chemical weathering, making it an ideal thermochronometer (Reiners et al. 2004). It has a T_c of ~180°C and a PRZ range of ~130-200°C (Reiners 2002; Reiners et al. 2004; Stockli 2005; Wolfe and Stockli, 2010). Apatite is not as refractory as zircon, however it is

generally ubiquitous and possesses a lower T_c of ~70°C, and has a PRZ range of ~40-90°C (Wolf et al. 1996; Wolf et al. 1998; Farley 2000; Stockli 2000; Schuster et al. 2006; Flowers et al. 2009; Gautheron et al. 2009). The lower T_c of apatite in comparison to zircon, therefore, means apatite more readily susceptible to thermal resetting. T_c's are generally dependent upon the cooling rate, grain size and diffusivity, which is influenced by the accumulation of radiation damage. Samples can be fully reset with respect to radiogenic ^{4}He if reheated to temperatures exceeding the PRZ and partially reset, recording both the pre- and post-heating thermal history, if the minerals resided within the PRZ for a protracted period (Wolf et al. 1996; Farley 2000; Guenthner et al. 2015).

Thermochronology can be used to resolve both simple and complex T-t histories. Inference of a thermal history is easier for samples that have experienced monotonic cooling from high to low temperatures, and therefore passed only once through the PRZ and T_c. Whereas non-monotonic cooling histories are harder to recognize and interpret as they are defined by single or multiple reheating events causing partial or full resetting before the final phase of cooling (Reiners et al. 2005; Zhang 2008). Detrital thermochronology can be utilized by matching cooling ages preserved from forelands to those from the hinterland, to determine sediment provenance and the thermal history of the source terrain (Reiners and Brandon 2006). Partially reset grains from detrital samples are even more difficult to interpret. Detrital grains may share a common post-depositional thermal history, but have individual pre-depositional formation ages and histories. Each detrital zircon or apatite from a single sample could therefore possess a unique date and amount of inherited radiation damage (Guenthner et al. 2015).

(U-Th)/He thermochronology was conducted at the Thermochronology Research

and Instrumentation Laboratory (U-Th)/He facility at the University of Colorado in Boulder, USA. Five to eight zircon grains were analyzed using (U-Th)/He dating for each of the samples in this study. Twenty-four apatite grains (four to five per sample) were dated for samples collected along the rift flank transect and ten grains (five per sample) were dated for two samples from the Ottawa Embayment transect (01P and 01S). Details of analytical methods are provided in the appendix.

(U-Th)/He thermochronology employs individual grain analysis and each zircon age is reported as an alpha-ejection corrected age with uncertainties of ~8% (Reiners et al. 2004). Age accuracy is limited by broken, rounded or eroded grains, U-Th rich inclusions, the accuracy of microscope-based dimensional measurements and analytical error (Farley et al. 1996; Rahl et al. 2003; Reiners 2005; Evans et al. 2008). The alpha-ejection correction (F_T) is used to account for the effects of alpha-ejection and is traditionally determined quantitatively using ideal crystal dimensions (Farley 2002; Ketcham et al. 2011). This method may result in poorly estimated F_T values and consequently imprecise ages for detrital grains with non-ideal geometries. Therefore we used ultra-high resolution X-ray micro-computed tomography (XR-μCT) as a non-destructive technique to reconstruct 3D images to identify suitable grains and determine individual F_T corrections based on grain volume. The CT and traditional dimensional method of calculating F_T values were both used to assess and compare the precision of each technique in regards to non-ideal grain geometries. In general, the variation between XR-μCT and the microscope-based dimensional grain F_T values was ±1.32%. The (U-Th)/He ages reported in this study are corrected with the traditional dimensional F_T and detailed XR-μCT methods and results are provided in the appendix.

4.1. (U-Th)/He thermochronometry results for the rift flank

Single zircon (U-Th)/He ages are presented as a function of elevation (**Figure 3A**). Zircons derived from samples collected along the vertical traverse of Mont-Tremblant yield average (U-Th)/He ages that vary systematically with elevation (**Table 1** and **DR1** in the appendix), with maximum ages of 800 Ma at the top (876 masl) and 600 Ma at the base (234 masl) of the mountain transect. Although age averages can be effective at defining large-scale tectonic displacements, it is necessary to review the single grain ages within each sample. Individual zircon ages are plotted with respect to their respective effective uranium (eU) values (**Figure 3B** and **DR1** in the appendix), for samples from the vertical transect of the mountain, and those from the adjacent regions to the NE and SW along the rift flank. The eU is the concentration of the radioactive parent within a grain, which acts as a radation damage proxy. The dataset exhibits notable intra-sample age dispersion. Sample 02RH, from the highest elevation along the vertical transect of Mont-Tremblant, yielded individual zircon (U-Th)He ages ranging from 82 ± 7 Ma to 754 ± 60 Ma, with eU values from 106 to 1614 ppm. Sample 012RH, collected from the lowest elevation along Mont-Tremblant, yielded zircon ages from 218 ± 17 Ma to 603 ± 48 Ma, with eU values ranging from 136 to 373 ppm. Additionally, sample 010RH from the adjacent region northeast of Mont-Tremblant yielded zircon ages from 622 ± 50 Ma to 789 ± 63 Ma and samples 014RH and M_RH, southwest of Mont-Tremblant at elevations of ~215 masl, yielded similar ages from 274 ± 22 Ma to 567 ± 45 Ma. By comparing the age variations observed at different elevations to the age-eU distributions (**Figure 3B**), a negative relationship between eU concentration and zircon (U-Th)/He age is recognized to some degree for all samples. For individually plotted samples, refer to **Figure DR1** in the

appendix. No relationships are obvious between age and grain size for any samples.

The apatite (U-Th)/He data from the vertical transect also has observable single crystal age dispersion, with intra-sample age variation of as much as 145 m.y. (**Table 1** and **DR2** in the appendix). Mont-Tremblant mountain samples 02RH and 012RH yield apatite (U-Th)/He ages from 199 ± 19 Ma to 344 ± 28 Ma and from 152 ± 12 Ma to 280 ± 18 Ma, respectively. Sample M_RH, from the adjacent region to the southwest, yielded apatite He ages of 80 ± 6 Ma to 126 ± 10 Ma. The eU values for all the apatite grains analyzed were <70 ppm, and the apatite age dispersion shows a positive relationship with eU for samples 02RH, 07RH, 012RH and M_RH, whereas sample 03RH shows no obvious trend (**Figure DR2** in the appendix).

4.2. (U-Th)/He thermochronometry results for the Ottawa Embayment

Five to eight zircon grains were analyzed individually for each sample from the Ottawa Embayment transect. Zircon (U-Th)/He ages are plotted as a function of their respective eU values, revealing samples with both positive and negative age-eU correlations (**Figure 4A, B** and **DR1** in the appendix). Similar to those of the rift flank, the Ottawa Embayment samples all possess intra-sample age dispersion to some degree, which is not atypical for detrital samples with a wide range of single grain variation. Some samples have as much as 400 m.y. of intra-sample age dispersion, and for this reason we refrain from averaging our single crystal dates, which is commonly used to reduce age variability.

Detrital samples (01S, 02S, 03S, 04S) from the Nepean Formation of the Potsdam Group are composed of sediments derived from the adjacent Grenville Province (Montario and Garver 2009; Sanford 2010; Lowe personal communication, December 2015).

Consequently, we expect the detrital samples to have experienced a similar thermal history with those from the rift flank transect. Detrital zircons yield (U-Th)/He ages ranging from 229 ± 18 Ma to 698 ± 56 Ma and eU values from 12 to 382 ppm (**Table 1** and **DR1** in the appendix). When plotted as a function of eU, detrital samples reveal either positive or negative age-eU relationships (**Figure 4A**). However, for the Ottawa Embayment samples we also obtained Raman spectroscopy data (for $v_3(SiO_4)$ peak) (**Figure 5**). Raman spectroscopy provides a direct representation of radiation damage for individual grains, thus it is preferred as proxy for relative damage.

Basement samples (01P, 02P, 03P, 04P) from the embayment yield zircon (U-Th)/He ages from 176 ± 14 Ma to 579 ± 46 Ma (**Figure 4B**) with eU values from 68 to 470 ppm. The basement samples show a weakly negative relationship between (U-Th)/He age and eU, if at all. Samples 01P and 01S contained apatite with (U-Th)/He ages from 91 ± 12 Ma to 154 ± 22 Ma, and from 133 ± 17 Ma to 193 ± 15 Ma, respectively, with all eU values <73 ppm. Sample 01S shows a negative relationship between apatite (U-Th)/He age and eU, whereas 01P shows a weakly positive trend (**Figure DR2**). Overall, the majority of basement samples (those of the central and western embayment locations 02P, 03P, 04P) yield significantly younger ages than those of the unconformably overlying detrital samples (**Figure 4C**). Similar to the rift flank samples, those of the Ottawa Embayment show no obvious correlation between age and grain size. The cooling ages from the basement rocks of the Ottawa Embayment and from the overlying sedimentary cover show evidence of partial resetting to some degree and therefore the thermal evolution can be interpreted in the context of plate tectonics. Therefore, the basement may have experienced fuller resetting, which provides a unique opportunity to reveal the details of the complicated

thermal history. Detrital and basement samples from the most eastern location yield very similar zircon (U-Th)/He ages and for this reason likely experienced similar thermal histories.

5. Radiation damage and Raman spectroscopy

Zircon ($ZrSiO_4$) is a common accessory mineral in many rocks types with considerable stability against both physical and chemical weathering. It has a tetragonal structure consisting of edge sharing SiO_4 tetrahedrons and ZrO_8 dodecahedrons (Robinson et al. 1971; Klein and Dutrow 2008). Zircon incorporates uranium (U) and thorium (Th) in abundances from tens to thousands of ppm, as they can substitute for Zr^{4+} due to their similar ionic radii of ~1.00-1.05 Å (Shannon 1976). A single atom of ^{238}U decays to ^{206}Pb through chain decay and eight He atoms are ejected through the decay of U and Th, resulting in eight separate recoil events (Ellsworth et al. 1994). Over time, self-irradiation results in damage to the crystal lattice as alpha-particle ejection causes several hundred atomic displacements and parent recoil causes thousands of displacements within the lattice structure (Farnan and Salje 2001; Ketcham et al. 2013). Spontaneous fission events may also contribute to damage accumulation. Fission tracks are more destructive, but far less abundant than α-recoil events and have a higher annealing temperature of 240°C ± 30°C (Bernet and Garver 2005; Schuster and Farley 2009; Ketcham et al. 2013). When below the annealing temperature radiation damage can accumulate, transforming the zircon crystal into an amorphous, isotropic, metamict mineral, significantly disturbing the (U-Th)/He system (Holland and Gottfried 1955, Hurley et al. 1956, Nasdala et al. 2001, 2004; Reiners 2005; Shuster et al. 2006; Marsellos and Garver, 2009).

Radiation damage in zircon has commonly been presumed to alter diffusion kinetics and be the cause of poorly reproducible (U-Th)/He ages (Hurley 1952; Holland 1954, Hurley et al. 1956; Farley 2000; Nasdala 2004; Reiners 2005). One way to determine the degree of damage in zircon is by calculating the α-fluence, the time integrated self-irradiation dose, expressed as the number of α-decay events per gram. Guenthner et al. (2013) proposed that in zircons with low levels of damage ($<2 \times 10^{18}$ α/g), isolated radiation damage zones can form, acting as diffusion impediments and increasing the tortuosity of diffusion pathways, and therefore lowering diffusivity for He. At higher doses ($>2 \times 10^{18}$ α/g) damage surpasses a threshold, and allows for the interconnection of damage zones within the grain, forming fast diffusion pathways and consequently increasing diffusivity. Ketcham et al. (2013) suggests that the onset of damage interconnectivity and poor He retention may correlate with damage from spontaneous fission, as their calculations indicate that alpha recoil damage interconnectivity occurs at alpha-doses that are two orders of magnitude lower ($2.5\text{-}3.1 \times 10^{16}$ α/g). The degree of radiation damage can also be estimated by calculating the eU, which acts as a damage proxy. The eU is a parameter that weighs the decay of the two isotopes for their current α-particle productivity, calculated: $eU = U + 0.235 \bullet Th$ (Farley et al. 2011).

A more direct way of measuring the degree of radiation damage is with the use of Raman spectroscopy (Nasdala et al. 2005; Marsellos and Garver, 2010; Garver and Davidson 2015). Raman spectroscopy is a measure of the inelastic scattering of monochromatic light and reflects the crystalline structure of minerals. Because it is non-destructive, it has emerged as an important analytical tool that can be used to quantify lattice disorder caused by radiation damage. Radiation damage in zircon is assessed

through the measurement of the shifts in the frequencies of the v_1SiO_4 (~974 cm^{-1}) symmetric stretching band and the v_3SiO_4 (~1007 cm^{-1}) antisymmetric stretching band, and widening of the v_3SiO_4 peak (full width half maximum – FWHM; Nasdala et al. 2005).

For our study, high resolution Raman spectroscopy measurements were made with a Bruker Senterra μ-Raman spectrometer at Union College, Schenectady, USA. Sixty grains chosen from XR-μCT analysis were placed within a divot in a glass slide for analysis, oriented with their c-axis parallel to the microscope's N-S oriented crosshairs. The grains were each measured with two or more spot analyses using a 633 nm external He-Ne laser with a 2 μm diameter beam at 20 mV. Multiple spot measurements taken on each grain were averaged for analysis. A baseline correction was applied to the Raman frequency data and FitYK (Version 0.9.8; Wojdyr 2010), a curve fitting and data analysis program, was implemented for peak fitting of the $v_1(SiO_4)$ (~974 cm^{-1}) and $v_3(SiO_4)$ (~1007 cm^{-1}) bands, as well as for determination of the FWHM of both peaks.

5.1. Raman spectroscopy results

To place our study in the context of what is known about zircon crystallinity, it was necessary to define damage boundaries and zircon end members from the literature (e.g., Marsellos and Garver 2010). A perfect crystalline zircon has a $v_3(SiO_4)$ peak frequency of ~1007.5 cm^{-1}, whereas highly damaged and metamict zircons have peak frequencies of ~1000 to 955 cm^{-1} (Nasdala et al. 1995; 2004). We also identify two intermediate ranges, roughly based on annealing experiments conducted by Nasdala et al. (2004): crystalline, with peak frequencies of ~1006 cm^{-1} to 1005 cm^{-1} and transitional (partially disordered), with peak frequencies from ~1005 cm^{-1} to 1001 cm^{-1}.

The 60 zircon grains analyzed yielded Raman measurements extending from lower

transitional (with a few sub-metamict) to very crystalline, with a $v_3(SiO_4)$ peak frequency range of 1000.3 cm^{-1} to 1007.5 cm^{-1} and FWHM's from 2.54 cm^{-1} to 14.8 cm^{-1}. The $v_1(SiO_4)$ peak frequencies range from 974.3 cm^{-1} to 958.6 cm^{-1}, with FWHM's from 1.89 cm^{-1} to 88 cm^{-1} (**Table 1** and **DR3** in the appendix). For this study, we focus on measurements of the $v_3(SiO_4)$ antisymmetric stretching band and respective FWHM's, as it is the stronger raman signal. The average variance between single grain spot measurements was 0.29 for $v_3(SiO_4)$ peak frequencies, with a maximum of 2.97 and a minimum of 0. Significant differences in spot measurements may be indicative of crystal zoning (Marsellos and Garver 2010).

The detrital and basement zircon data for the Ottawa Embayment exhibits relationships typical of radiation damage and loss of crystallinity revealed by Raman spectroscopy. There is a distinct negative correlation between $v_3(SiO_4)$ peak position and their respective spectra line breadths (FWHM), and the detrital samples possess a strong negative correlation between eU and $v_3(SiO_4)$ peaks (**Figure 5** and **DR3** in appendix). As radiation damage increases, the $v_3(SiO_4)$ frequencies decrease and the FWHM increase, and detrital grains with higher U concentrations generally have more disorder (i.e., damage) than those with lower U concentrations. The basement zircons show a weak relationship, if at all, between eU concentration and $v_3(SiO_4)$ peak frequency.

The Raman $v_3(SiO_4)$ values for the individual grains of the Ottawa Embayment samples were plotted against their respective zircon (U-Th)/He date, along with eU (**Figure 6** and **DR4** in the appendix). Very-crystalline grains commonly yield unusually young ages in comparison to the crystalline-transitional grains of the same sample. The dataset reveals positive, negative and sometimes both types of correlations present within a single sample,

between zircon (U-Th)/He age and damage (represented by $v_3(SiO_4)$ peak). Three of the eleven samples (01S, 01P, M_RH) display generally strong positive relationships between radiation damage and age. Therefore, He retention increased with increasing damage. Five of the eleven samples (01S, 02S, 03S, 04S and 012RH), most of which are detrital, had a dominantly positive damage-age relationship within the crystalline Raman range, that then transitioned to a negative relationship within the transitional range (**Figure 6A, B**). Two samples (02P, 03P) yielded more complicated Raman signals with a weak negative relationship between radiation damage and (U-Th)/He date, if at all (**Figure 6C**). One sample from the top of Mont-Tremblant (02RH), has a strong negative relationship between radiation damage and (U-Th)/He date (**Figure 6D**).

In some cases, sample eU shows similar positive or negative damage-age relationships, as those displayed between their respective Raman $v_3(SiO_4)$ data and (U-Th)/He ages (**Figure 6B, D**). In contrast, other samples exhibit weakly similar relationships or none at all (**Figure 6A, C**). For detrital samples, this may be attributed to different provenance, and therefore varying damage accumulation over time between individual grains.

6. Numerical modeling with HeFTy

HeFTy (v 1.9; Ketcham 2015) is a modeling software with the purpose to aid in obtaining the maximum amount of thermal history information possible from thermochronometric data. It does so by generating possible thermal histories that best replicate the analytical data, constrained by a set of kinetic parameters and independent geologic information. Viable T-t paths are simulated individually for the sample(s) using

the inverse modeling capabilities of HeFTy. For this study, two helium diffusion models were implemented, including: the laboratory-derived radiation damage accumulation and annealing model (RDAAM) for apatite (Flowers et al. 2009) and the zircon radiation damage and annealing model (ZRDAAM) for zircon (Guenthner et al. 2013). After specifying independent geological T-t constraints, the HeFTy program uses a Monte Carlo approach to generate thousands of candidate T-t paths, classified as either "good" or "acceptable." The output paths are classified as either “good” or “acceptable” paths. Good paths correspond with unitless values of >0.5, with the connotation that the modeled and measured ages coincide (Ketcham, 2013).The goodness of fit measurements summarize the discrepancy between the observed and expected values for each model, with the intention to be good to the limit of statistical precision, defined so the mean of goodness of fit statistics assessed is 0.5 and the minimum is 1/(N+1), where N represents the statistical sample size (Ketcham, 2005). Acceptable paths have less congruent modeled and measured ages with values >0.05. In other words, a good T-t path implies that the path is supported by the data, whereas an acceptable T-t path is not ruled out by the data. Apatite and zircon (U-Th)/He thermochronometers are valuable for deciphering low temperature (<200°C) T-t histories and $^{40}Ar/^{39}Ar$ dating can record a simple account of cooling through deep time.

6.1. Inverse modeling of the rift flank

For this study, inverse models were run for all seven samples from Mont-Tremblant and the adjacent regions within the rift flank. Apatite and zircon (U-Th)/He data were utilized as the main inputs and each model was defined with identical simulation conditions. Pre-set, model T-t constraints were determined based on the timing of the Grenville Orogeny, consisting of peak temperature conditions of 790-700°C at ca. 1200-

1150 Ma (Indares and Martignole 1989; Storm and Spear 2005) and present day conditions with a surface temperature of 20°C. Two additional moderate temperature constraints were added as defined by $^{40}Ar/^{39}Ar$ dating. $^{40}Ar/^{39}Ar$ dating of biotite from our Mont-Tremblant samples defined a constraint of 250-350°C from ca. 970-920 Ma, and dating of hornblende from the surrounding region by Martignole and Reynolds (1997) defines a 450-550°C constraint from ca. 1050-1000 Ma. Two to three zircon and apatite (when available) grains were chosen with a range of single grain dates with eU values <300 ppm for each model, and therefore with relatively less accumulated radiation damage. For each sample model, 10,000 random T-t paths were simulated to resolve a range of viable histories.

6.1.1. Rift flank inverse modeling results

Viable "good" and "acceptable" T-t paths were detected for all seven samples from the rift flank (**Figure DR5** in the appendix). The seven inverse models yield viable T-t paths with a slight temperature variation, however there is a significant regional pattern that emerges and similarities between their thermal histories. Therefore, we present a single representative thermal model for the T-t history of the uplifted rift flank within the Grenville Province, adjacent to the Ottawa Embayment (**Figure 7**). The inverse models exhibit monotonic cooling and indicate that the area has not experienced sufficient re-heating (>200°C) to reset the zircon or apatite He systematics since Grenvillian metamorphism. Furthermore, the model paths for samples from the vertical transect do not reveal an inflection, which would represent a preserved partial retention zone. Overall, the good fit T-t paths defined using combined (U-Th)/He and $^{40}Ar/^{39}Ar$ data, can be highlighted by three phases of slow to moderate cooling through temperatures of the zircon PRZ and prolonged continuous cooling through the apatite PRZ. The three phases of cooling include

rates of 1 to 3°C/m.y. to reach temperatures of 250-350°C (1200 Ma to 750 Ma), then cooling rates of 0.3 to 1°C/m.y. to reach ~100°C (750 Ma to 350 Ma), and finally cooling of 0.1-0.3°C/m.y. (350 Ma to present).

6.2. Multi-sample inverse modeling of the Ottawa Embayment

Inverse models were created using the multi-sampling method for each of the four sample locations within the embayment (01, 02, 03, 04) (**Figure 8** and **9**), allowing for the basement and detrital models from the same location to have unique pre-basin fill thermal histories, but identical post-basin fill histories. Zircon (U-Th)/He data was utilized as the main constraint as only the most eastern of the four sample locations (location 01) contained datable apatite within their samples (01P, 01S). The basement samples from the central and western portion of the transect (02P, 03P, 04P) yield zircon (U-Th)/He ages that are significantly younger than those of the detrital samples at the same outcrop and have likely experienced a similar partial re-setting event. Therefore, the inverse models for those samples are defined by identical simulation conditions. As basement zircons are from the Grenville crystalline rock, and the Potsdam Group have a Grenville provenance (Montario and Garver 2009; Sanford 2010; Lowe personal communication, December 2015), all models were run with the same T-t constraints for conditions during Grenvillian times, consisting of peak temperatures of 790-700°C at ca. 1200-1150 Ma (Indares and Martignole 1989; Storm and Spear 2005). Additionally, they were all constrained to reach 20-30°C surface temperatures at some point between ca. 550-430 Ma to reflect basement exposure and subsequent deposition of the Nepean Formation of the Potsdam Group, and finally surface temperatures of 20°C for present day conditions. The models were set so the basement and detrital samples would have an unconformable stratigraphic relationship

and independent He and damage inheritance. Samples from the central and western portions of the transect experienced a partial resetting event that did not reach the easternmost sample location. Therefore models for the central and western locals had three additional constraints. Two pre-basin fill constraints were added to the basement samples: i) a broad constraint of 20-150°C from 1100-610 Ma to allow for cooling past the zircon PRZ before the opening of the Iapetus ca. 620-570 Ma (Kumarapeli and Saull 1966; Keppie et al. 2001; Miller and Bar 2004; O'Brien and van de Pluijm 2012); and ii) a 20-200°C constraint from 610-530 Ma, to permit only partial resetting due to heating during rifting. One post-basin fill constraint was applied to the basement and detrital samples at 20-150°C between 430-0 Ma. The constraint was applied to prevent any significant heating or partial resetting forced by the basement (U-Th)/He data, as the overlying detrital samples have not experienced fuller resetting. Models for the easternmost location were run with only the post-basin fill constraint used for all models.

One to two zircon grains were strategically chosen based on the Raman $v_3(SiO_4)$ peak frequency data for each sample, therefore each multi-sample model was run with data constraints from two to four grains. Zircon grains spanning the crystalline through transitional range of damage for each sample were chosen, when possible, to obtain a range of grain ages with varied accumulated damage. The very crystalline detrital grains were avoided as they commonly yield unusually young ages. Due to availability, two apatite grains were added to the multi-sample models for the eastern part of the embayment (location 01), as an additional low temperature constraint.

6.2.1. Multi-sample modeling results

Viable "good" and "acceptable" T-t paths were determined for all of the multi-

sample models for each location within the embayment (**Figure DR6** in the appendix). The multi-sample models allow for the basement and detrital models from the same location to have unique pre-basin fill thermal histories, but identical post-basin fill histories. The inverse models for all of the detrital samples from the embayment yield comparable viable T-t paths, whereas only the models for basement samples from the central and western portions of the transect (02, 03, 04) yield similar thermal histories. The inverse model for the easternmost basement sample (01P) reveals a slightly different thermal history as expected, for it yields dissimilar results compared to the other basement samples of the embayment. Therefore, we show a single representative multi-sample inverse model for both the central and western side (**Figure 8**) and another for the easternmost side of the embayment (**Figure 9**).

Comparable to inverse models of the rift flank, the detrital samples of the embayment yield independent pre-basin fill T-t paths characterized by slow to moderate rates (~0.7-2.5°C) of continuous cooling, between the Grenville orogeny and Cambro-Ordovician sedimentation. The basement of the central and western portions of the embayment is defined by a number of cooling phases. In the first, the basement experiences cooling to varying degrees below the zircon PRZ (<130°C) during the Tonian or Cryogenian of the Neoproterozoic. It then experiences heating to temperatures within the zircon PRZ (130-200°C), is partially reset by the Late Cryogenian or the Early Ediacaran, and remains within the PRZ until the end of the period or the Early Cambrian. The Cambrian is then dominated by moderate to rapid cooling (2-6°C/m.y) to surface temperatures (20-30°C) during the Cambro-Ordovician, coincident with timing of basement unroofing, surface exposure and subsequent basin filling. The easternmost

basement sample of the embayment, on the other hand (**Figure 9**), does not cool past the zircon PRZ until the very Late Ediacaran to Early Cambrian, and then cools to surface temperatures by the Cambro-Ordovician. Therefore, the easternmost basement does not experience partial resetting of the zircon (U-Th)/He system.

The post-basin fill thermal histories are similar for locations throughout the embayment. The thermal models show similar post-fill trends of heating to temperatures that exceed those expected for the estimated burial maximum of the basin during the Devonian, yet remain at temperatures below the zircon PRZ, preventing resetting. Maximum burial during the Devonian was <1 km (Sanford and Arnott 2010) and assuming a normal geothermal gradient, burial temperatures would not have surpassed 50°C. The Carboniferous and Late Permian thermal history is not well constrained, therefore, the timing at which the area began its final stage of progressive cooling to the present is unclear. Examining the multi-sample model of the easternmost location (**Figure 9**), the only inverse multi-sample model constrained with apatite data, it appears that there was no obvious heating during the Cretaceous.

7. Discussion

7.1. Relationship between zircon (U-Th)/He age and radiation damage, as revealed by Raman spectroscopy

Thermochronology can provide informative data to aid in understanding geological phenomena, however datasets can be unclear as they often possess intra-sample age dispersion that exceeds the general range of analytical error. Our zircon (U-Th)/He dataset yields varying degrees of intra-sample age dispersion and shows no obvious relationship

between age and grain size for any samples. Thus, radiation damage is likely the major control on He diffusivity for our study. Many researchers have studied the effects of high levels of radiation damage on He diffusion in zircon (e.g., Hurley 1952; Holland 1954; Nasdala et al. 2004) and an increasing number are investigating the effects of lower levels of damage (Reiners et al. 2005, Guenthner et al. 2013).

Rift flank samples from the Grenville crystalline basement have relatively high levels of radiation damage (40-1600 ppm) and exhibit negative age-eU correlations, whereas the Ottawa Embayment samples have low levels of radiation damage (determined by Raman spectroscopy) and corresponding eU (12-469 ppm) and can show either or both positive and negative age-damage correlations within a sample (**Figure 3** and **10**). We can therefore interpret that our low-damage samples behave differently and have dissimilar diffusion kinetics than our samples with relatively high levels of damage.

Guenther et al. (2013) showed that He diffusivity in zircon is affected by radiation damage in two markedly different ways, producing either positive or negative correlations, or both, between age and radiation damage. They suggest that zircons with low levels of damage ($<2 \times 10^{18}$ α/g) have isolated *damage zones* that retain helium and lower diffusivity, resulting in positive age-damage relationships. Those with high levels of damage ($>2 \times 10^{18}$ α/g) experience the interconnection of damage zones and thus serve as *fast diffusion pathways*, significantly increasing diffusivity and resulting in a negative age-damage correlation.

Our detrital samples from the Potsdam Group commonly show both positive and negative relationships between zircon (U-Th)/He age and radiation damage (represented by $v_3(SiO_4)$ peak frequency). However, the basement samples exhibit weak relationships,

if at all, between radiation damage (indicated by $v_3(SiO_4)$ peaks) and eU concentration, as well as between radiation damage and zircon (U-Th)/He ages. This may be a result of crystal zoning as Raman values were derived from outer crystal surface measurements, whereas the eU values are an integration of the entire grain. Therefore, if the basement grains are significantly zoned, the Raman values may not be directly or fully related to the measured eU (Garver; personal communication, April 2016). Non-formula elements like hafnium can also cause a slight shift in Raman frequency, and may also contribute to the weak relationships observed (Marsellos and Garver 2010).

The majority of the detrital samples have crystalline through upper transitional grains that exhibit positive and negative damage-age trends similar to those of the Guenthner et al. (2013) models. Grains with $v_3(SiO)_4$ peaks of ~1005-1007 cm^{-1} show a positive damage-age relationship as they become more retentive with increasing damage (**Figure 10B, C**) and lower transitional grains with peaks <1005.5 cm^{-1} are more diffusive and are either approaching the trend roll-over or are within the negative age-damage zone. A positive (retentive) to negative (diffusive) boundary would likely be more definable with samples that have grains spanning the whole range of damage from very crystalline to metamict (<1000 cm^{-1}). The most crystalline grains for each of our detrital samples ($v_3(SiO)_4$ peaks >1007 cm^{-1}) have exceptionally young ages. These unusually young ages may be as a result of high diffusivity solely along a defect free and ideal c-axis parallel channels within the grain, or varied detrital provenance.

7.2. Mont-Tremblant/rift flank thermal history

The (U-Th)/He data and numerical model results from the Mont-Tremblant region in western Québec, reveal the thermal history of the crystalline rift flank (**Figure 8**). Our

dataset defines a thermal history dominated by three phases of progressive cooling since orogeny (ca. 1200 Ma). This monotonic thermal history indicates that the area has not experienced any significant periods of burial, or other episodes of heating (such as the passage of the Mesozoic hotspot). Therefore, our data record cooling and progressive stabilization of the craton, and provides a background basement cooling history signal for the Ottawa Embayment data. Post-metamorphic cooling of the rift flank proceeded at a moderate rate of 1-3°C/m.y. until the mid-Neoproterozoic, when it reached temperatures of ~250-350°C. Cooling then slowed to a rate of 0.3 to 1°C/m.y., attaining ~100°C by the Carboniferous. The final phase of cooling through the Carboniferous to the present is defined by slow and uniform cooling rates of 0.1-0.3°C/m.y. The initial phase of post-orogenic cooling until the mid-Neoproterozoic may be related to regional stabilization, initiated by extensional orogenic collapse, as proposed for much of the Canadian Grenville Province (e.g., Culshaw et al. 1994; Matignole and Reynolds 1997; Ketcham et al. 1998; Schneider et al. 2013). Assuming an average geothermal gradient of 25°C/km, the initial phase of post-Grenville cooling until the mid-Neoproterozoic would be consistent with erosion rates of ~0.05 km/m.y., unroofing material to depths of ~15-25 km, which is in the expected range for active or decaying orogens (Reiners and Brandon 2006).

Continental rifts are commonly bounded by elevated flanks (e.g., MacPhee 2006; Mark et al. 2014). Currently, there are two main uplift mechanisms to explain the forces behind the uplift generated at these crustal thinning zones: active asthenospheric upwelling, as upwelling results in crustal doming (Cox 1989; Ziegler and Cloetingh 2004), and simultaneous rifting and uplift as a flexural isostatic response to unloading (Braun and Beaumont 1989; Mark et al. 2014). Therefore, identification of the mechanism behind

uplift can be determined by establishing the timing of uplift with respect to rifting (Mark et al. 2014). Rift flank uplift to some degree, would be expected with the opening of the Ottawa Embayment during Late Neoproterozoic rifting. However, our numerical models of the cooling data do not exhibit any punctuated periods of increased cooling after the mid-Neoproterozoic. Samples along the rift flank transect are ~80 to ~8 km northeast from the rift zone and the Ottawa Embayment. It has been proposed that uniform extension with induced mantle convection does not cause rift flank uplift for passive rifting, as commonly observed in many rifts (Landon and Coury 1994). However, it is surprising that even the closest samples to the embayment and the rift axis do not preserve a markedly different thermal history.

The main transect for our study passes across the projected track of the Mesozoic Great Meteor hotspot. As previously stated, hotspots may produce elevated geothermal gradients, dynamic uplift and consequent exhumation over a broad region (e.g., Crough 1981; Taylor and Fitzgerald 2011). Mantle plume magmatism associated with the continental portion of the track has included kimberlite magmatism, such as in the Kirkland Lake area in northeastern Ontario, and alkaline intrusions, like those of the Cretaceous Monteregian Hills in Québec (Foland et al. 1986; Heaman and Kjarsgaard 2000). The Monteregian Hills yield biotite and hornblende $^{40}Ar/^{39}Ar$ ages of ca. 124 Ma (Foland et al. 1986). The path of the hot spot is traced into the Atlantic margin where it is defined by the 1200 km long New England and Corner Seamounts (Foland et al. 1986). Although the hotspot has been associated with a number of low temperature thermochronology studies within the Adirondacks (e.g., Roden Tice et al. 2005; Taylor and Fitzgerald 2011) our rift flank models show continuous cooling throughout the Mesozoic and therefore neither the

cooling ages nor topography of the rift flank were influenced by the hotspot.

7.3. Thermal evolution of an intracratonic rift basin

7.3.1. Pre-basin fill thermal history

When modeled, all the Ottawa Embayment detrital samples, though not strongly controlled by constraints other than zircon (U-Th)/He data, yield similar pre-basin fill thermal histories as the adjacent Grenville basement of the rift flank. Each of the individual detrital models reveals similar histories of monotonic cooling from ca. 1200 Ma to the basin fill stage during the Cambro-Ordovician (**Figure 8 and 9**). The detrital samples experienced slow to moderate cooling with rates of 1-2°C/m.y. to reach temperatures of ~100-200°C by the end of the Tonian, at ca. 720 Ma, then slowly cooled to reach surface temperatures by the Cambro-Ordovician. The detrital samples have a similar monotonic cooling history as those of the rift flank, supported by their Grenville provenance. However, the detrital samples reached surface temperatures significantly earlier, as rift flank samples only reached surface temperatures during the Cretaceous-Cenozoic. Therefore, the inferred source of the detrital samples likely experienced cooling and exhumation earlier than the rocks currently exposed along the rift flank. The similarity between the zircon (U-Th)/He ages of the embayment detrital and the rift flank basement samples demonstrates that the detrital samples did not experience any significant re-heating and therefore partial resetting.

The zircon (U-Th)/He data from the basement samples of the central and western portion of the Ottawa Embayment primarily yield younger ages in comparison to the detrital samples of the overlying Potsdam from the same respective outcrop locations. Furthermore, the basement samples of the embayment do not preserve a monotonic post-

orogenic cooling history like those of the rift flank. Therefore, the basement samples have been heated to temperatures within the PRZ prior to the Cambrian, causing partial resetting before the basin fill stage. The (U-Th)/He data paired with independent geological constraints reveal a comprehensive post-orogenic, pre-basin fill thermal history. The basement of the central and western portion of embayment experienced post-orogenic cooling to some degree above the PRZ before the Ediacaran, thereby halting He diffusion and achieving a closed system. The basement was then heated to temperatures within the PRZ (likely to a minimum of ~150°C based on our models), causing partial resetting of the zircon grains by ca. 550 Ma. Viable T-t path envelopes reveal that the basement may have reached these temperatures at any point between ca. 750 Ma and 600 Ma, and then resided at temperature (>100°C) until ca. 550 Ma.

Structurally, the OBG acts as the central axis of the Ottawa Embayment, and both are characterized by rift-related normal faults (Kumarapeli 1985; Gbadeyan and Dix 2013). The presence of graben structures and fault blocks imply that the rift system was produced by passive continental rifting rather than active rifting (Scrutton 1982; Fitton 1983). Passive rifting is a result of far-field forces, like large-scale plate interactions, that initialize and drive lithospheric extension, with doming and volcanic activity as secondary syn-rifting processes (Cloetingh and Wortel 1986). The lithospheric extension leads to mechanical thinning of the crust and lithosphere, mantle upwelling and an increase in the geothermal gradient and surface heat flux, with possible localized high intensity thermal disturbances associated with igneous intrusions (McKenzie 1978; Ziegler 1993; Zellmer and Annen 2008). The numerical models for the central and western basement samples of the embayment yield potential T-t paths with heating and cooling episodes that may reflect

passive rifting related to the breakup of Rodinia.

We interpret that heating and partial resetting of the basement samples during the Ediacaran was not a result of significant burial, but due to an increase in the regional geothermal gradient and heat flux as a result of hot asthenosphere moving nearer to the surface with lithospheric extension. Magmatic intrusions during rifting may also have advected heat into the shallow crust. The basement models show some variance as to when heating begins, however all models show that the heating phase ceases by ca. 550 Ma, with the introduction of a cooling phase lasting until the basin fill stage in the Cambro-Ordovician. According to the McKenzie (1978) model, elevated temperatures during rifting in the region would have lowered the density of the lithosphere, allowing for some degree of isostatic uplift and erosion throughout the episode of heating. Additionally, lithospheric extension would have resulted in simultaneous fault controlled subsidence to some degree.

The timing of the heating and rifting phase revealed by our data is consistent with regional magmatism. Tholeittic dikes belonging to the Grenville dike swarm are parallel to faults related to the OBG and yield emplacement ages of ca. 590 Ma (Kumarapeli et al. 1989, Davidson et al. 1998). The dikes are proposed to have been emplaced syn-tectonically with the development of the graben, as a response to crustal uplift and lithospheric cracking coinciding with the onset of rifting (Kumarapeli et al. 1989; Campbell and Griffiths 1991). The trend of eastern North American dike swarms of Late Proterozoic age, including the Grenville Dike Swarm, converge at a RRR triple junction, east of the Ottawa Embayment and not far from Montréal, Québec, known as the Sutton Mountain triple junction (Burke and Dewey 1973; Kumarapeli et al. 1989). St. Seymour and

Kumarapeli (1995) have observed that the geochemistry of the Grenville dike swarm becomes increasingly plume-like closer to the Sutton Mountain triple junction.

The basement in the central and western portions of the Ottawa Embayment resided at temperatures within the PRZ until ca. 550 Ma, therefore indicating that there was ca. 50 m.y. of continued rifting and magmatism after emplacement of the Grenville dike swarm. This period of heating and rifting is consistent with the Tibbit Hill volcanism, which has been interpreted as the youngest Iapetan rift-related unit in the region, with an extrusion age of ca. 555 Ma (Kumarapeli et al. 1989; Abdel-Fattah et al. 1999). The Tibbit Hill Formation has been characterized as predominantly basaltic, with minor felsic and intermediate alkaline volcanic lithologies, and is likely a product of late rift volcanism at Sutton Mountain (Abdel-Fattah et al. 1999). The triple junction coincides with major positive gravity and magnetic anomalies, which Kumarapeli et al. (1981) have interpreted as an 8 km thick pile of the Tibbit Hill volcanic material, even though the Tibbit Hill Formation is restricted to a narrow exposure at surface. Puffer (2002) investigated the geochemistry of many eastern North American Late Neoproterozoic (Vendian) flood basalts and dikes swarms, including the Tibbit Hill volcanics and Grenville dike swarm. He concluded that magmatic occurrences from 615 to 564 Ma are consistent with early stages of deep mantle plume upwelling, followed by peak superplume magmatism at ca. 550 Ma. Based on our results, we invoke a ca. 550 Ma opening of the Iapetus Ocean. However paleomagnetic studies suggest that a well-developed Iapetus existed prior to 550 Ma rifting along eastern Laurentia (McCausland et al. 2011). Magmatic and paleomagnetic evidence for the paleogeography of Laurentia during the Ediacaran has been highly debated (Evans 1998; McCausland and Hodych 1998; Meert 1999; Cawood et al. 2001; Puffer

2002; Evans 2003; Hodych et al. 2004; McCausland et al. 2007; McCausland et al. 2011). Paleomagnetic data from rift related rocks along Laurentia's incipient Iapetan margin in Newfoundland and Québec suggests that the craton moved rapidly between 615 and 590 Ma, from low latitudes to the south pole, and then very rapidly northward (~27 cm/year) toward the equator between ca. 570 and ca. 550 Ma (McCausland and Hodych 1998; Cawood et al. 2001; Hodych et al. 2004; McCausland et al. 2007). This second phase of movement has been interpreted as rapid plate motion during the opening of the Iapetus (McCausland and Hodych 1998; Cawood et al. 2001). Cawood et al. (2001) explains the occurrence of ca. 550 Ma plume-related magmatism, after rapid plate movement and the breakup of Rodinia, as a result of continued rifting of marginal terranes into an already open Iapetus. McCausland et al. (2011) postulates that Laurentia remained at low latitudes throughout the Ediacaran, agreeing with the magmatic and geochemical evidence indicating that the margin of Laurentia remained stationary over a mantle plume from ca. 615 to 550 Ma (Puffer 2002).

Our models show that the easternmost portion of the basement of the Ottawa Embayment did not experience partial resetting to the same degree as the central and western locations as it did not cool to temperatures within the PRZ until ca. 550 Ma. This portion of the basement may have remained at warmer temperatures due to proximity to the Sutton Mountain triple junction and/or a deeper residency within the crust.

Overall, our data from the Ottawa Embayment supports that the detrital zircon in the Potsdam Group records a monotonic post-orogenic cooling history of the adjacent Grenville and that the Laurentian margin experienced a heating event during the Ediacaran concurrent with rifting and coincident with plume related magmatism until ca. 550 Ma

(Puffer 2002). The region then began to cool, indicating opening and exposure to the Iapetus Ocean at ca. 550 Ma (**Figure 11**). However, if paleomagnetic data are reliable, our data may be consistent with continued rifting of marginal terranes into an already open Iapetus as proposed by Cawood et al. (2001).

7.3.2. Basin fill to present day thermal history

As the basin fill stage of the embayment commenced at ca. 475 Ma, our detrital samples from the Nepean formation of the Potsdam Group are therefore an early post-rift sedimentary sequence, deposited while the Ottawa Embayment was facing the Iapetus Ocean. The basal Abbey Dawn and Covey Hill formations, deposited below the Nepean farther south in the embayment, therefore were likely deposited in a syn-rift environment. The Potsdam was overlain by lower to upper Ordovician carbonates and shales associated with the transgressive Epeiric Sea and the cumulative stratigraphic thickness of the embayment was ~1 km (Sanford and Arnott, 2010). The Iapetus closed during the Ordovician with progressive series of terrane accretions between Laurentia and Gondwana during the Appalachian orogeny (e.g., van Staal and Barr 2012), which is separated into four phases known as the Taconic, Salinic, Acadian and Alleghenian (Bird and Dewey 1970). The Taconic occurred during the Ordovician to Early Silurian, and Montario and Garver (2010) report no evidence of a regional Taconic heating event based on their zircon fission work in the Adirondacks south of the embayment. The results from our study are equivocal for the Ordovician-Silurian transition as our numerical models show a wide range of possible temperature conditions within the embayment during this time (**Figure 8** and **9**).

Our models show similar trends of heating during the Devonian to temperatures

that exceed those expected for the estimated burial maximum of the Ottawa Embayment (~1 km, Sanford and Arnott 2010) yet remain cooler than the zircon PRZ**.** Heating in the region may be a result of unaccounted for burial, an elevated geothermal gradient, and hydrothermal fluids from orogenic activity along the Laurentian margin associated with the Acadian orogeny (Bird and Dewey 1970). An elevated geothermal gradient during this time is evinced in the dolomitization of the carbonates sequences of the OBG. Nurkhanuly (2012) combined fluid inclusion and isotope data to determine that dolomitization was a result of hot (87-115°C) brines that interacted with siliciclastic strata or Precambrian gneissic rocks. The investigation suggests that the alteration may have occurred during Acadian orogenesis and with an elevated geothermal gradient of ~56°C/km, agreeable to our thermal models.

As the OBG is the structural axis of the Ottawa Embayment, the basin may have remained tectonically unstable after the post-Carboniferous time, with episodes of small-scale fault reactivations, like those observed elsewhere within the St. Lawrence Rift System (e.g., Sasseville et al. 2012). However, our sample network is not dense enough nor our models finely resolved enough to suggest fault reactivations during the post-Carboniferous. Additionally, based on the thermal history defined by our data for the eastern portion of the embayment, there is no strong evidence of any influence of the ca. 120 Ma Great Meteor hotspot on the cooling paths within the Ottawa Embayment.

8. Conclusions

1. We used zircon and apatite (U-Th)/He thermochronometry along with Raman spectroscopy and additional geological constraints to resolve the timing and thermal

evolution of the Ottawa-Bonnechere graben rift flank and the Ottawa Embayment, an intracratonic rift basin.

2. Zircon and apatite (U-Th)/He dating along a vertical transect of Mont-Tremblant was conducted to evaluate the temperature-time history of the crystalline rift flank. Cooling defined by our data correspond with moderate post-Grenvillian (Neoproterozoic) cooling (1-2°C/m.y.) and exhumation of the orogen before rifting and passive margin formation and subsequent slow and protracted cooling (0.3-0.1°C/m.y.) to present. The area has not experienced sufficient heating (>200°C) to reset the zircon He systematics. Neither the cooling ages nor topography were influenced by the passage of the Cretaceous Great Meteor hotspot.

3. Zircon (U-Th)/He data from the crystalline Grenville basement samples of the Ottawa Embayment primarily yield significantly younger ages in relation to those of the detrital samples from the overlying Cambro-Ordovician Potsdam Group at the same respective outcrop locations. The younger ages of the basement may indicate partial resetting followed by rapid subsidence and cooling before the basin fill stage (ca. 475 Ma), likely due to higher heat flow as a result of syn-rift crustal thinning with asthenospheric upwelling and intrusion of the Grenville dike swarm. Thermal models for the embayment show similar trends of heating during the Devonian that may be a result of burial, an elevated geothermal gradient, and hydrothermal fluids as a result of orogenic activity along the Laurentian margin associated with the Acadian orogeny. The embayment may have remained tectonically unstable from the post-Carboniferous, with episodes of small-scale fault reactivation, however the cooling ages have not been affected by these, nor by the ca. 120 Ma Great Meteor hotspot.

4. Rift flank samples from the Grenville crystalline basement have relatively high levels of radiation damage and exhibit negative age-eU correlations, whereas the Ottawa Embayment samples have low levels of radiation damage and can exhibit positive and negative age-damage correlations. The detrital samples show both positive and negative age-damage trends possibly as a consequence of the two ways radiation damage impacts He diffusion in zircon, supporting the Guenther et al. (2013) damage diffusivity relationship. Detrital crystalline through upper transitional grains with peaks 1007-1005.5 cm^{-1} are more retentive with a positive age-damage relationship, and lower transitional grains with peaks <1005.5 cm^{-1} are more diffusive and are either approaching the trend turn-over or are within negative age-damage zone.

References

Abdel-Fattah, M.; Abdel-Rahman, and Kumarapeli, S. P. 1999. Geochemistry and petrogenesis of the Tibbit Hill Metavolcanic Suite of the Appalachain Fold Belt, Quebec-Vermont: A plume-related and fractionated assemblage. *Am. J. Sci.* 299:210-237.

Adams, J.; and Basham, P. 1989. The seismicity and seismotectonics of Canada east of the Cordillera. *Geoscience Canada*. 16:3-16.

Bell, K. 1981. Will the real Grenville Orogeny please stand up. *Nature.* 290:89-90.

Bernet, M.; and Garver, J. I. 2005. Fission-track analysis of detrital zircon. *Rev. Mineral. Geochem.* 58:205-238.

Bernstein, L. 1991. The Lower Ordovician Beekmantown Group, Québec and Ontario. PhD thesis, Université de Montréal, Montréal, Canada. 330 p.

Bickford, M. E.; McLelland, J. M.; Selleck, B. W.; Hill, B. M.; and Heumann, M. J. 2008. Timing of anatexis in the eastern Adirondack Highlands: implications for tectonic evolution during ca. 1050 Ma Ottawan orogenesis. *Geol. Soc. Am. Bull.* 120:950-961.

Bleeker, W.; Dix, G.; Davidson, T.; and Lechneminant, T. 2011. Tectonic evolution and sedimentary record of the Ottawa-Bonnchere Graben: examining the Precambrian and Phanerozoic history of magmatic activity, faulting and sedimentation. Field trip guidebook, *Geological Association of Canada - Mineralogical Association of Canada*.

Braun, J.; and Beaumont, C. 1989. A physical explanation of the relation between flank uplifts and the breakup unconformity at rifted continental margins. *Geology.* 17:760-764.

Campbell, I. H.; and Griffiths, R. W. 1991. Megaplumes and giant radiating dyke swarms. Program with Abstracts, Annual Meeting, *Geological Association of Canada - Mineralogical Association of Canada*, Toronto. 16: A19.

Carr, S. D.; Easton, R. M.; Jamieson, R. A.; and Culshaw, N. G. 2000. Geologic transect across the Grenville orogeny of Ontario and New York. *Can. J. Earth. Sci*. 37:193-216.

Cawood, P. A.; McCausland, P. J. A.; and Dunning, G.R., 2001. Openin Iapetus: Constraints from the Laurentian margin in Newfoundland. *Geol. Soc. Am. Bull.* 113:4 443-453.

Cawood, P. A.; and Pisarevsky, S.A. 2006. Was Baltica right-way-up or upside-down in the Neoproterozoic? *J. Geol. Soc. London* 163:753-759.

Cloetingh, S.; and Wortel, R. 1986. Stress in the Indo-Australian plate. *Tectonophysics.* 132:49-67.

Cox, K. 1989. The role of mantle plumes in the development of continental drainage pattern. *Nature*. 342:873-877.

Crough, S. 1981. Mesozoic hotspot epeirogeny in eastern North America. *Geology*. 9:2-6.

Culshaw, N.; Ketchum, J.; Wodicka, N.; and Wallace, P. 1994. Deep crustal ductile extension following thrusting in the southwestern Grenville Province, Ontario. *Can. J. Earth. Sci.* 31:160-175.

Dahl, P. S.; Pomfrey, M. E.; and Foland, K. A. 2004. Slow cooling and apparent tilting of the Adirondack Lowlands, Grenville Province, New York, based on $^{40}Ar/^{39}Ar$ ages *Geol. Soc. Am. Mem*. 197:299-323.

Davidson, A. 1998. An overview of Grenville Province geology, Canadian Sheild, in *Geology of the Precambrian Superior and Grenville provinces and Precambrian fossils in North America*, edited by Lucas, S. B.; St-Onge, M. R. 207-270 p. Geological Survey of Canada, Geology of Canada, no. 7.

Burke, K. C. A.; and Dewey, J. F. 1973. Hot spots and continental breakup: implications

for collisional orogeny. *Geology.* 2:57-60.

Dodson, M. H. 1973. Closure temperature in cooling geo- chronological and petrological systems. *Contrib. Mineral. Petr*. 40:259-274.

Ebinger, C; and C. A. Scholz. 2011. Continental rift basins: An East African perspective, in *Sedimentary Basins:Recent Advances,* edited by Busby, C.; and Azor, A. 656 p. John Wiley & Sons, Ltd, Chichester, UK.

Ehlers, T. A.; and Farley, K. A. 2003. Apatite (U-Th)/He thermochronometry: methods and applications to problems in tectonic and surface processes. *Earth. Planet. Sci. Lett*. 206:1-14.

Ellsworth, S.; Navrotsky, A.; and Ewing, R.C. 1994. Energetics of radiation damage in natural zircon ($ZrSiO_4$). *Phys. Chem. Miner.* 21:140-149.

Evans, D. A. D. 1998. True polar wander, a supercontinental legacy. *Earth Planet. Sci. Lett*. 157:1-8.

Evans, D. A. D. 2003. True polar wander and supercontinents. *Tectonophysics*. 362:303-320.

Evans, N. J.; McInnes, I. A.; Squelch, A. P.; Austin, P. J.; McDonald, B. J.; and Wu, Q. 2008. Application of X-ray micro-computed tomography in (U-Th)/He thermochronology. *Chem. Geol*. 257:101-113.

Farley, K. A.; Wolf, R. A.; and Silver, L. T. 1996. The effects of long alpha-stopping distances on (U-Th)/He dates. *Geochim. Cosmochim. Acta.* 60:4223-4230.

Farley, K. 2002. (U-Th)/He dating: techniques, calibrations, and applications. *Rev. Mineral. Geochem*. 47:819-844.

Farley K. A. 2000. Helium diffusion from apatite: general behavior as illustrated by Durango fluorapatite. *J. Geophys. Res.* 105:2903-2914.

Farley, K. A.; Shuster, D. L.; and Ketcham, R. A. 2011. U and Th zonation in apatite observed by laser ablation ICPMS, and implications for the (U-Th)/He system. *Geochim. Cosmochim. Acta.* 75:4515-4530.

Farnan, I.; and Salje, E. K. H. 2001. The degree and nature of radiation damage in zircon observed by ^{29}Si nuclear resonance. *J. Appl. Phys.* 89:2084-2090.

Fitton, J. G. 1983. Active versus passive continental rifting: evidence from the West African rift system. *Tectonophysics*. 94:473-481.

Flowers, R. M.; Ketcham, R. A.; Shuster, D. L.; and Farley, K. A. 2009. Apatite (U-

Th)/He thermochronometry using a radiation damage accumulation and annealing model. *Geochim. Cosmochim. Acta.* 73:2347-2365.

Foland, K. A.; Gilbert, L. S.; Sebring, C. A.; and Jiang-Feng, C. 1986. $^{40}Ar/^{39}Ar$ ages for plutons of the Monteregian Hills, Quebec: Evidence for a single episode of Cretaceous magmatism. *Geol. Soc. Am. Bull.* 97:966-974.

Gautheron, C.; Tassan-Got, L.; Barbarand, J.; and Pagel, M. 2009. Effect of alpha-damage annealing on apatite (U-Th)/He thermochronology. *Chem. Geol.* 266:157-170.

Garver, J. I.; and Davidson, C. M. 2015. Southwestern Laurentian Zircons in Upper Cretaceous Flysch of the Chugach-Prince William Terrane in Alaska. *Am. J. Sci.* 315:537-556.

Gbadeyan, R.; and Dix, G. 2013. The role of regional and local structure in a Late Ordovician (Edenian) foreland platform-to-basin succession inboard of the Taconic orogen, Central Canada. *Geosciences.* 3:216-239.

Gower, C.; and Krough, T. 2002. A U-Pb geochronolocial review of the Proterozoic history of the eastern Grenville Province. *Can. J. Earth. Sci.* 35:795-829.

Guenthner, W. R.; Reiners, P. W.; Ketcham, R. A.; Nasdala, L.; and Geister, G. 2013. Helium diffusion in natural zircon: radiation damage, anisotropy, and the interpretation of zircon (U-Th)/He thermochronology. *Am. J. Sci.* 313:145-198.

Guenthner, W. R.; Reiners, P. W.; DeCelles, P. G.; and Kendall, J. 2015. Sevier belt exhumation in central Utah constrained from complex zircon (U-Th)/He data sets: Radiation damage and He inheritance effects on partially reset detrital zircons. *Geol. Soc. Am. Bull.* 127:323-348.

Harrison, M. T.; and Zeitler, P. K. 2005. Fundamentals of noble gas thermochronometry. *Rev. Mineral. Geochem.* 58:123-149.

Heaman, L. M.; and Kjarsgaard, B. A. 2000. Timing of eastern North American kimberlite magmatism: continental extension of the Great Meteor hotspot track? *Earth Planet. Sci. Lett.* 178:253-268.

Heizler, M. T.; and Harrison, T. M. 1998. The thermal history of the New York basement determined from $^{40}Ar/^{39}Ar$ K-feldspar studies. *J. Geophys. Res*. 103:29795-29814.

Hodych, J. P.; Cox, R. A.; and Kosler, J. 2004. An equatorial Laurentia at 550 Ma confirmed by Grenvillian inherited zircons dated by LAM ICP-MS in the Skinner Cove volcanics of western Newfoundland: implications for inertial interchange true polar wander. *Precambrian Res.* 129:93-113.

Hoffman, P. F. 1991. Did the breakup of Laurentia turn Gondwana inside out? *Science.* 252:1409-1412.

Holland, H.D. 1954 Radiation damage and its use in age determination. In: *Nuclear Geology*. Edited by Faul, H. Wiley, New York, 175–179 p.

Holland, H. D.; and Gottfried, D. 1955. The effect of nuclear radiation on the structure of zircon. *Acta Crystallographica*. 8:291-300.

Hurley, P. M. 1952. Alpha ionization damage as a cause of low helium ratios. *Eos. T. Am. Geophys. Union* 33:174-183.

Hurley, P. M.; Larsen, E. S.; and Gottfried, D. 1956. Comparison of radiogenic helium and lead in zircon. *Geochim. Cosmochim. Acta.* 9:98-102.

Indares, A.; and Martignole, J. 1989. Metamorphic constraints on the tectonic evolution of the allochthonous monocyclic belt of the Grenville Province, western Quebec. *Can. J. Earth. Sci.* 27:371-386.

Kamo, S. L.; Krogh, T. E.; and Kumarapeli, P. S. 1995. Age of the Grenville dyke swarm, Ontario-Quebec: Implications for the timing of Iapetan rifting. *Can. J. Earth. Sci.* 32:273-280.

Keppie, J. D.; Dostal, J.; Ortega-Gutierrez, F.; and Lopez, R. 2001. A Grenvillian arc on the margin of Laurentia: Evidence from the southern Oaxacan Complex, southern Mexico. *Precambrian Res.* 112:165-181.

Ketchum, J. W. F.; Heaman, L. M.; Krogh, T. E.; Culshaw, N. G.; and Jamieson, R. A. 1998. Timing and thermal influence of late orogenic extension in the lower crust: a U-Pb geochronological study from the southwest Grenville orogen, Canada. *Precambrian Res*. 89:25-45.

Ketcham, R. A.; Gautheron, C.; and Tassan-Got, L. 2011. Accounting for long alpha-particle stopping distances in (U-Th-Sm)/He geochronology: Refinement of the baseline case. *Geochim. Cosmochim. Acta*. 75:7779-7791.

Ketcham, R. A.; Guenthner, W. R.; and Reiners, P. W. 2013. Geometric analysis of radiation damage connectivity in zircon, and its implications for helium diffusion. *Am. Mineral.*, 98:350-360.

Klein, C.; and Dutrow, B. 2008. Manual of Mineral Science. 23rd Ed. Wiley. Hoboken, N.J. 716 p.

Knight, I.; James, N. P.; and Williams, H. 1995. Cambrian-Ordovician carbonate sequence (Humber Zone), in *Geology of the Appalachian-Caladonian Orogen in Canada and Greenland (Ch2),* edited by Williams, H. 67-87 p. Geological Survey

of Canada, Geology of Canada, no. 6.

Kumarapeli, P. S.; and Saull, V.A. 1966. The St. Lawrence Valley System: a North American Equivalent of the East African Rift Valley System. *Can. J. Earth. Sci.* 3:639-658.

Kumarapeli, P. S.; Goodacre, A. K.; and Thomas, M. D. 1981. Gravity and magnetic anomalies of the Sutton Mountains region, Quebec and Vermont; Expressions of rift volcanics related to the opening of Iapetus. *Can. J. Earth. Sci.* 18-680-692.

Kumarapeli, P. S. 1985. Vestiges of Iapetan rifting in the craton of the Northern Appalachians. *Geosci. Can.* 12:54-59.

Kumarapeli, P.S.; Dunning, G. R.; Pinston, H.; and Shaver, J. 1989. Geochemistry and U-Pb zircon age of comenditic metafelsites of the Tibbit Hill Formation, Quebec Appalachians. *Can. J. Earth. Sci.* 26:1374-1383.

Landon, S. M.; and Coury, A.B. 1994. Interior rift basins. Am. Assoc. Petr. Geol. Mem. 59. 276 p.

Lavoie, D., 1994. Diachronous tectonic collapse of the Ordovician continental margin, eastern Canada: comparison between the Québec Reentrant and St. Lawrence Promontory. *Can. J. Earth. Sci.* 31:1309-1319.

Li, Z. X.; Bogdanova, S. V.; Collins, A. S.; Davidson, A.; De Waele, B.; Ernst, R. E.; Fitzsimons, I. C. W.; Fuck, R. A.; Gladkochub, D. P.; Jacobs, J.; Karlstrom, K. E.; Lu, S.; Natapov, L. M.; Pease, V.; Pisarevsky, S. A.; Thrane, K.; and Vernikovsky, V. 2008. Assembl, configuration, and break-up history of Rodinia: A synthesis. *Precambrian Res*. 160:179-210.

Lisker, F.; Ventura, B.; and Glasmacher, U. A. 2009. Apatite thermochronology in modern geology. Geological Society of London, Special Publications. 324:1-23.

Lowe D. G.; Arnott, R. W. C.; and Sanford, B. V. 2013. Before the Great North American Carbonate Bank: A Complex Cambrian-Lower Ordovician Transgressive History Recorded in Siliciclastic Strata of the Potsdam Group, Southwest Laurentia. AAPG Annual Convention and Exhibition, Pittsburgh, Pennsylvania, May 2013. #50859.

Ma, S.; and Audet, P. 2014. The 5.2 magnitude earthquake near Ladysmith, Quebec, 17 May 2013: implications for the seismotectonics of the Ottawa-Bonnechere Graben. *Can. J. Earth. Sci.* 51:439-451.

Macgregor, D. 2015. History of the development of the East African Rift System: A series of interpreted maps through time. *J. African Earth. Sci*. 101:232-252.

MacPhee, D. 2006. Exhumation, rift-flank uplift, and the thermal evolution of the Rwenzori Mountains determined by combines (U-Th)/He and U-Pb thermochronology. MSc thesis, Massachusetts Institute of Technology, Cambridge, USA. 38 p.

Mark, C.; Gupta, S.; Carter, A.; Mark, D.F.; Gautheron, C.; and Martin-Barajas, A. 2014. Rift flank uplift at the Gulf of California: Neo requirement for asthenospheric upwelling. *Geology.* 42:259-262.

Marsellos, A.; and Garver, J. 2010. Radiation damage and uranium concentration in zircon as assessed by Raman spectroscopy and neutron irradiation. *Am. Mineral*. 95:1192-1202.

Martignole, J., Reynolds, P., 1997. $^{40}Ar/^{39}Ar$ thermochronology along a western Quebec transect of the Grenville Province, Canada. *J. Metamorph. Geol* 15:283-296

McCausland, P. J. A.; and Hodych, J. P. 1998. Paleomagnetism of the 550 Ma Skinner Cove volcanics of western Newfoundland and the opening of the Iapetus Ocean. *Earth Planet. Sci. Lett*. 163:15-29.

McCausland, P. J. A.; van der Voo, R.; and Hall, C. M. 2007. Circum-Iapetus paleogeography of the Precambrian-Cambrian transition with a new paleomagnetic constraint from Laurentia. *Precambrian Res*. 156:125-152.

McCausland, P. J. A.; Hankard, R.; and van der Voo, R. 2011. Ediacaran paleogeography of Laurentia: Paleomagmatism and $^{40}Ar/^{39}Ar$ geochronology of the 583 Ma Basie des Moutons syenite, Quebec. *Precambrian Res.* 187:58-78.

Meert, J. G. 1999. A paleomagnetic analysis of Cambrian true polar wander. *Earth Planet. Sci. Lett*. 168:1310-144.

Miller, B. V.; and Barr, S. M. 2004. Metamorphosed gabbroic dikes related to the opening of the Iapetus Ocean at the St. Lawrence Promontory: Blair River Inlier, Nova Scotia, Canada. *J. Geol*. 112:277-288.

Montario, M. J.; and Garver, J. I. 2009. The thermal evolution of the Grenville Terrane revealed through U-Pb and Fission-Track analysis of detrital zircon from Cambro-Ordovician quartz arenites of the Potsdam and Galway Formations. *J. Geol.* 117:595-614.

Nasdala, L.; Irmer, G.; and Wolf, D. 1995. The degree of metmictization in zircon: a Raman spectroscopic study. *Eur. J. Mineral*. 7:471-478.

Nasdala, L.; Wenzel, M.; Vavra, G.; Irmer G.; Wenzel, T.; and Kober, B. 2001. Metamictisation of natural zircon: accumulation versus thermal annealing of radioactivity-induced damage. *Contrib. Mineral. Petr.* 141:125-144.

Nasdala, L.; Reiners P. W.; Garver, J. I.; Kennedy, A. K.; Stern, R. A.; Balan, E.; and Wirth, R. 2004. Incomplete retention of radiation damage in zircon from Sri Lanka. *Am. Mineral.* 89:219-231.

Nasdala, L.; Hanchar, J. M.; Kronz, A.; and Whitehouse, M. J. 2005. Long-term stability of alpha particle damage in natural zircon. *Chemical Geology*. 220:83–103.

Nurkhanuly, U. 2012. Structurally controlled hydrothermal dolomite, Eganville-Douglas Paleozoic outlier, Ottawa-Bonnechere Graben, Eastern Ontario. MSc thesis, Carleton University, Ottawa, Ontario. 98 p.

O'Brien, T. M.; and van der Pluijm, B. A. 2012. Timing of Iapetus Ocean rifting from Ar geochronology of pseudotachylytes in the St. Lawrence rift system of southern Quebec. *Geology*. 40:443-446.

Olsen, K. H. 1995. Continental Rifts: evolution, structure, tectonics. Elsevier. Amsterdam, the Netherlands. 463 p.

Rahl, J. M.; Reiners, P. W.; Campbell, I. H.; Ncolescu, S.; Allen, C. M. 2003. Combined cingle grain (U-Th)/He and U/Pb dating of detrital zircons from the Navajo Sandstone, Utah. *Geology.* 31:761-764.

Reiners, P. W. 2002. (U-Th)/He chronometry experiences a renaissance. *Earth and Space News.* 83:21-27.

Reiners, P. W.; Spell, T. L.; Nicolescu, S.; and Zanetti, K. A. 2004. Zircon (U-Th)/He thermochronometry: He diffusion and comparisons with $^{40}Ar/^{39}Ar$ dating. *Geochim. Cosmochim. Acta.* 68:1857-1887.

Reiners, P.; Ehlers, T.; and Zeitler, P. 2005. Past, present, and future of thermochronology. *Rev. Mineral. Geochem*. 58:1-18.

Reiners, P. W. 2005. Zircon (U-Th)/He thermochronometry. *Rev. Mineral. Geochem*. 58:151-179.

Reiners, P. W.; and M. T. Brandon. 2006. Using thermochronology to understand orogenic erosion, *Ann. Rev. Earth Planet. Sci. 34*:419-466.

Richardson, M.; and Arthur, M. A. 1988. The Gulf of Suez-northern Red Sea Neogene rift: a quantitative basin analysis. *Mar. Petrol. Geol*. 5:247-270.

Rivers, T. 1997. Lithotectonic elements of the Grenville Province: Review and tectonic implications. *Precambrian Res*. 86:117-154.

Rivers, T. 2008. Assembly and preservation of lower, mid, and upper orogenic crust in

the Grenville Province- Implications for the evolution of large hot long-duration orogens. *Precambrian Res*. 167:237-259.

Rivers, T.; Martignole, J.; Gower, C.; Davison, A. 2010. New tectonic divisions of the Grenville province, southeast Canadian Shield. *Tectonics*. 8:63-84.

Rivers, T. 2012. Upper-crustal orogenic lid and mid-crustal core complexes: signature of a collapsed orogenic plateau in the hinterland of the Grenville Province. *Can. J. Earth. Sci.* 49: 1-42.

Robinson, K.; Gibbs, G. V.; and Ribbe, P. H. 1971. The structure of zircon; a comparison with garnet. *Am. Mineral.* 56:782-790.

Roden-Tice, M. K.; and Tice, S. J. 2005. Regional-Scale Mid-Jurassic to Late Cretaceous Unroofing from the Adirondack Mountains through Central New England Based on Apatite Fission-Track and (U-Th)/He Thermochronology. *J. Geol.* 112:535-552.

Roden-Tice, M. K.; Tremblay, A.; Negrycz, K. M.; and Gamache, B. 2012. Mesozoic unroofing of the Ottawa-Bonnechere Graben, Ontario, based on apatite fission-track thermochronology. Geological Society of America Abstracts with Programs. 44:69.

Sanford, B. V. 1993. St. Lawrence Platform-Introduction: Chapter 10, in *Sedimentary Cover of the Craton in Canada*, edited by Stott, D. F.; and Aitken, J. D. Geological Survey of Canada, Geology of Canada 5. 709-722.

Sanford, B. V.; Arnott, R. W. C. 2009. Stratigraphic-structural sections across the Ottawa Embayment and the western segment of the Quebec Basin. Geological Survey of Canada, Geology of Canada 5. 711-722.

Sanford, B. V.; and Arnott, R. W. C. 2010. Stratigraphic and structural framework of the Potsdam Group in eastern Ontario, western Quebec, and northern New York State. Geological Survey of Canada Bulletin 597. 84 p.

Sasseville, C.; Clauer, N.; and Tremblay, A. 2012. Timing of fault reactivation in the upper crust of the St. Lawrence rift system, Canada, by K-Ar dating of illite-rich fault rocks. *Can. J. Earth. Sci.* 249:148-161.

Schneider, D. A.; Cope, N.; Holm, D. K. 2013. Thermochronology of the Mont Laurier terrane, southern Canadian Grenville Province, and its bearing on defining orogenic architecture. *Precambrian Res.* 226:43-58.

Schutz, K. I. 1994. Structure and stratigraphy of the Gulf of Suez, Egypt, in *Interior Rift Basins,* edited by Landon, S. M. American Association of Petroleum Geologists Memoir 59. 9-55.

Scrutton, R. A. 1982. Passive continental margin: A review of observations and mechanisms, in *Dynamics of passive margins,* edited by Scrutton, R. A. American Geophysical Union, Geological Society of America Geodynamics Series 6. 5-11.

Shannon, R. D. 1976. Revised ionic radii and systematic studies of interatomic distances in halides and chalcogenides. *Acta Crystallographica*. 32:751-767.

Shuster, D. L.; Flowers, R. M.; and Farley, K. A. 2006. The influence of natural radiation damage on helium kinetics in apatite. *Earth. Planet. Sci. Lett*. 249:148-161.

Sleep, N. H. 1990. Monteregian hotspot track: A long-lived mantle plume. *J. Geophys. Res.* 95:983-21.

Songnian, L.; Chunliang, Y.; Huaikun, L.; and Humin, Li. 2002. A group of rifting events in the terminal Paleoproterozoic in the North China Craton. *Gondwana Res*. 5:123-131.

Seymour, K. S.; Kumarapeli, P. 1995. Geochemistry of the Grenville Dyke Swarm: role of plume-source mantle in magma genesis. *P. Contr. Mineral. and Petrol.* 120:29.

Stockli, D.; Farley, K. A.; and Dumitru, T. 2000. Calibrations of the apatite (U-Th)/He thermochronometer on an exhumed fault clock, White Mountains California. *Geology*. 28:983-986.

Stockli, D. 2005. Application of Low-Temperature Thermochornometry to Extensional Tectonic Settings. *Rev. Mineral. Geochem*. 58:411-448.

Storm, L. C.; and Spear, F. S. 2005. Pressure, temperature and cooling rates of granulite facies migmatitic pelites from the southern Adirondack Highlands, New York. *J. Metamorph. Geol.* 23:107-130.

Taylor, J.; and Fitzgerald, P. 2011. Low-temperature thermal history and landscape development of the eastern Adirondack Mountauins, New-York: Constraints from apatite fission-track thermochronology and apatite (U-Th)/He dating. *Geol. Soc. Am. Bull.* 123:412-426.

Tollo, R. P.; Corriveau, L.; McLelland, J.; and Bartholomew, M. J. 2004. Proterozoic tectonic evolution of the Grenville orogen in North America: An introduction, *in Proterozoic Tectonic Evolution of the Grenville Orogen in North America*, edited by Tollo, R. P.; Corriveau, L.; McLelland, J.; and Bartholomew, M. J. *Geol. Soc. Am. Mem*. 197:299-323.

Tremblay, A.; Roden-Tice, M. K.; Brandt, J. A.; Megan, T. W. 2013. Mesozoic fault reactivation along the St. Lawrence rift system, eastern Canada: Thermochronologic evidence from apatite fission-track dating. *Geol. Soc. Am. Bull*. 125:794-810.

Williams, H.; Kumarapeli, P. S.; and Knight, I. 1995. Upper Precambrian-Lower Precambrian clastic sedimentary and volcanic rocks (Humber Zone), in *Geology of the Appalachian-Caledonian Orogen in Canada and Greenland*, edited by Williams, H. Geological Society of America, Geology of North America F-1. 61-67.

Wilson, A. E. 1946. Geology of the Ottawa-St. Lawrence Lowland, Ontario and Quebec. Geological Survey of Canada Memoir 241. 66 p.

Wojdyr, J. M. 2010. FitYK, Version 0.9.8. *J. Appl. Crystallogr*. 43:1126.

Wolf, R. A.; Farley K. A.; and Silver L.T. 1996. Helium diffusion and low-temperature thermochronometry of apatite. *Geochim. Cosmochim. Acta*. 60:4231-4240.

Wolf, R. A.; Farley, K. A.; and Kass, D.M. 1998. Modeling of the temperature sensitivity of the apatite (U-Th)/He thermochronometer. *Chem. Geol.* 148:105-114.

Wolfe, M. R.; Stockli, D. F. 2010. Zircon (U-Th)/He thermochronometry in the KTB drill hole, Germany, and its implications for bulk He diffusion kinetics in zircon. *Earth. Planet. Sci. Lett*. 295:69-82.

Wynne-Edwards, H. R. 1972. The Grenville Province. Geological Assocation of Canada Special Paper 11. 163-182.

Zhang, Y. 2008. Geochemical Kinetics. Princeton University Press, Princeton, NJ. 664 p.

Zellmer, G. F.; Annen, C. 2008. An introduction to magma dynamics, in *Dynamics of Crustal Magma Transfer, Storage and Differentation,* edited by Annen, C.; Zellmer, G. F. Geological Society of London, Special Publications 304. 1-13.

Ziegler, P. A. 1993. Plate moving mechanisms: their relative important. *J. Geol. Soc. London.* 150:927-940.

Ziegler, P. A.; and Cloetingh, S. 2004. Dynamic processes controlling evolution of rifted basins. *Earth-Sci. Rev.* 64:1-50.

Table 1: Summary of sample coordinates and results from this study

Sample	Location†	Elevation (m)	Rock Type	ZHe Age Range (Ma)	AHe Age Range (Ma)	V_3SiO_4 Range (cm^{-1})	mCT[a]
Mont-Tremblant Rift Flank							
02RH	534520, 5118677	876	quartzofeldspathic orthogneiss	82 ± 7 - 754 ± 60	199 ± 19 - 344 ± 45	1003.0 - 1006.0	Y
03RH	533757, 5118357	654	quartzofeldspathic orthogneiss	190 ±15 - 730 ± 58	180 ± 16 - 323 ± 50	—	—
07RH	532966, 5118101	333	quartzofeldspathic orthogneiss	361 ± 29 - 532 ± 43	168 ± 20 - 354 ± 35	—	—
010RH	554095, 5130882	234	quartz monzonite	622 ± 50 - 789 ± 63	—	—	—
012RH	531679, 5117146	228	quartzofeldspathic orthogneiss	218 ± 17 - 603 ± 48	152 ± 17 - 279 ± 21	1005.0 - 1006.3	Y
014RH	516396, 5092503	553	granite	274 ± 22 - 567 ± 45	—	—	—
M_RH	497684, 5055405	205	amphibolite	335 ± 27 - 542 ± 43	80 ± 16 - 126 ± 11	1005.0 - 1005.7	—
Ottawa Embayment - *Grenville Basement*							
01P	466714, 5043139	75	muscovite-biotite meta-granite	478 ± 38 - 555 ± 44	91 ± 12 - 154 ± 22	1005.0 -1006.5	Y
02P	451413, 5036866	68	biotite granitic gneiss	232 ± 19 - 532 ± 43	—	1003.5 - 1007.0	Y
03P	446258, 5038386	65	biotite meta-granite	176 ± 14 - 401 ± 32	—	1001.3 - 1006.0	Y
04P	405509, 4969027	130	garnet-biotite meta -granite to gneiss	183 ± 15 - 579 ± 46	—	1004.1 - 1006.4	Y
Ottawa Embayment - *Detrital*							
01S	466714, 5043139	75	quartz arenite	229 ± 18 - 520 ± 42	133 ± 17 - 193 ±15	1005.5 - 1007.1	Y
02S	451413, 5036866	68	quartz arenite	302 ± 29 - 672 ± 54	—	1001.8 - 1006.7	Y
03S	446258, 5038386	65	quartz arenite	256 ± 20 - 613 ± 49	—	1005.3 - 1007.2	Y
04S	405509, 4969027	130	quartz arenite	503 ± 40 - 698 ± 56	—	1005.5 - 1007.5	Y

† UTM zone 18T; [a:] Y = mCT analysis conducted on sample

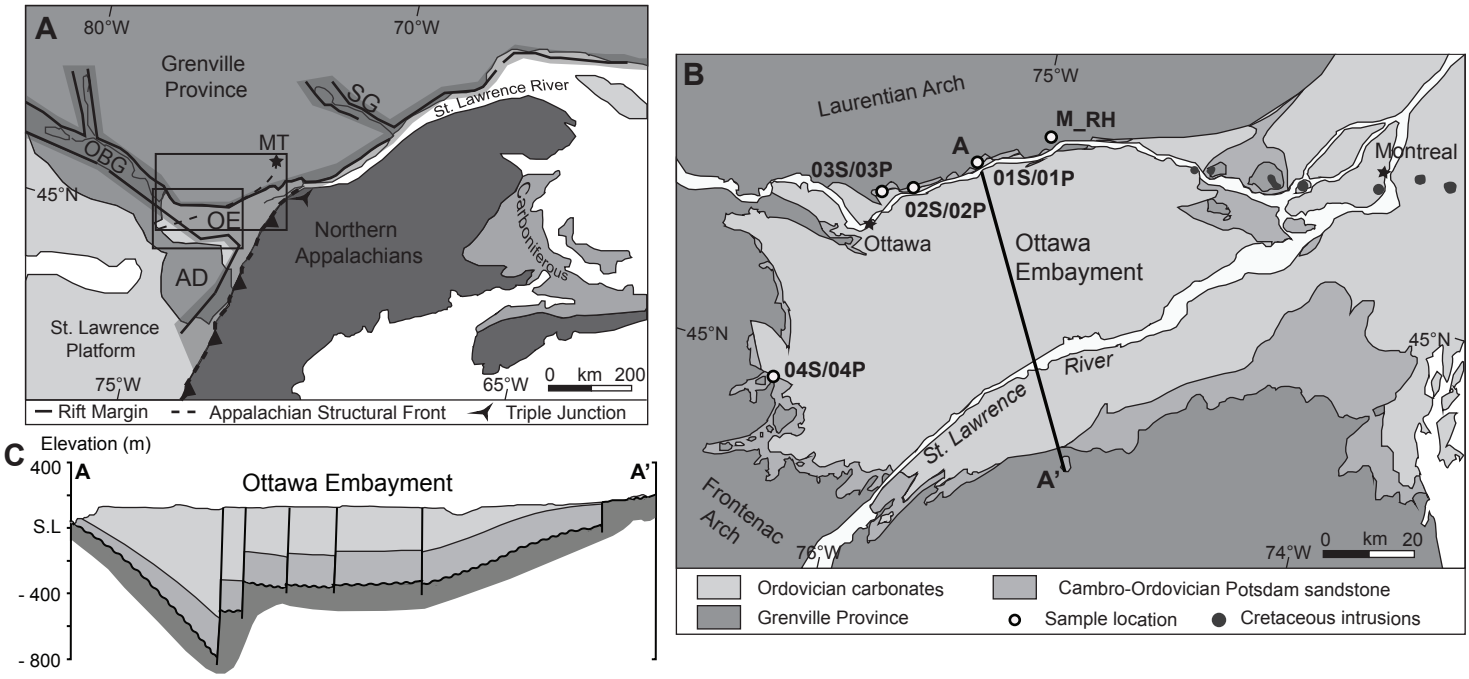

Figure 1. (A) The St. Lawrence rift system (shaded), a seismically active zone trending northeast-southwest, connecting the Ottawa-Bonnechere (OBG) and Saguenay grabens (SG). Structurally, the Ottawa-Bonnechere graben acts as the central axis of the Ottawa Embayment (OE) and rift related faults denote the contact between the Cambro-Ordovician sedimentary rocks of the embayment and the Grenville Province to the northwest. Samples were collected along a ~250 km NE-SW transect (dashed line), from Mont-Tremblant (MT) into the embayment and oblique to the axis of the rift system. Small inset box shows location of Fig. 1B and large inset box shows location of Fig 2. Modified from Kumarapeli and Saull 1966 and Sasseville et al. 2012. (B) Regional geology of the Ottawa Embayment showing the extent and distribution of the sedimentary successions and location of Cretaceous intrusive rocks related to the trace of the Meteor Hot Spot. Modified from Sanford and Arnott 2009b and Bleeker et al. 2011. (C) A NW-SE oriented stratigraphic and structural cross section A-A' across the Ottawa Embayment. Modified from Sanford and Arnott 2009b.

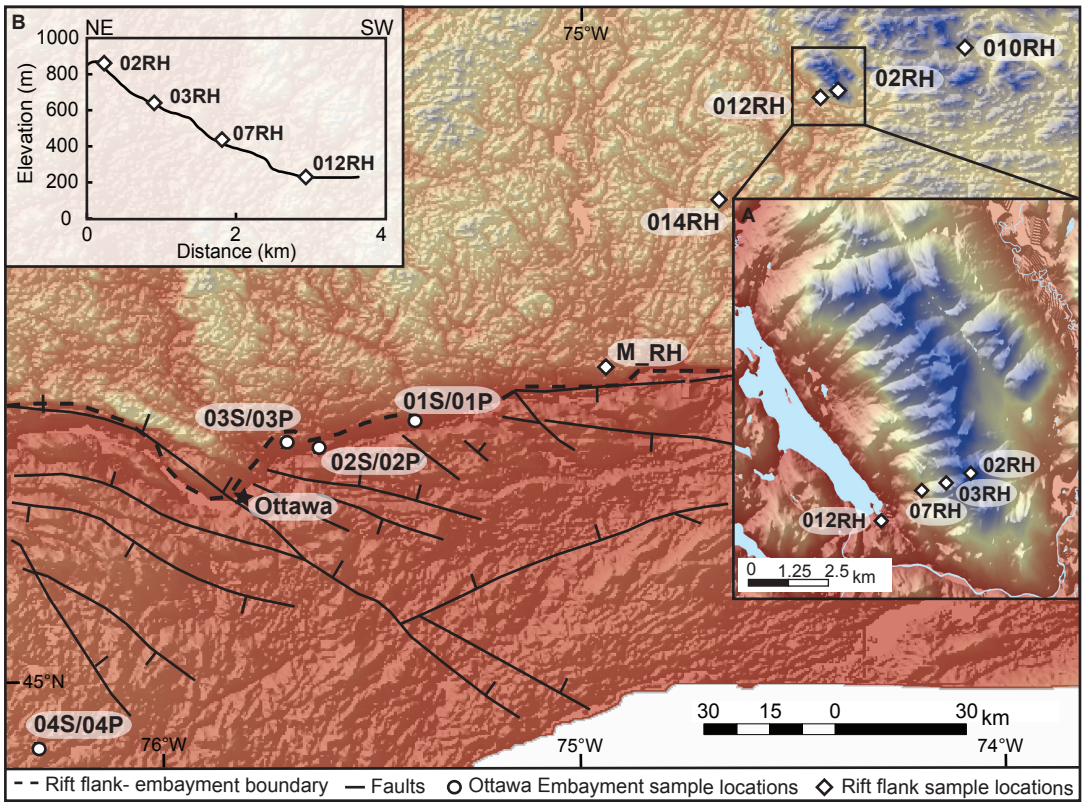

Figure 2. Digital elevation model (DEM) of study area with locations of 15 samples collected along ~250 km NE-SW transect from Mont-Tremblant, Québec (02RH, ~900 m) through the central axis of the Paleozoic rift to Perth, Ontario (04P, 04S), located in the St. Lawrence Lowlands (~65 m). Blue shades represent elevation highs of ~900 m and red shades represent lows of ~70 m. The main transect can be separated into two sections; the rift flank (diamond symbols) with a vertical transect along Mont-Tremblant (inset A a nd B), and the Ottawa Embayment (open circle symbols). Both samples of the basement and overlying sedimentary unit were collected at each location within the embayment.

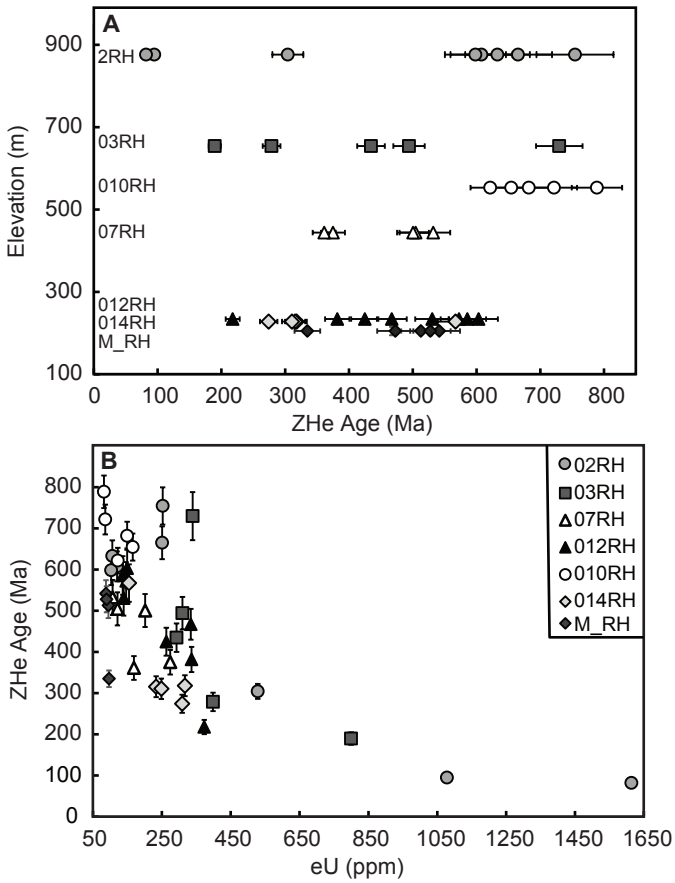

Figure 3. (A) Single zircon (U-Th)/He ages as a function of present day elevation and (B) single zircon (U-Th)/He ages plotted against their respective eU for samples collected from Mont-Tremblant and adjacent area along the rift flank.

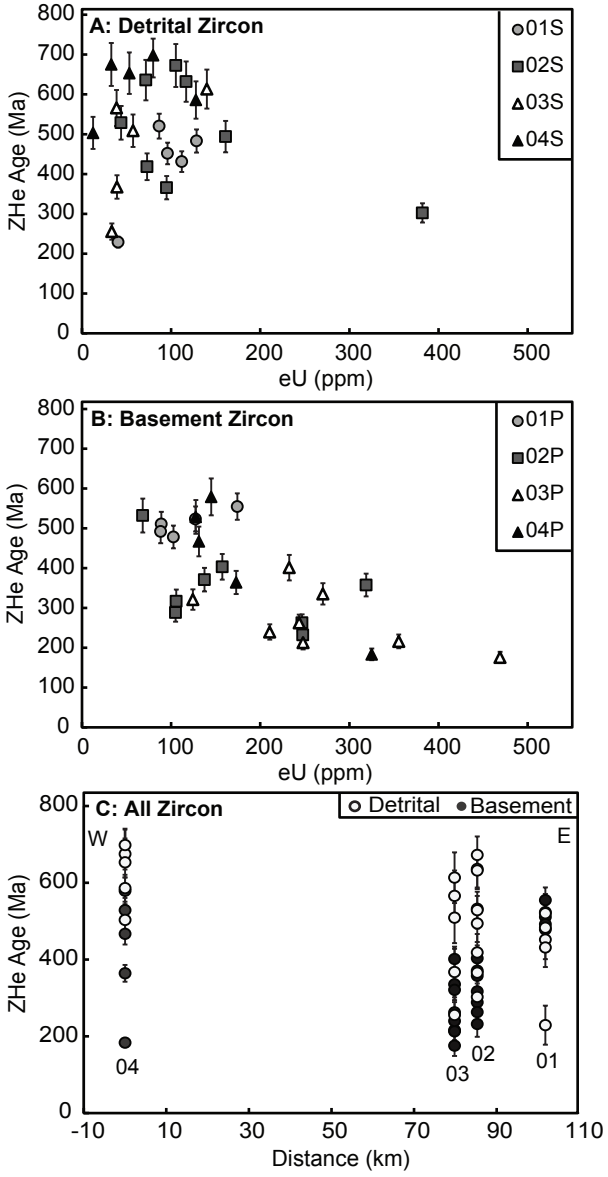

Figure 4. Single zircon (U-Th)/He ages as a function of eU for (A) detrital and (B) basement samples from the Ottawa Embayment. (C) Detrital and basement zircon (U-Th)/He ages plotted against their sample location along a west-to-east transect across the Ottawa Embayment. Detrital and basement samples of the same sample prefix (i.e. 01) come from the same outcrop location.

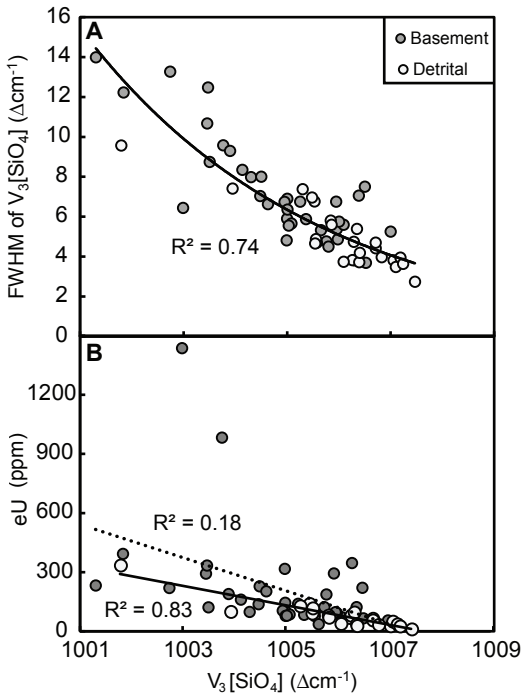

Figure 5. (A) Negative correlation between $v_3(SiO_4)$ frequency peaks and their respective spectra line breadths (FWHM), for the detrital and basement zircon of the embayment. (B) $v_3(SiO_4)$ plotted as a function of uranium concentration for individual detrital and basement zircon. The detrital grains possess a strong negative correlation as grains with higher uranium concentrations are generally more damaged than grains with lower uranium concentrations. Whereas, the basement zircons show a weak negative relationship, if at all, between uranium concentration and $v_3(SiO_4)$ peak frequency.

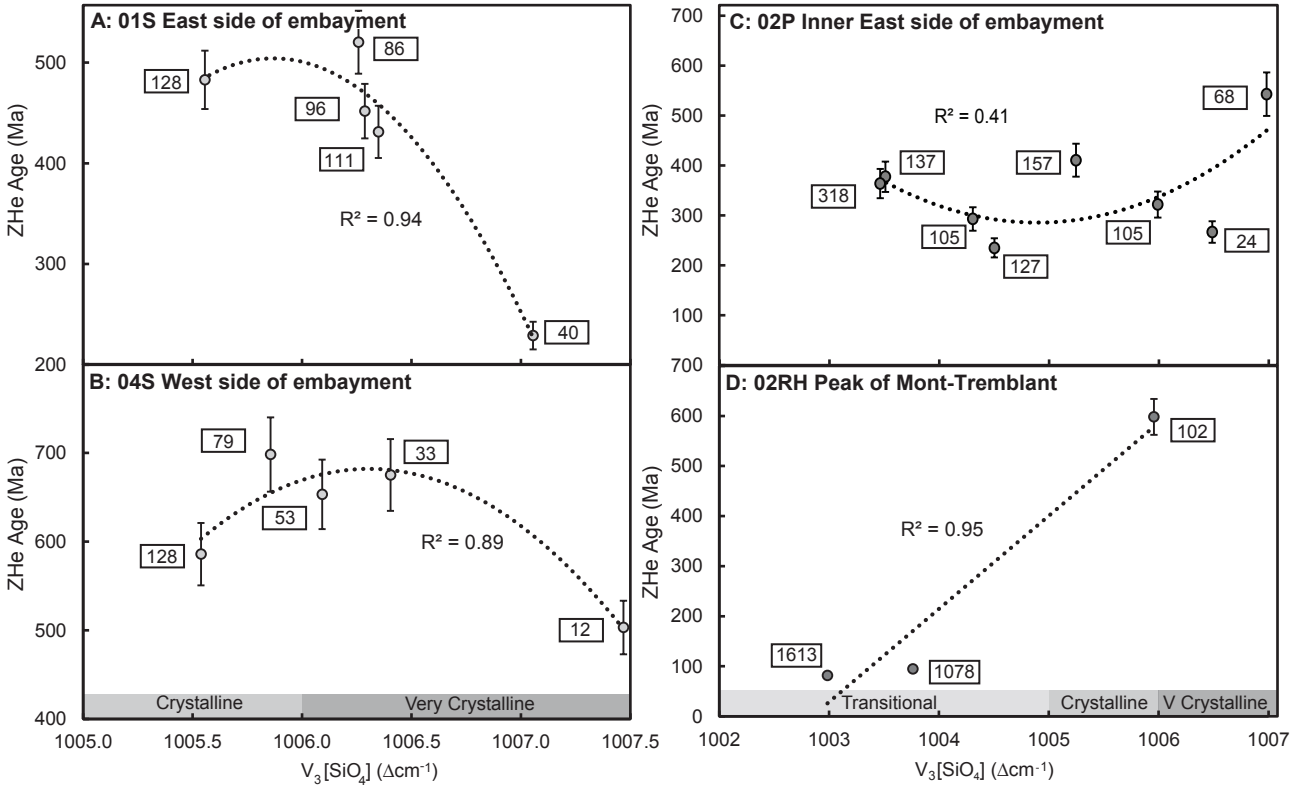

Figure 6: Individual zircon (U-Th)/He ages plotted against their respective Raman $v_3(SiO_4)$ peak frequency along with their reported eU values (boxes), for four representative samples. (A) 01S, a detrital sample from the easternmost side of the embayment, with individual grains spanning from very crystalline to crystalline, exhibiting both a negative and positive age-damage relationship, with increasing damage, also shown by eU. (B) 04S, a detrital sample from the westernmost side of the embayment, with very crystalline to crystalline grains, exhibiting both a positive and negative age-damage relationship, with increasing damage, also shown by eU (C) 04P, a basement sample from the westernmost side of the embayment, with well crystallized to transitional grains with a positive age-damage relationship, with increasing damage discordant with eU. (D) 02RH, a metamorphic basement sample from the peak of Mont-Tremblant along the rift flank, with crystalline to transitional grains, exhibiting a n egative age-damage relationship, analogous with eU values.

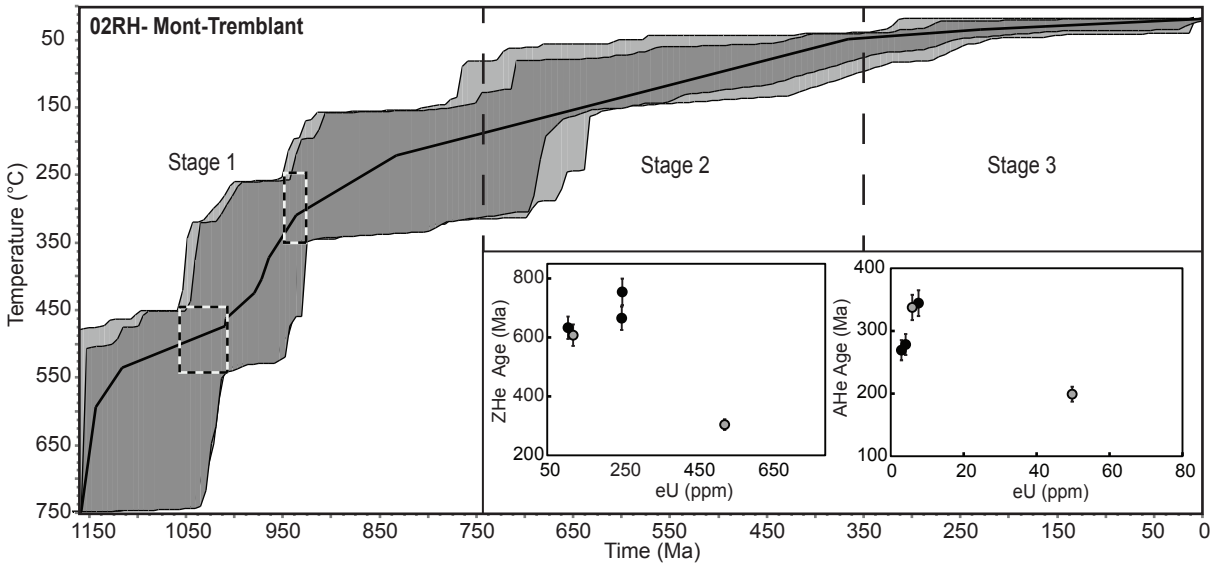

Figure 7. Inverse HeFTy thermal history model of sample 02RH, from the peak of Mont-Tremblant. This model is representative of the thermal history of the rift flank. The corresponding individual zircon and apatite (U-Th)/He age-eU plots for the sample are also shown, with the grains highlighted in black that were chosen for the inverse modeling. Two additional higher temperature constraints were added (dashed boxes) as defined by $^{40}Ar/^{39}Ar$ dating of biotite from Mont-Tremblant samples (Tc: ~250-350°C; data presented in this study) and hornblende (Tc: ~450-550°C) from within the surrounding region (Martignole and Reynolds, 1997). 'Good fit' solutions are represented by the dark grey envelope and 'Acceptable fit' solutions by the lighter grey. The solid black line displays the best-fit thermal path for the model.

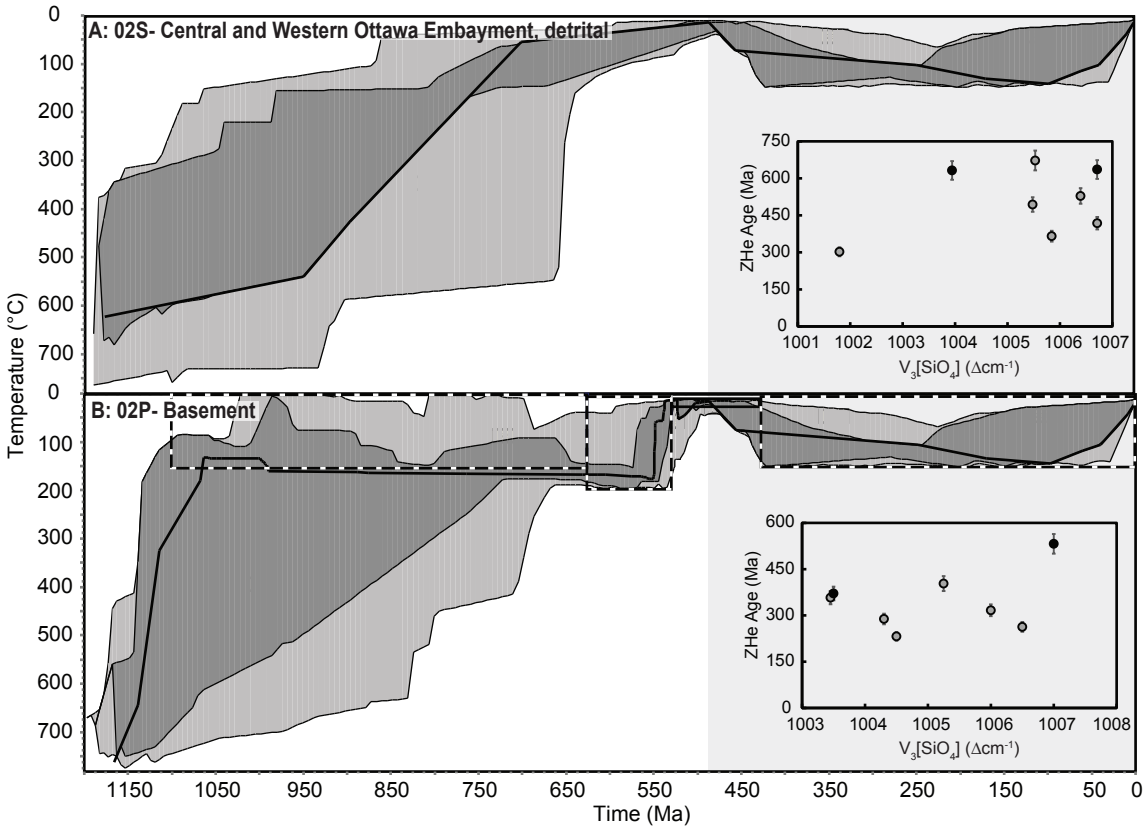

Figure 8. Inverse HeFTy thermal models for the (A) basement and (B) overlying detrital sample collected from the central-western side of the Ottawa Embayment transect. These models are representative of the thermal history experienced by the westernmost side and centre of the embayment (locations 04, 03, 02, from west to east). The inverse models were created using the multi-sampling method, allowing for the basement and detrital models to have unique pre-basin fill thermal histories, but identical post-basin fill histories (younger history that is shaded). The corresponding individual zircon (U-Th)/He age-Raman $v_3(SiO_4)$ peak graphs for each sample is to the bottom right of each model, with the ages used for modeling highlighted in black. Dashed boxes indicate additional time-temperature constraints and the solid line shows the best-fit thermal history for each model. 'Good fit' solutions are represented by the dark grey envelope and 'Acceptable fit' solutions by the lighter grey. The solid black line displays the best-fit thermal path for the model.

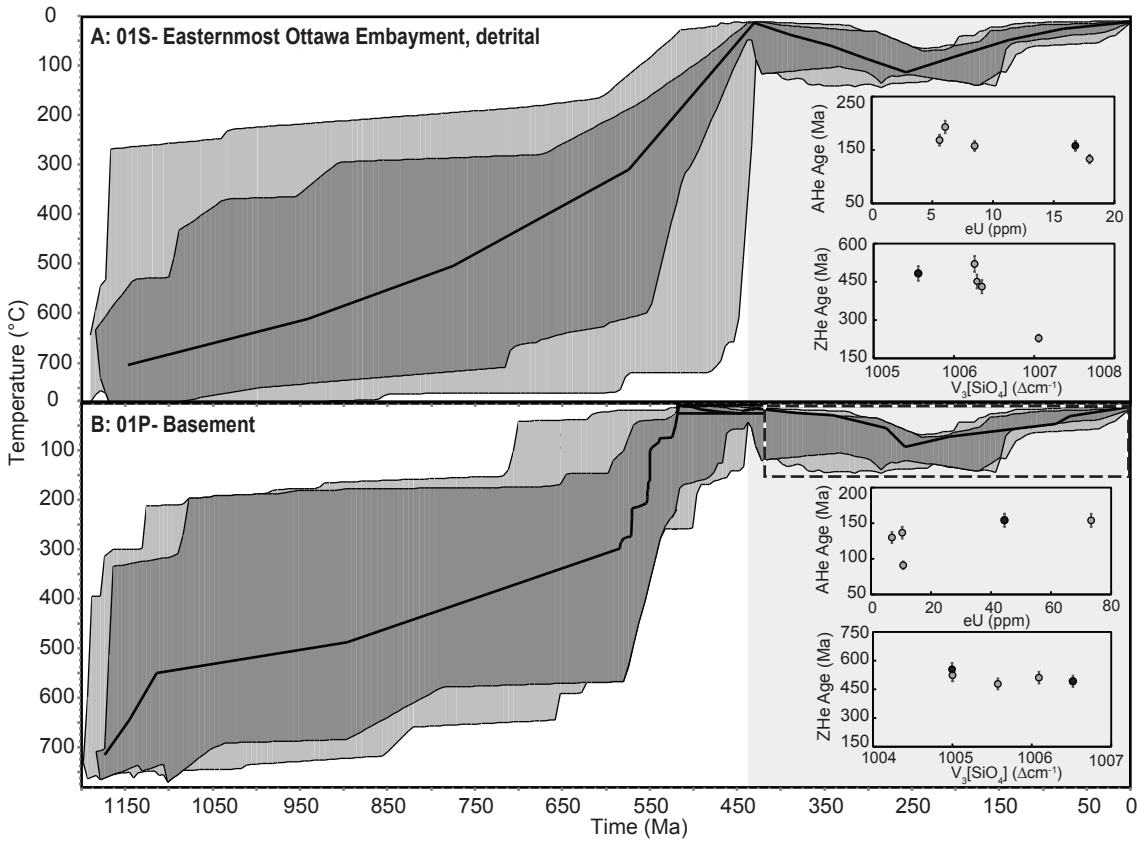

Figure 9. Inverse HeFTy thermal history models for the (A) Grenville basement and (B) overlying detrital sample collected from the easternmost side of the Ottawa Embayment. The inverse models were created using the multi-sampling method, allowing for the basement and detrital models to have unique pre-basin fill thermal histories, but identical post-basin fill histories (younger history that is shaded). The corresponding individual zircon and apatite (U-Th)/He age-Raman $v_3(SiO_4)$ peak graphs for the samples are also shown, with the ages used for modeling highlighted in black. Dashed boxes indicate additional time-temperature constraints and the solid line shows the best-fit thermal history for each model. 'Good fit' solutions are represented by the dark grey envelope and 'Acceptable fit' solutions by the lighter grey. The solid black line displays the best-fit thermal path for the model.

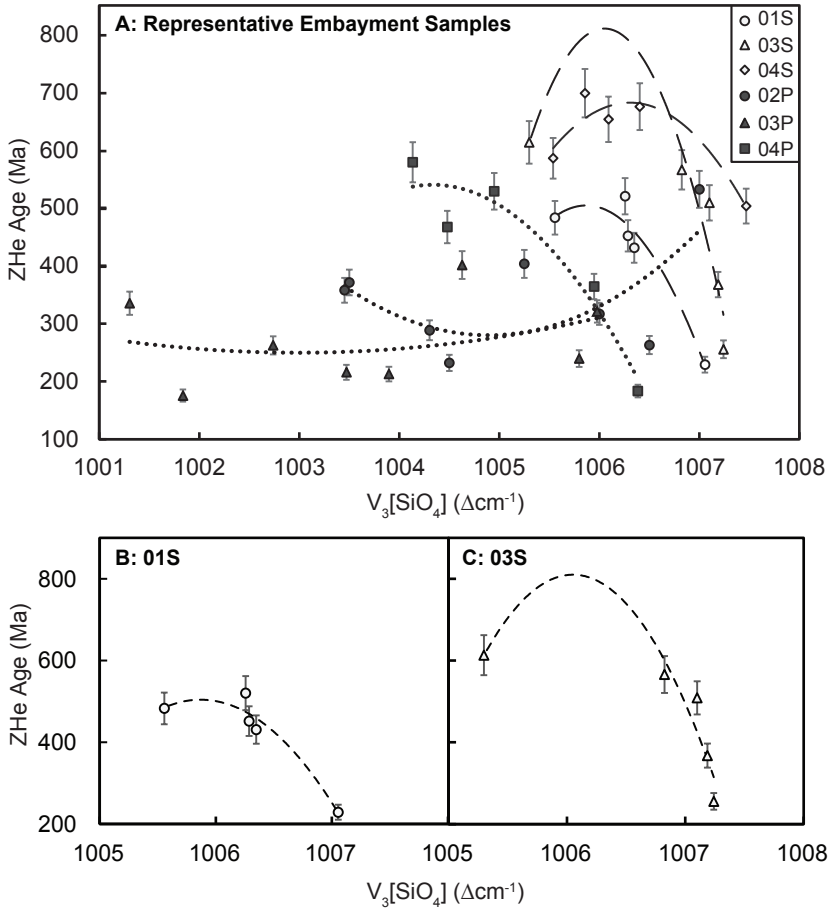

Figure 10: (A) Individual zircon (U-Th)/He ages plotted against their respective Raman $v_3(SiO_4)$ peak frequencies for three representative detrital (01S, 03S, 04S) and basement (02P, 03P, 04P) samples from the Ottawa Embayment. The non-reset detrital samples show common positive and negative age-damage trends, whereas the reset basement samples have variable and complex Raman signals. (B and C) Individual zircon (U-Th)/He ages plotted against their respective Raman $v_3(SiO_4)$ peak frequency for two representative samples.

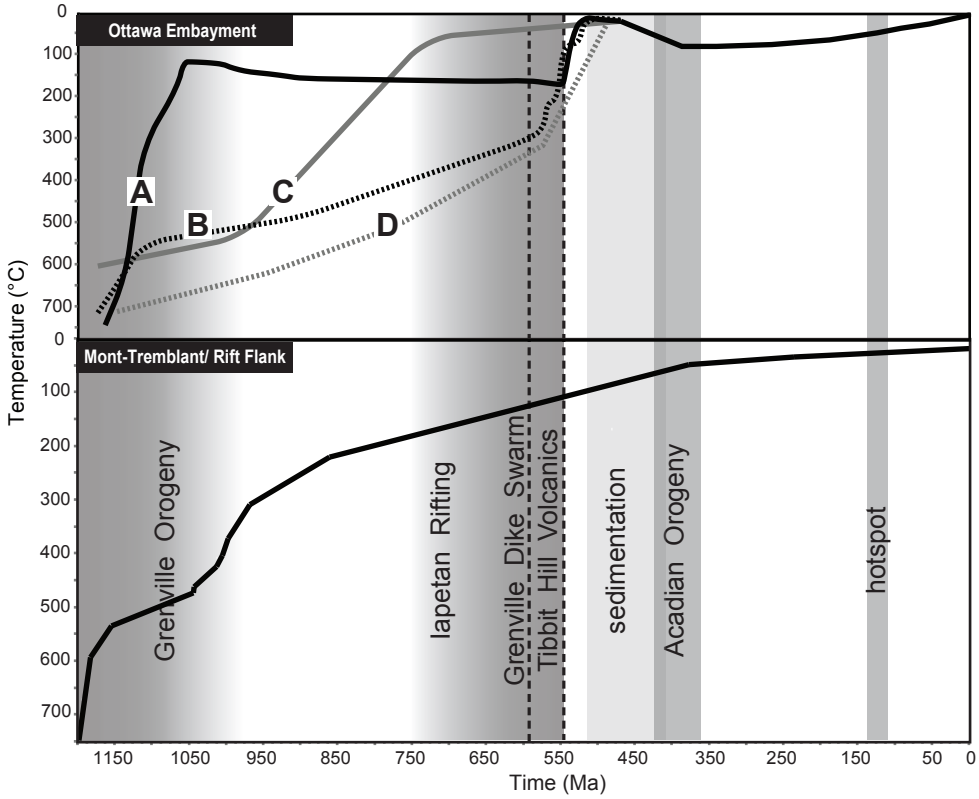

Figure 11: Timeline schematic of our interpretation of the T-t history of the rift flank (bottom) and Ottawa Embayment (top), determined with the use of modelled (U-Th)/He and $^{40}Ar/^{39}Ar$ thermochronometry data presented in this study, integrated with regional stratigraphic relationships, provenance studies and local geology. The Ottawa Embayment paths include: (A) the western and central basement, (B) the eastern basement, (C) the western and central Potsdam Group, and (D) the eastern Potsdam Group. Additional regional geological events are presented, including: the Grenville Orogeny, rifting with the break-up of Rodinia, intrusion of the mafic Grenville dike swarm (ca. 590 Ma), T ibbit Hill volcanics (ca. 550 Ma), Acadian orogenesis and passing of the hotspot.

APPENDIX TO:

(U-Th)/He thermochronology of the Ottawa Embayment, Eastern Canada: the temperature-time history of an ancient, intracratonic rift basin

R.A. Hardie

Department of Earth and Environmental Sciences, University of Ottawa, Canada

TABLE OF CONTENTS

A1. Introduction

This supplementary document includes additional details on sample descriptions and analytical techniques for x-ray micro-computed tomography, Raman spectroscopy, and apatite and zircon (U-Th)/He dating. It also includes the $^{40}Ar/^{39}Ar$ geochronology methodology and our results. Supplementary **Figures DR1-DR7** and **Tables DR1-DR5** are available in separate files.

A2. Sample Descriptions

The zircon grains chosen for analysis from basement samples were generally euhedral and prismatic to elongate whereas the detrital zircons chosen from the overlying cover were subhedral to euhedral. The grains varied in size as expressed in the spherical grain geometry. See **Table DR1 and DR2**.

A2.1. Rift Flank Samples

The Mont-Tremblant massif is a large elliptical mass of quartzofeldspathic granulite which is younger than and intrusive to the Grenville Series (Katz, 1969). The four samples (002RH, 003RH, 007RH, 012RH), collected at elevations ranging from 876-234 m (18T0534520, 5118677 to 18T0531679, 5117146), of quartzofeldspathic gneiss from the crystalline rift flank elevation transect have very similar mineral assemblages that comprise of quartz + plagioclase + mesoperthite + orthopyroxene + minor biotite ± clinopyroxene ± hornblende. Zircon and apatite can be seen in thin section and are ubiquitous throughout the samples. Minor amounts of oxides, likely ilmenite and/or magnetite are evident. The samples are medium to coarse grained with weak to moderate gneissic foliation and may have a bated augen/flasser like texture. No signs of strain remain in thin section. Their dominantly recrystallized fabrics consists of quartz, plagioclase and mesoperthite plates with bands of darker elongate minerals like biotite and pyroxene. The distal

sample (010RH, 553m; 18T0554095, 5130882) to the northeast of the Mont-Tremblant massif is a coarse grained quartz monzonite and sample (014RH, 228m; 18T0516396, 5092503) to the southwest is a rose granite. The sample extracted from between the Mont-Tremblant and Ottawa Embayment transects (M_RH, 205 m; 18T0497684, 5055405) is an amphibolite from Papineauville, Québec. It is medium grained, weakly foliated, dark grey/green/ black in colour and is comprised of feldspar + amphibole + biotite + minor quartz.

Additional samples for $^{40}Ar/^{39}Ar$ dating include, 04RH, 06RH and 013RH. 04RH (598 m; 18T0533474, 5118249) is a medium grained, gray to black diabase comprised of plagioclase feldspar, and pyroxene or hornblende. 06RH (500 m; 18T0533474, 5118136) is a course grained medium grey and pink meta-granite. It is weakly foliated and largely composed of quartz and feldspar with secondary biotite. Sample 013RH, (203 m; 18T0525751, 5102212) was collected ~10 km SW of Mont-Tremblant, in Brébeuf, Quebec and was an augen-gneiss. It was coarse grained and composed of feldspar, quartz and secondary garnet and characterized by large elliptic feldspar porphyroblasts.

A2.2. Ottawa Embayment Samples

The four samples (01P, 02P, 03P, 04P) from the Precambrian Grenville basement beneath the Ottawa Embayment are high grade metagranite to gneiss. They are composed of quartz + feldspar + minor biotite ± minor garnet ± minor muscovite. The basement samples range from medium to coarse grained and are largely equigranular. The metagranites are predominantly massive with locally developed weak gneissic foliation. Zircon is prevalent throughout the samples while quality apatite is scarce. The four samples (01S, 02S, 03S, 04S) from the overlying sedimentary Nepean Formation within the Ottawa Embayment consist of quartz arenite. The arenite is cemented by a silica matrix, ranges in colour from a bright white to a medium beige and

is well sorted with rounded grains. The sedimentary samples are locally iron stained and thinly layered. Burrows were present in outcrop scale, however no fossils were present in the extracted samples.

Samples 01P and 01S were collected in Masson-Angers, Québec *(*18T0466714, 5043139) at an elevation of 75 m. The basement sample, 01P, is a massive and coarse muscovite-biotite metagranite. It is light to medium grey with some hints of pink and weathered to a dark grey-beige. The samples mineral composition consists of quartz (75%) + feldspar (15%) + minor muscovite (5%) + minor biotite (5%). 01S, the sample from the overlying Nepean Formation, is a quartz arenite. It is a light bluish grey in colour and weathers to a medium beige. It is medium to coarse grained and is cemented together by a silica matrix (<15%). The sample is well sorted, has rounded grains and is locally iron stained. The arenite has some layering visible that is further defined by detrital biotite. Zircon is a prevalent and apatite is present in both samples.

Samples 02P and 02S were collected at Lac Beauchamp Park in Gatineau, Québec (18T0451413, 5036866) at an elevation of 68 m. The basement sample, 02P, is a biotite granitic gneiss. It is pinkish grey to light grey in colour and weathers to a medium beige. The unit the sample was extracted from is largely foliated and locally massive. The sample is medium grained, equigranular and is comprised of quartz (70%) + feldspar (20%) + biotite (10%). The sample is highly weathered. 02S, the sample from the overlying sedimentary unit, is a quartz arenite. It is bright white in colour and weathers to a light grey. It is medium grained, well sorted, has rounded grains and some visible layering. It is cemented together by a silica matrix (~20%). Zircon is present and apatite is absent in both samples.

Samples 03P and 03S were also collected in Gatineau, Québec (18T0446258, 5038386), nearby the Hôpital de Gatineau at an elevation of 65 m. The basement sample, 03P, is a biotite

metagranite. It is medium grained, equigranular, massive and blue grey in colour, weathered dark grey. It is comprised of quartz (65%) + feldspar (20%) + biotite (15%). 03S, from the sedimentary unit lying above, is a quartz arenite. It is a bright white colour and weathers to a light grey. It is medium grained, well sorted and has rounded grains. It is cemented together by a silica matrix (~15%). Zircon is present while apatite is absent in both samples.

Samples 04BP and 04S were collected in Perth, Ontario (18T0405509, 4969027) at an elevation of 130 m. The basement sample, 04P, is a garnet-biotite metagranite to gneiss. It is bluish-pink-grey to dark grey in colour, weathers medium beige, is coarse grained and largely equigranular. The sample is massive and also has locally developed gneissic foliation. It is made up of quartz (65%) + feldspar (20%) + biotite (10%) + garnet (5%). Sample 04S, from the overlying sedimentary unit, is a quartz arenite. It is a light beige colour and weathers to medium grey. It is medium to coarse grained, well sorted, has rounded grains and is cemented together by a silica matrix (~15%). Zircon is a prevalent accessory mineral whereas apatite is absent from both samples.

A3. Methodology of the apatite and zircon (U-Th)/He analyses

(U-Th)/He thermochronology was conducted at the Thermochronology Research and Instrumentation Laboratory (U-Th)/He facility at the University of Colorado at Boulder, USA. Individual mineral grains were handpicked using a Leica M165 binocular microscope equipped with a calibrated digital camera and capable of both reflected and transmitted, polarized light. The grains were screened for quality, including crystal size, shape, and the presence of inclusions. After characterization, grains were placed into small Nb tubes that were then crimped on both ends. This Nb packet is then loaded into an ASI Alphachron He extraction and measurement line. The packet

is placed in the UHV extraction line (~$3x10^{-8}$ torr) and heated with a diode laser to ~800-1100°C for 5 to 10 m to extract the radiogenic ^{4}He. The degassed ^{4}He is then spiked with approximately 13 ncc of pure ^{3}He, cleaned via interaction with two SAES getters, and analyzed on a Balzers PrismaPlus QME 220 quadrupole mass spectrometer. Degassed grains are then removed from the line, and taken to a Class 10 clean lab for dissolution. Apatite grains, still enclosed in the Nb tubes, are placed in 1.5 mL Cetac vials, spiked with a ^{235}U-^{230}Th tracer in HNO_3, capped, and baked in a lab oven at 80°C for 2 h. Zircon are dissolved using Parr large-capacity dissolution vessels in a multi-step acid-vapor dissolution process. Grains (including the Nb tube) are placed in Ludwig-style Savillex vials, spiked with a ^{235}U-^{230}Th tracer, and mixed with 200 µl of Optima grade HF. The vials are then capped, stacked in a 125 mL Teflon liner, placed in a Parr dissolution vessel, and baked at 220°C for 72 h. After cooling, the vials are uncapped and dried down on a 90°C hot plate until dry. The vials then undergo a second round of acid-vapor dissolution, this time with 200 µl of Optima grade HCl in each vial that is baked at 200°C for 24 h. Vials are then dried down a second time on a hot plate. Once dry, 200 µl of a 7:1 HNO_3:HF mixture is added to each vial, the vial is capped, and cooked on the hot plate at 90°C for 4 h. Once the minerals are dissolved, regardless of the dissolution process, they are diluted with 1 to 3 mL of doubly-deionized water, and taken to the ICP-MS lab for analysis. Mineral standards of Durango Apatite (31.5 Ma) and Fish Canyon Tuff Zircon (28.2 Ma) are routinely analyzed (degassed and dissolved) in conjunction with the samples with each run to ensure data integrity. Sample solutions, along with standards and blanks, are analyzed for U, Th, and Sm content using a Thermo Element 2 magnetic sector mass spectrometer. Once the U, Th, and Sm contents have been measured, He dates and all associated data are calculated in a custom spreadsheet made by CU TRaIL staff.

A4. X-ray micro computed tomography: Methodology and XR-μCT results vs microscope-based measurement results

(U-Th)/He thermochronology employs individual grain analysis and each zircon age is reported as an alpha-ejection corrected age with uncertainties of ~8% (2σ; e.g., Reiners et al. 2004). Accuracy of the age is limited by broken, rounded or eroded grains, U-Th rich inclusions, the accuracy of microscope-based dimensional measurements and analytical error (Farley 1996; Rahl et al. 2003; Reiners 2005; Evans 2008). The alpha-ejection correction (F_T) is used to account for the effects of alpha-ejection, a complication with the use of (U-Th)/He dating. Alpha particles produced by nuclear decay of U and Th are emitted with a kinetic energy that allows them to travel a specific stopping distance through the crystal lattice before coming to rest and are either retained or ejected from the individual crystal. For zircon, the specific stopping distances are 15.55 μm for ^{238}U, 18.05 μm for ^{235}U and 18.43 μm for ^{232}Th (Ketcham et al. 2011), and the F_T accounts for the consequential He loss from parent nuclides located within the outer 20 μm of the grain.

Typically, the F_T is determined quantitatively using ideal crystal dimensions and assuming homogenous distribution of the parent nuclides (Farley 2002; Ketcham et al. 2011). This method may result in inaccurate or poorly estimated F_T values and therefore age corrections for grains with non-ideal geometries due to the impact of physical weathering, such as detrital grains from sedimentary basins or alluvial environments. Therefore, determining accurate F_T values for non-ideal crystal geometries require more direct methods of measurement. Recent work has shown the usefulness of 3D imaging when applied to single crystal dating to improve age determination (Ketcham, 2005; Herman et al. 2007; and Evans et al. 2008). 3D imaging can be conducted with the use of X-ray micro-computed tomography (XR-μCT), a high-resolution version of the commonly used medical computerized axial tomography (CAT) scan. XR-μCT is a non-

destructive technique that can be used to identify unsuitable grains and obtain accurate grain volume measurements.

Ultra-high resolution X-ray micro-computed tomography (XR-μCT) was completed at the XR-μCT Laboratory for Earth Material Research at Carleton University, Ottawa, Canada. After the zircon grains were selected, they were mounted in rows on a ¼ inch circular piece of double-sided sticky tape. Measurements were made with a SkyScan1173 (Hardware version A, Software Version 1.6) scanner with a distortion-free 2240 x 2240 pixel-flat-panel-x-ray-sensor, a camera with a pixel size of 50 μm, and a source voltage of 70 kV. 1371 cross-section image slices were acquired as tagged image files with pixel sizes and inter-pixel spacing of 5.33 μm using a 1.0 mm aluminum filter and a 1300 ms exposure. The scanning trajectory was round with a step and shoot motion and images were obtained at rotational steps of 0.175°. The scan required three hours of imaging. Once imaging was complete, the program Blob3D (Version 1.4, Beta 1) written by Ketcham et al. (2005) was implemented to process and reconstruct the XR-μCT data, render 3D images and extract individual zircon grain information. Three main steps were executed using the software, including; segmentation, separation and extraction. Segmentation was completed through defining a range of voxel grayscales called a threshold, to be used for grain voxel selection and to convert the grayscale images into binary black and white images. The images are converted to 256 shades ranging from pure black at zero, to pure white at 255. A grayscale threshold range of 70-255 was manually implemented. The contiguous sets of blobs, groups of classified voxels within the set threshold range, were then individually inspected and processed to determine if they were objects of interest (zircon grains) and discern if the blob encompassed multiple objects. Blobs made up of multiple, touching or close grains, or unwanted objects were then manually separated to be accurately measured. Once separated, the zircon grains volumes, shape, contact relationships,

centers of mass, surface areas, long axis orientation and Ft data could be measured and extracted. With Blob3D, F_T correction values for ^{238}U, ^{235}U and ^{232}Th were measured for each of the individual zircon grains using the Ketcham et al. method (2011). As ^{235}U and ^{232}Th have similar decay energies, the He from these two parents are associated with one F_T value. To obtain a single F_T value the weighted mean for U and Th values was computed for each grain using,

$$^{Mean}F_T = a_{238}\ ^{238U}F_T + (1 - a_{238})\ ^{232Th}F_T \qquad \text{(Farley, 2002)}$$

where a_{238} is approximated from the measured Th/U ratio as:

$$a_{238} = (1.04 + 0.245\ (Th/U))^{-1} \qquad \text{(Farley, 2002)}$$

The Ft correction is then applied to determine the corrected age using,

$$\text{Corrected age} = \text{measured age} / F_t \qquad \text{(Farley, 1996)}$$

Therefore, the closer the Ft value is to 1, the smaller the alpha-ejection correction applied to the measured age.

The CT method utilizes an individual grain's measured surface area and volume to determine its F_T correction value. Both the CT and purely dimensional method were used to determine an F_T for each grain, to assess and compare the precision of each technique. The 84 suitable grains that were imaged and measured (of the 150 total) using XR-µCT yielded a range of calculated F_T values from 0.723 to 0.857, with an average of 0.80. The F_T calculated from the microscope-based grain dimensions on the same grains yielded an F_T range of 0.725 to 0.865, with an average of 0.80 (**Table 1** and **Table DR3**). In general, the variation between XR-µCT and the microscope-based dimensional grain F_T values was ±1.32% with a maximum difference of 8.24% for a visibly pitted zircon and a minimum difference of ±0.05% for a euhedral grain. The average difference between the XR-µCT F_T values and dimensional F_T results was ±1.45% for the basement zircons and ±1.10% for the detrital zircon grain population. As (U-Th)/He ages are

reported with uncertainties of ~8% (2σ) or less (e.g., Reiners et al. 2004), the final XR-μCT F_T corrected (U-Th)/He ages would commonly lie within the range of uncertainty of the dimensional F_T corrected (U-Th)/He ages. Although the F_T values for both methods were quite similar, the XR-μCT method was still beneficial, as the 3D grain images revealed inclusions and grain shape irregularities, largely aiding in the grain selection process and prevention of anomalous (U-Th)/He age determinations. Future (U-Th)/He thermochronology studies with only non-ideal or significantly rounded grains for analysis should consider using XR-μCT as a more precise method of F_T determination.

A5. Methodology of the Raman spectroscopy

High resolution Raman spectroscopy measurements were made with a Bruker Senterra μ-Raman spectrometer at Union College, Schenectady, USA. The Raman spectroscopy was conducted using a 633 nm external He-Ne laser with a 2 μm beam diameter and 20 mV of power. The aperture was 1000 nm, the spectral resolution was 3-5 cm^{-1} and the laser focusing objective was 50x or 20x. Spectra within the 1800b, 417-1805 cm^{-1} spectral range were recorded and integration times were dominantly 30 seconds, with up to 5 co-additions. OPUS 7.0 spectroscopy software was used as an interface for measurement collection. After the baseline correction was applied, the software FitYK, was implemented for Gaussian-Lorenzian peak fitting of the v_1SiO_4 (~974 cm^{-1}) symmetric stretching band and the v_3SiO_4 (~1007 cm^{-1}) antisymmetric stretching band, as well as for determination of the dispersion of frequency of the full width half maximum (FWHM). Each zircon grain was unpolished and placed within a divot in a glass slide for analysis. 83 individual grains were oriented with their c-axis parallel to the microscopes N-S oriented crosshairs and measured in two or more spot locations.

A6. Biotite $^{40}Ar/^{39}Ar$ geochronology: methodology and results

The $^{40}Ar/^{39}Ar$ technique is based upon the conversion of a known fraction of ^{39}K into ^{39}Ar as a result of neutron bombardment, and the age is then calculated from the measured $^{40}Ar/^{39}Ar$ ratio in K bearing materials. A stepwise heating technique is commonly used, where Ar isotopes are released in incremental heating stages resulting in a spectrum of apparent ages for a single sample (Dalrymple and Lanphere 1971). Minerals used for $^{40}Ar/^{39}Ar$ dating have higher T_c (300-550°C) relative to the zircon and apatite (U-Th)/He system (<200°C) and specifically biotite has a normal T_c of 300°C (Dallmeyer 1978; Harrison et al. 1979; Harrison et al. 1985). Biotite was extracted from four samples from within the Grenville rift flank; including one sample from the main transect (010RH) located 20 km northeast of Mont-Tremblant, two additional samples from mid-elevations (~500-600 masl) along Mont-Tremblant (04RH, 06RH), and one additional sample from ~10 km southwest of the mountain near Brébeuf, Québec (013RH). Biotite was obtained through traditional crushing and manual separation techniques, and loaded into Al foil packets which were then stacked in foil tubes and placed into the holes of an aluminum cylinder.

After mechanical mineral separation from the host rock to achieve 99% purity, mica with grain size between 106 and 250 μm was picked and washed with dilute HCl. Individual mineral separates were loaded into 2-3 mm-deep aluminum foil packets, which were subsequently stacked vertically into 35-mm long foil tubes and placed into the tubular holes of an aluminum cylinder. Several flux monitor grains of Fish Canyon tuff sanidine (FCT-SAN) (28.02 ± 0.16 1σ Ma; Renne et al., 1998, ^{40}K decay = $5.543e^{-10}$/a, Steiger and Jäger, 1977) were loaded into each sample packet. The vessel was irradiated for 160 MWH in medium flux position 8A at the research nuclear reactor of McMaster University (MNR) in Hamilton, Canada. Neutron fluence was approximately 1.08 x

10^{13} neutrons/cm^2 operating at a 2.5 MW power level. Correction factors for typical interference species produced by thermal neutrons during irradiation are 0.058 ($^{40}Ar/^{39}Ar_K$), 0.000743 ($^{39}Ar/^{37}Ar_{Ca}$) and 0.000258 ($^{36}Ar/^{37}Ar_{Ca}$).

Analytical conditions follow the protocol of Kellett and Joyce (2014). Small aliquots (1-2 grains) and monitors were loaded into separate 1.5 mm diameter pits in a copper planchet and placed under vacuum. Individual grains were progressively heated and analyzed using a Photon Machines Ltd. Fusion 10.6 55W CO_2 laser coupled to the all-metal extraction line and a Nu Instruments Noblesse multicollector mass spectrometer operated at the Geological Survey of Canada, Ottawa, Canada. Laser heating was homogenized over a beam radius of 2 mm for a total of 40 sec, after which the released gas was exposed to SAES^{TM} NP-10 (~400°C) and HY-STOR® 201 (25°C) getters in the extraction line for three minutes. Following gettering, sample gas was expanded into the mass spectrometer. The Nu Noblesse is a single-focussing, Nier-source, magnetic sector multicollector noble gas spectrometer equipped with two quadrupole lens arrays. Argon ions were measured with a fixed array of three ETP® discrete dynode ion-counting multipliers (IC0, IC1, IC2). Data collection occurred in two multicollection cycles: cycle 1 = $^{40}Ar_{IC0}$, $^{38}Ar_{IC1}$ and cycle 2 = $^{39}Ar_{IC0}$, $^{37}Ar_{IC1}$, $^{36}Ar_{IC2}$. Blanks were run every 5 analyses, in an identical manner to unknowns. Air shots were analyzed every 10 analyses to monitor efficiency and mass fractionation. Relative collector efficiency and mass bias corrections were made for IC1 and IC2 collectors relative to IC0 using $^{40}Ar_{IC0}/^{36}Ar_{IC1}$ and $^{40}Ar_{IC0}/^{36}Ar_{IC2}$ measurements of air. Mass bias in IC0 was not corrected as it would be equally applied to the $^{40}Ar/^{39}Ar$ ratio in unknowns and J-factors determined from monitors in the age calculation, thereby cancelling out (e.g. Brumm et al., 2010). Error in J-factor values are conservatively estimated at ±0.6% (2σ). Sensitivity of the Nu Noblesse at the time of analyses was 7.1-7.5 Amps/mol. Data collection,

reduction, error propagation, age calculation and plotting were performed using the software MassSpec (version 7.93; Deino, 2001).

Analytical results are presented in **Table DR5**; **Figure DR7** presents the data as spectra where the width of each bar (thermal increment) represents the proportion of evolved gas, and the height represents the uncertainty associated with the apparent age. The integrated (or total gas: Tg) age is an average age for the sample calculated by summing the isotopic measurements of all steps with an uncertainty calculated by quadratically combining errors of isotopic measurements of all steps. Plateau ages are conventionally defined as the portion of an age spectrum composed of contiguous increments representing >70% of gas released which result in concordant ages (Mahon, 1996). A preferred age (Tp), on the other hand, is calculated as the weighted mean of a selection of mostly contiguous increments which represent >50% of ^{39}Ar gas released and result in concordant ages. The calculated age uncertainties are relatively small because analytical precision in the age of each heating step is high.

^{40}Ar/^{39}Ar analysis of one aliquot (1-2 grains) for each of the two Mont-Tremblant mountain samples 04RH and 06RH, yielded ages of 928 ± 4 Ma and 934 ± 4 Ma, respectively. For samples 010RH, from NE of Mont-Tremblant, and 013RH, from SW of Mont-Tremblant, two aliquots were analysed. 010RH yielded ages of 977 ± 4 Ma and 973 ± 4 Ma and 013RH yielded ages of 940 ± 4 Ma and 929 ± 4 Ma. Analytical results are presented in **Table DR5** and **Figure DR7.**

References

Brumm, A.; Jensen, G. M.; van den Bergh, G. D.; Morwood, M. J.; Kurniawan, I.; Aziz, F.; and Storey, M. 2010. Hominins on Flores, Indonesia, by one million years ago. *Nature.* 464: 748-752.

Dallmeyer, R. D. 1978. ^{40}Ar/ ^{39}Ar incremental-release ages of hornblende and biotite from Grenville basement rocks within the Indian Head Range complex, southwest Newfoundland:

their bearing on Late Proterozoic Early Paleozoic thermal history. *Can. J. Earth. Sci*. 15:1374-1379.

Dalrymple, B. G.; and Lanphere, M. A. 1971. $^{40}Ar/^{39}Ar$ Technique of K-Ar Dating: A Comparison with the Conventional Technique. *Earth Planet. Sci. Lett*. 12:300-308.

Deino, A.L. 2001. Users manual for Mass Spec v. 5.02. Berkeley Geochronology Center Special Publication 1a, 119 p.

Evans, N. J.; McInnes, I. A.; Squelch, A. P.; Austin, P. J.; McDonald, B. J.; and Wu, Q. 2008. Application of X-ray micro-computed tomography in (U-Th)/He thermochronology. *Chem. Geol*. 257:101-113.

Farley, K. A.; Wolf, R. A.; and Silver, L. T. 1996. The effects of long alpha-stopping distances on (U-Th)/He dates. *Geochim. Cosmochim. Acta.* 60:4223-4230.

Farley, K. 2002. (U-Th)/He dating: techniques, calibrations, and applications. *Rev. Mineral. Geochem*. 47:819-844.

Harrison, T. M.; Armstrong, R. L.; Naeser, C. W.; and Harakal, J.E. 1979. Geochronology and the thermal history of the Coast Plutonic Complex, near Prince Rupert, British Columbia. *Can. J. Earth. Sci.* 16:400-410.

Harrison, T. M.; Duncan, I.; and McDougall, I. 1985. Diffusion of ^{40}Ar in biotite: Temperature, Pressure and compositional effects. *Geochom Cosmochim Acta*. 49:2461-2468.

Herman, F.; Braun, J.; Senden, T. J.; and Dunlap, W. J. 2007. (U-Th)/He thermochronometry: mapping 3D geometry using micro-X-ray tomography and solving the associated production-diffusion equation. *Chem, Geol*. 242:126-136.

Katz, M. B., 1969. The nature and origin of the granulites of Mont Tremblant Park, Quebec: *Geol. Soc. Am. Bull.* 80:2019-2037.

Kellett, D.; Joyce, N. 2014. Single- and multi-collection $^{40}Ar/^{39}Ar$ measurements for conventional step-heating and total fusion age calculation using the Nu Noblesse at the Geological Survey of Canada. Geological Survey of Canada Technical Note 8, 27 p.

Ketcham, R. A. 2005. Computational methods for quantitative analysis of three-dimensional features in geological specimens. *Geosphere*. 1: 32-41.

Ketcham, R. A.; Gautheron, C.; and Tassan-Got, L. 2011. Accounting for long alpha-particle stopping distances in (U-Th-Sm)/He geochronology: Refinement of the baseline case. *Geochim. Cosmochim. Acta*. 75:7779-7791.

Mahon, K. 1996. The new "York" regression; application of an improved statistical method to geochemistry. *Int. Geol. Rev.* 38:293–303

Rahl, J. M.; Reiners, P. W.; Campbell, I. H.; Ncolescu, S.; Allen, C. M. 2003. Combined cingle grain (U-Th)/He and U/Pb dating of detrital zircons from the Navajo Sandstone, Utah. *Geology.* 31:761-764.

Reiners, P. W.; Spell, T. L.; Nicolescu, S.; and Zanetti, K. A. 2004. Zircon (U-Th)/He thermochronometry: He diffusion and comparisons with $^{40}Ar/^{39}Ar$ dating. *Geochim. Cosmochim. Acta.* 68:1857-1887.

Reiners, P. W. 2005. Zircon (U-Th)/He thermochronometry. *Rev. Mineral. Geochem*. 58:151-179.

Renne P. R.; Swisher C. C.; Deino A. L.; Karner D. B.; Owens T. L.; DePaolo D. J. 1998. Intercalibration of standards, absolute ages and uncertainties in $^{40}Ar/^{39}Ar$ dating. *Chemical Geology*. 145:117-152.

Steiger, R. H.; Jäger, E. 1977. Subcommission on geochronology: convention on the use of decay constants in geo- and cosmochronology. *Earth. Planet. Sci. Let*. 36:359-362.

Appendix Supplementary Files

Tables

Table DR1: Zircon (U-Th)/He data
Table DR2: Apatite (U-Th)/He data
Table DR3: X-ray micro-computed tomography data
Table DR4: Raman spectroscopy data
Table DR5: $^{40}Ar/^{39}Ar$ geochronology data

Figures

Figure DR1: Individual zircon (U-Th)/He age vs eU plots
Figure DR2: Individual apatite (U-Th)/He age-eU plot
Figure DR3: Individual raman $v3SiO_4$ vs FWHM and eU concentration plots
Figure DR4: Individual zircon (U-Th)/He age, Raman, eU plots for all samples
Figure DR5: Individual rift flank numerical models
Figure DR6: Multi-sample models for Ottawa Embayment samples from locations 03 and 04
Figure DR7: $^{40}Ar/^{39}Ar$ geochronology spectra

Data Repository Table 1: Zircon (U-Th)/He data for the Rift Flank and Ottawa Embayment

	rs[a] (mm)	4He (nmol/g)	U (ppm)	Th (ppm)	eU (ppm)	Ft[b]	Raw Date (Ma)	Corrected Date (Ma)	Error[c] (Ma)
Rift Flank Samples									
02RH: quartzofeldspathic orthogneiss (876 m; 18T0534520, 5118677)									
1	61	876.4	226.9	108.3	252.4	0.81	611	754	60
2	56	748.3	226.8	102.7	250.9	0.79	528	665	53
3	70	738.2	510.0	79.4	528.6	0.83	253	304	24
4	45	309.2	108.0	50.3	119.8	0.76	460	608	49
5	50	290.4	97.0	38.7	106.1	0.77	486	633	51
1[R]	70	464.9	982.3	407.1	1078.0	0.84	79	95	8
2[R]	75	296.5	92.7	43.1	102.9	0.85	510	598	48
3[R]	68	596.2	1436.6	753.9	1613.8	0.83	68	82	7
03RH: quartzofeldspathic orthogneiss (654m; 18T0533757, 5118357)									
1	57	659.8	768.8	131.2	799.6	0.80	151	190	15
2	55	675.8	299.1	45.2	309.7	0.79	391	494	40
3	61	572.1	268.2	104.0	292.6	0.81	352	435	35
4	57	488.2	388.7	42.2	398.7	0.80	223	279	22
5	44	1033.1	302.0	158.7	339.3	0.74	539	730	58
07RH: quartzofeldspathic orthogneiss (444m; 18T0532966, 5118101)									
1	56	451.9	262.3	51.2	274.3	0.79	298	375	30
2	82	289.1	153.6	65.5	168.9	0.86	309	361	29
3	64	279.4	110.9	43.2	121.1	0.82	413	505	40
4	44	416.0	185.2	68.9	201.4	0.74	371	500	40
5	49	248.1	98.1	38.5	107.1	0.78	414	532	43
012RH: quartzofeldspathic orthogneiss (234m; 18T0531679, 5117146)									
1	59	498.1	242.7	86.6	263.0	0.80	341	425	34
2	73	346.6	125.9	55.9	139.0	0.84	445	530	42
3	51	672.0	309.3	106.3	334.2	0.77	361	467	37
4	76	396.9	132.2	59.0	146.1	0.84	483	573	46
5	60	408.0	136.7	53.6	149.3	0.81	486	603	48
1[R]	64	588.0	316.6	83.8	336.3	0.82	315	382	31

2[R]	51	348.1	364.5	36.5	373.1	0.78	170	218	17
3[R]	49	348.3	123.2	56.0	136.4	0.77	455	586	47
014RH: granite (228m; 18T0516396, 5092503)									
1	67	407.1	142.9	50.2	154.7	0.83	468	567	45
2	45	413.9	292.9	102.1	316.9	0.75	237	318	25
3	43	299.3	224.2	39.4	233.5	0.74	233	316	25
4	49	325.2	228.8	84.2	248.6	0.77	238	311	25
5	38	327.2	302.5	27.0	308.9	0.70	193	274	22
010RH: quartz monzonite (553m; 18T0554095, 5130882)									
1	98	309.2	76.8	37.4	85.6	0.88	634	722	58
2	78	489.8	135.7	57.3	149.2	0.85	579	682	55
3	69	355.6	113.1	38.2	122.1	0.83	516	622	50
4	71	510.5	145.0	86.5	165.3	0.83	547	655	52
5	63	303.8	75.5	27.1	81.9	0.82	649	789	63
M_RH: amphibolite (205 m; 18T0497684, 5055405)									
1[R]	55	140.7	83.8	53.9	96.4	0.79	265	335	27
2[R]	66	223.8	86.0	37.4	94.8	0.82	422	513	41
3[R]	51	206.2	78.5	39.4	87.8	0.77	420	542	43
4[R]	54	207.2	79.6	42.0	89.5	0.78	414	528	42
5[R]	60	89.8	36.7	19.9	41.4	0.82	389	473	38

	rs[a] (mm)	4He (nmol/g)	U (ppm)	Th (ppm)	eU (ppm)	Ft[b]	Raw Date (Ma)	Corrected Date (Ma)	Error[c] (Ma)
Ottawa Embayment Samples									
01P_RH: muscovite-biotite metagranite (75 m; 18T0466714, 5043139)									
1	55	297.2	102.7	105.0	127.4	0.79	418	523	42
2	57	435.0	144.6	126.1	174.3	0.80	446	555	44
3	54	215.4	77.0	108.6	102.6	0.78	378	478	38
4	64	209.4	71.8	73.4	89.0	0.82	421	511	41
5	62	197.8	65.9	95.4	88.3	0.81	402	492	39
01S_RH: quartz arenite (75 m; 18T0466714, 5043139)									
1	64	284.9	99.1	125.1	128.5	0.82	398	483	39
2	61	41.0	25.7	63.3	40.6	0.80	185	229	18

3	42	183.9	67.8	80.0	86.6	0.72	381	520	42
4	44	180.6	79.4	70.8	96.0	0.74	339	452	36
5	64	221.0	95.6	69.4	111.9	0.82	355	431	34
02P_RH: biotite granitic gneiss (68 m; 18T0451413, 5036866)									
1	56	132.4	98.4	28.2	105.0	0.79	229	288	23
2	48	239.8	228.7	81.3	247.8	0.76	177	232	19
3	51	218.0	121.4	68.3	137.5	0.77	287	371	30
4	53	146.0	93.4	52.6	105.8	0.79	250	317	25
5	49	275.5	220.8	111.3	246.9	0.77	203	263	21
6	56	505.8	293.1	109.3	318.8	0.80	287	358	29
7	42	148.7	55.5	54.0	68.2	0.73	391	532	43
8	43	260.7	139.2	77.4	157.4	0.74	299	403	32
02S_RH: quartz arenite (68 m; 18T0451413, 5036866)									
1	67	212.2	63.7	34.2	71.7	0.82	525	636	51
2	58	331.8	98.9	76.6	116.8	0.80	505	632	51
3	73	108.6	36.3	31.9	43.8	0.84	443	529	42
4	58	512.6	334.2	203.6	382.0	0.80	244	302	24
5	61	328.0	89.8	65.5	105.2	0.81	551	672	54
6	71	374.5	138.4	96.6	161.1	0.84	416	494	40
7	52	132.5	55.8	73.2	73.0	0.78	328	418	33
8	65	158.6	79.5	66.0	95.0	0.82	302	366	29
03P_RH: biotite metagranite (65 m; 18T0446258, 5038386)									
1	77	355.8	334.1	90.5	355.4	0.85	183	216	17
2	68	413.1	232.7	159.8	270.3	0.83	277	335	27
3	68	371.1	393.2	323.2	469.1	0.83	145	176	14
4	69	291.6	219.6	102.9	243.8	0.83	218	262	21
5	66	181.8	97.1	116.3	124.4	0.82	265	321	26
6	69	240.0	188.9	251.5	248.1	0.83	177	213	17
7	70	435.1	202.8	126.6	232.6	0.83	337	401	32
8	86	240.4	187.7	97.7	210.6	0.87	208	240	19
03S_RH: quartz arenite (65 m; 18T0446258, 5038386)									
1	60	389.1	126.9	56.1	140.1	0.80	493	613	49
2	61	131.5	48.8	35.9	57.2	0.81	411	509	41
3	79	104.4	32.0	28.8	38.7	0.85	480	566	45

4	66	65.7	35.5	15.9	39.2	0.82	303	367	29
5	67	38.9	24.2	39.2	33.5	0.82	211	256	20
04P_RH: garnet-biotite metagranite to gneiss (130 m; 18T0405509, 4969027)									
1	76	318.6	105.0	96.7	127.7	0.84	446	529	42
2	44	253.3	122.9	35.1	131.1	0.74	347	467	37
3	54	255.4	293.7	133.6	325.1	0.79	144	183	15
4	50	269.0	160.3	53.9	173.0	0.77	281	364	29
5	49	361.2	138.0	29.6	145.0	0.77	444	579	46
04S_RH: quartz arenite (130 m; 18T0405509, 4969027)									
1	49	321.8	116.7	47.4	127.9	0.77	449	586	47
2	64	28.4	10.3	8.8	12.4	0.82	411	503	40
3	57	99.3	27.0	24.9	32.9	0.79	536	675	54
4	54	152.0	37.5	66.2	53.1	0.78	510	653	52
5	44	237.9	69.2	44.9	79.8	0.76	528	698	56

rs[a] - spherical radius

Ft[b] -alpha ejection correction of Farley et al. (1996)

Error[c]- 8% (2σ)analytical uncertainty (Reiners et al., 2004)

Data Repository Table 2: Apatite (U-Th)/He data for the Rift Flank and Ottawa Embayment

	rs[a] (mm)	4He (nmol/g)	U (ppm)	Th (ppm)	Sm (ppm)	eU (ppm)	Ft[b]	Raw Date (Ma)	Corrected Date (Ma)	Error[c] (Ma)
Rift Flank Samples										
02RH:quartzofeldspathic orthogneiss (876 m; 18T0534520, 5118677)										
1	61	5.0	2.4	7.0	54.8	4.1	0.725	202	278	23
2	56	3.4	2.2	3.3	40.4	2.9	0.707	190	269	23
3	43	10.0	5.5	9.0	99.5	7.6	0.627	216	344	45
4	39	7.3	5.2	3.2	83.3	5.9	0.598	202	338	62
5	47	34.9	14.3	150.8	107.4	49.8	0.634	126	199	19
03RH: quartzofeldspathic orthogneiss (654m; 18T0533757, 5118357)										
2	55	1.9	2.1	0.0	35.4	2.1	0.709	140	197	22
3	61	3.5	3.9	2.9	39.5	4.5	0.731	132	180	16
4	57	1.3	0.8	0.0	28.1	0.8	0.714	219	306	47
5	44	11.7	5.9	18.0	72.0	10.1	0.62	200	323	50
07RH: quartzofeldspathic orthogneiss (444m; 18T0532966, 5118101)										
3	43	6.4	4.1	23.9	152.3	9.7	0.638	107	168	20
4	40	17.2	5.7	46.1	192.2	16.5	0.582	174	299	42
5	55	54.4	15.0	113.1	114.7	41.6	0.687	233	339	24
1	47	22.7	8.6	49.2	139.8	20.1	0.657	195	297	299
2	46	25.7	7.2	51.4	122.7	19.3	0.654	231	354	355
012RH: quartzofeldspathic orthogneiss (234m; 18T0531679, 5117146)										
1	44	18.8	12.2	82.7	126.7	31.6	0.64	106	165	18
2	51	24.5	17.9	51.9	104.0	30.1	0.696	145	208	16
3	52	18.7	8.6	59.4	111.4	22.6	0.694	146	210	16
4	54	38.8	16.7	77.4	91.7	34.9	0.711	199	279	21
5	44	37.6	26.6	182.4	147.5	69.5	0.642	98	152	17
014RH: meta-syenite (228m; 18T0516396, 5092503)										
1	66	0.2	0.0	0.0	0.1	0.0	0.749	69879	93338	5331089
2	57	0.0	0.0	0.0	0.3	0.0	0.735	2696	3666	51162
3	48	0.1	0.0	0.0	0.5	0.0	0.664	3936	5928	76910
4	75	0.4	0.0	0.0	0.1	0.0	0.779	52449	67329	1351682

5	69	0.1	0.0	0.1	0.2	0.0	0.778	285	367	515
M_RH: amphibolite (205 m; 18T0497684, 5055405).										
1	45	0.6	1.8	1.1	11.7	2.1	0.646	51	80	16
2	46	0.8	1.4	4.6	14.4	2.4	0.642	57	89	12
3	43	2.4	6.7	7.7	15.8	8.5	0.631	51	81	10
4	61	1.8	3.2	1.0	13.4	3.4	0.733	92	126	11
5	46	1.1	2.4	2.5	8.5	2.9	0.651	65	100	13

	rs[a] (mm)	4He (nmol/g)	U (ppm)	Th (ppm)	Sm (ppm)	eU (ppm)	Ft[b]	Raw Date (Ma)	Corrected Date (Ma)	Error[c] (Ma)
Ottawa Embayment Samples										
01P_RH: muscovite-biotite metagranite (75 m; 18T0466714, 5043139)										
1	39	3.1	5.4	22.5	8.3	10.7	0.587	53	91	12
2	42	37.7	37.9	150.7	34.3	73.3	0.611	94	154	18
3	46	3.3	2.7	18.0	39.9	7.0	0.634	82	130	12
4	43	23.7	39.1	22.9	29.4	44.5	0.632	97	154	22
5	41	4.6	4.4	25.7	13.1	10.4	0.592	81	137	21
01S_RH: quartz arenite (75 m; 18T0466714, 5043139)										
1	50	4.5	4.1	8.4	29.2	6.1	0.673	130	193	15
2	63	5.5	6.4	8.8	17.7	8.5	0.736	116	158	12
3	43	8.0	9.6	35.6	7.4	18.0	0.613	82	133	17
4	53	9.9	9.5	31.2	16.4	16.8	0.682	108	158	11
5	48	3.5	3.2	10.4	14.4	5.6	0.66	111	168	13

rs[a] - spherical radius

Ft[b] -alpha ejection correction of Farley et al. (1996)

Error[c]-1σ propogated error calculated using analytical uncertainties on U, Th, and He and grain length measurements

Data Repository Table 3: X-ray Micro-Computed Tomography Data

Grain #	Volume (mm^3)	Surface Area (mm^2)	^{238}U FT	^{235}U FT	^{232}Th FT	Mean CT FT*	Dimensional FT	Ft % Difference
002RH: quartzofeldspathic orthogneiss (876 m; 18T0534520, 5118677)								
1	0.0029	0.1214	0.848	0.826	0.822	0.843	0.837	-0.64
2	0.0027	0.1208	0.837	0.813	0.809	0.831	0.846	2.63
3	0.0009	0.0546	0.777	0.744	0.738	0.769	0.831	8.24
012RH: quartzofeldspathic orthogneiss (234m; 18T0531679, 5117146)								
1	0.0021	0.0950	0.834	0.809	0.805	0.828	0.821	-0.26
2	0.0011	0.0652	0.789	0.757	0.752	0.781	0.780	0.22
3	0.0012	0.0662	0.792	0.762	0.757	0.785	0.767	-1.10
01P_RH:muscovite-biotite metagranite (75 m; 18T0466714, 5043139)								
1	0.0011	0.0650	0.787	0.755	0.750	0.780	0.790	2.30
2	0.0017	0.0857	0.817	0.790	0.786	0.811	0.796	-0.90
3	0.0012	0.0688	0.787	0.754	0.749	0.779	0.783	1.36
4	0.0021	0.1003	0.827	0.800	0.796	0.821	0.818	0.41
5	0.0016	0.0772	0.822	0.795	0.791	0.816	0.811	0.13
01S_RH: quartz arenite (75 m; 18T0466714, 5043139)								
1	0.0019	0.0880	0.829	0.803	0.799	0.823	0.818	0.14
2	0.0015	0.0763	0.817	0.790	0.785	0.811	0.803	-0.61
3	0.0007	0.0461	0.748	0.710	0.704	0.739	0.725	-0.83
4	0.0007	0.0451	0.755	0.718	0.713	0.746	0.743	0.54
5	0.0018	0.0857	0.827	0.800	0.796	0.821	0.818	0.38
02P_RH: biotite granitic gneiss (68 m; 18T0451413, 5036866)								
1	0.0010	0.0584	0.797	0.767	0.762	0.790	0.795	0.62
2	0.0010	0.0592	0.785	0.753	0.748	0.777	0.762	-2.02
3	0.0009	0.0516	0.788	0.756	0.751	0.781	0.773	-0.93
4	0.0010	0.0585	0.796	0.765	0.761	0.789	0.786	0.17
5	0.0009	0.0544	0.787	0.756	0.751	0.780	0.769	-0.85
6	0.0013	0.0674	0.810	0.781	0.776	0.803	0.797	-0.08
7	0.0013	0.0816	0.768	0.733	0.728	0.760	0.726	-3.17
8	0.0007	0.0465	0.766	0.731	0.726	0.758	0.735	-2.08
02S_RH: quartz arenite (68 m; 18T0451413, 5036866)								
1	0.0023	0.1025	0.841	0.816	0.813	0.835	0.825	-1.23
2	0.0015	0.0785	0.808	0.777	0.773	0.801	0.798	-0.30
3	0.0023	0.1050	0.835	0.811	0.807	0.830	0.838	1.01
4	0.0015	0.0801	0.808	0.779	0.774	0.801	0.801	0.59
5	0.0015	0.0755	0.821	0.793	0.789	0.814	0.810	0.59
6	0.0022	0.0958	0.841	0.817	0.813	0.835	0.836	0.80
7	0.0012	0.0651	0.795	0.765	0.760	0.788	0.778	-0.58
8	0.0017	0.0801	0.829	0.803	0.800	0.823	0.821	0.30
03P_RH: biotite metagranite (65 m; 18T0446258, 5038386)								
1	0.0044	0.1732	0.858	0.836	0.833	0.853	0.847	-0.66
2	0.0027	0.1146	0.844	0.820	0.817	0.838	0.826	-1.52

3	0.0026	0.1142	0.845	0.822	0.818	0.839	0.825	-1.68
4	0.0022	0.0988	0.837	0.812	0.808	0.831	0.830	-0.09
5	0.0019	0.0881	0.832	0.807	0.803	0.827	0.822	-0.06
6	0.0021	0.1027	0.825	0.798	0.794	0.819	0.828	1.53
7	0.0026	0.1188	0.834	0.809	0.804	0.828	0.835	1.41
8	0.0039	0.1501	0.862	0.841	0.837	0.857	0.865	1.27
03S_RH: quartz arenite (65 m; 18T0446258, 5038386)								
1	0.0018	0.0833	0.826	0.801	0.797	0.821	0.805	-1.94
2	0.0017	0.0818	0.829	0.803	0.800	0.823	0.809	-1.80
3	0.0024	0.1016	0.846	0.822	0.819	0.840	0.849	1.00
4	0.0016	0.0782	0.823	0.797	0.793	0.817	0.824	0.80
5	0.0019	0.0871	0.832	0.806	0.802	0.826	0.823	0.05
04P_RH: garnet-biotite metagranite to gneiss (130 m; 18T0405509, 4969027)								
1	0.0035	0.1352	0.861	0.839	0.836	0.856	0.843	-1.48
2	0.0006	0.0410	0.760	0.724	0.719	0.752	0.744	-1.01
3	0.0011	0.0574	0.803	0.773	0.768	0.796	0.785	-1.39
4	0.0009	0.0512	0.790	0.758	0.753	0.782	0.773	-1.23
5	0.0009	0.0501	0.788	0.756	0.751	0.781	0.767	-1.74
04S_RH: quartz arenite (130 m; 18T0405509, 4969027)								
1	0.0016	0.0860	0.802	0.773	0.768	0.796	0.766	-3.75
2	0.0012	0.0676	0.803	0.773	0.768	0.796	0.817	2.62
3	0.0012	0.0641	0.807	0.778	0.773	0.800	0.793	-0.87
4	0.0010	0.0590	0.781	0.748	0.742	0.773	0.781	1.03
5	0.0007	0.0456	0.748	0.711	0.705	0.740	0.757	2.31
M_RH: quartz arenite (205 m; 18T0497684, 5055405)								
1	0.0009	0.0548	0.784	0.752	0.747	0.777	0.790	1.69
2	0.0022	0.1026	0.832	0.807	0.804	0.827	0.823	-0.39
3	0.0008	0.0500	0.767	0.731	0.726	0.759	0.775	2.02
5	0.0008	0.0494	0.781	0.747	0.742	0.774	0.822	6.33

*Mean CT FT: The weighted mean of 238U and 232Th, with the derived fraction of He as the weighing factor.

Data Repository Table 4: Raman Spectroscopy Data

Grain #[a]	V_3SiO_4 Peak (cm^{-1})	FWHM (cm^{-1})	V_1Si0_4 Peak (cm^{-1})	FHWM (cm^{-1})	Structural State[b]	V_3SiO_4 Variance
02RH: quartzofeldspathic orthogneiss (876 m; 18T0534520, 5118677)						
1a	1004.24	9.55	971.73	11.95	T	
1b	1003.29	9.60	971.27	13.70	T	
1μ	1003.76	9.58	971.50	12.83	T	0.45
2a	1005.86	5.77	972.84	3.75	C	
2b	1006.05	4.98	972.92	4.14	C	
2μ	1005.96	5.37	972.88	3.95	C	0.02
3a	1002.00	8.50	970.00	8.00	T	
3b	1003.97	4.38	971.35	4.15	T	
3μ	1002.99	6.44	970.68	6.07	T	1.94
012RH: quartzofeldspathic orthogneiss (234 m; 18T0531679, 5117146)						
1a	1005.03	4.87	972.15	3.26	C	
1b	1004.95	4.75	972.12	3.28	C	
1μ	1004.99	4.81	972.14	3.27	C	0.00
2a	1006.55	4.22	973.48	3.39	C	
2b	1006.05	3.40	973.17	2.54	C	
2μ	1006.30	3.81	973.32	2.96	C	0.13
3a	1005.71	4.86	972.80	3.39	C	
3b	1005.81	4.66	972.84	3.95	C	
3μ	1005.76	4.76	972.82	3.67	C	0.01
01P_RH: muscovite-biotite metagranite (75 m; 18T0466714, 5043139)						
1a	1005.30	6.75	972.21	5.15	C	
1b	1004.70	7.05	971.85	6.27	T	
1μ	1005.00	6.90	972.03	5.71	C	0.18
2a	1004.79	5.77	971.91	5.63	T	
2b	1005.20	6.04	972.18	5.73	C	
2μ	1005.00	5.90	972.04	5.68	C	0.08
3a	1005.76	4.77	972.72	3.69	C	
3b	1005.38	4.62	972.43	4.02	C	
3μ	1005.57	4.70	972.57	3.85	C	0.07
4a	1005.86	5.26	973.08	4.14	C	

4b	1006.32	5.92	973.17	3.49	C	
4μ	1006.09	5.59	973.13	3.82	C	0.11
5a	1006.49	4.02	973.49	3.01	VWC	
5b	1006.55	3.36	973.62	2.70	VWC	
5μ	1006.52	3.69	973.56	2.85	VWC	0.00
01S_RH: quartz arenite (75 m; 18T0466714, 5043139)						
1a	1005.25	5.42	972.39	4.31	C	
1b	1005.86	4.34	972.84	3.58	C	
1μ	1005.56	4.88	972.61	3.94	C	0.18
2a	1007.07	3.82	973.79	3.18	VWC	
2b	1007.04	3.80	973.75	3.24	VWC	
2μ	1007.06	3.81	973.77	3.21	VWC	0.00
3a	1006.25	3.55	973.25	3.25	C	
3b	1006.26	4.10	973.17	3.10	C	
3μ	1006.26	3.83	973.21	3.18	C	0.00
4a	1006.29	4.84	973.18	4.45	C	
4b	1006.29	4.64	973.16	3.85	C	
4μ	1006.29	4.74	973.17	4.15	C	0.00
5a	1006.17	5.49	973.07	4.26	C	
5b	1006.53	5.29	973.61	4.02	VWC	
5μ	1006.35	5.39	973.34	4.14	VWC	0.07
02P_RH: biotite granitic gneiss (68 m, 18T0451413, 5036866)						
1a	1004.00	8.50	971.50	7.50	T	0.18
1b	1004.61	7.47	971.55	10.22	T	
1μ	1004.30	7.99	971.53	8.86	T	0.18
2a	1004.00	9.00	971.50	7.50	T	
2b	1005.00	7.00	972.50	6.50	C	
2μ	1004.50	8.00	972.00	7.00	T	0.50
3a	1003.50	9.00	970.50	7.50	T	
3b	1003.50	8.50	970.50	7.50	T	
3μ	1003.50	8.75	970.50	7.50	T	0.00
4a	1006.00	5.00	973.00	4.50	C	
4b	1006.00	6.50	973.00	5.50	C	
4μ	1006.00	5.75	973.00	5.00	C	0.00

5a	1006.00	7.00	972.50	5.50	C	
5b	1007.00	8.00	973.50	7.00	VWC	
5µ	1006.50	7.50	973.00	6.25	VWC	0.50
6a	1003.36	13.03	970.15	9.36	T	
6b	1003.50	9.50	970.50	9.50	T	
6c	1003.50	9.50	971.50	10.00	T	
6µ	1003.45	10.68	970.72	9.62	T	0.01
7a	1007.00	5.00	974.00	4.00	VWC	
7b	1007.00	5.50	973.50	4.00	VWC	
7µ	1007.00	5.25	973.75	4.00	VWC	0.00
8a	1005.00	7.00	972.00	6.00	C	
8b	1005.50	6.50	972.50	6.50	C	
8µ	1005.25	6.75	972.25	6.25	C	0.13
02S_RH: quartz arenite (68 m; 18T0451413, 5036866)						
1a	1007.28	3.56	973.96	3.01	VWC	
1b	1006.14	5.28	972.91	8.44	C	
1µ	1006.71	4.42	973.43	5.72	VWC	0.65
2a	1004.39	7.81	971.66	5.24	T	
2b	1003.50	7.00	971.00	6.00	T	
2µ	1003.94	7.41	971.33	5.62	T	0.39
3a	1006.42	3.21	973.42	2.19	C	
3b	1006.37	4.22	973.35	3.35	C	
3µ	1006.39	3.71	973.39	2.77	C	0.00
4a	1001.74	9.57	970.00	9.81	T	
4b	1001.85	9.56	969.90	10.29	T	
4µ	1001.80	9.57	969.95	10.05	T	0.01
5a	1005.56	6.03	972.62	4.86	C	
5b	1005.50	7.50	972.50	6.50	C	
5µ	1005.53	6.77	972.56	5.68	C	0.00
6a	1006.28	5.98	972.66	6.20	C	
6b	1004.67	7.95	971.82	8.54	T	
6µ	1005.48	6.97	972.24	7.37	T	1.30
7a	1006.84	4.95	973.70	3.79	VWC	
7b	1006.58	4.46	973.47	3.66	VWC	

7μ	1006.71	4.70	973.59	3.73	VWC	0.03
8a	1005.90	5.68	972.85	4.76	C	
8b	1005.78	5.92	972.61	5.41	C	
8μ	1005.84	5.80	972.73	5.08	C	0.01
03P_RH: biotite metagranite (65 m; 18T0446258, 5038386)						
1a	1002.25	11.50	968.82	44.55	T	
1b	1004.69	13.47	X	0.00	T	
1μ	1003.47	12.48	968.82	22.27	T	2.97
2a	1002.28	14.72	X	0.00	T	
2b	1000.33	13.26	966.45	42.20	M	
2μ	1001.30	13.99	966.45	21.10	T	1.90
3a	1001.84	11.96	969.95	26.10	T	
3b	1001.83	12.49	966.76	53.46	T	
3μ	1001.84	12.23	968.36	39.78	T	0.00
4a	1002.67	14.82	967.82	36.28	T	
4b	1002.80	11.71	965.33	57.39	T	
4μ	1002.74	13.27	966.58	46.83	T	0.01
5a	1005.76	4.96	973.11	4.18	C	
5b	1006.20	4.78	973.25	3.50	C	
5μ	1005.98	4.87	973.18	3.84	C	0.10
6a	1004.30	8.70	971.96	9.24	T	
6b	1003.49	9.90	958.58	70.74	T	
6μ	1003.90	9.30	965.27	39.99	T	0.32
7a	1003.81	7.74	971.21	5.75	T	
7b	1005.44	5.51	972.97	3.40	C	
7μ	1004.63	6.63	972.09	4.58	T	1.33
8a	1005.79	4.73	972.97	3.47	C	
8b	1005.81	4.27	972.98	3.83	C	
8μ	1005.80	4.50	972.97	3.65	C	0.00
03S_RH: quartz arenite (65 m; 18T0446258, 5038386)						
1a	1005.11	7.57	972.92	4.91	C	
1b	1005.49	7.19	973.04	5.98	C	
1μ	1005.30	7.38	972.98	5.45	C	0.07
2a	1007.04	3.79	973.74	3.10	VWC	

2b	1007.17	3.17	973.94	2.17	VWC	
2μ	1007.10	3.48	973.84	2.63	VWC	0.01
3a	1006.92	4.01	973.72	2.89	VWC	
3b	1006.73	3.93	973.68	2.82	VWC	
3μ	1006.82	3.97	973.70	2.85	VWC	0.02
4a	1007.31	3.56	974.16	3.01	VWC	
4b	1007.06	4.34	973.85	2.94	VWC	
4μ	1007.19	3.95	974.01	2.98	VWC	0.03
5a	1007.28	3.56	973.96	3.01	VWC	
5b	1007.20	3.71	973.89	3.25	VWC	
5μ	1007.24	3.63	973.92	3.13	VWC	0.00
04P_RH: garnet-biotite metagranite to gneiss (130 m; 18T0405509, 4969027)						
1a	1005.42	5.83	972.68	5.16	C	
1b	1005.15	5.30	972.40	4.96	C	
1c	1004.54	6.73	968.55	4.95	T	
1d	1004.69	9.11	971.93	7.84	T	
1μ	1004.95	6.74	971.39	5.73	T	0.17
2a	1004.05	5.87	971.48	5.22	T	
2b	1004.91	8.20	972.07	7.75	T	
2μ	1004.48	7.03	971.77	6.49	T	0.38
3a	1006.24	7.70	973.24	5.55	C	
3b	1006.53	6.41	968.47	88.00	C	
3μ	1006.39	7.06	970.85	46.77	C	0.04
4a	1005.68	7.75	972.75	7.80	C	
4b	1006.21	5.76	973.08	4.94	C	
4μ	1005.95	6.75	972.91	6.37	C	0.14
5a	1004.97	6.39	972.34	6.12	T	
5b	1003.29	10.31	970.89	11.50	T	
5μ	1004.13	8.35	971.62	8.81	T	1.41
04S_RH: quartz arenite (130 m; 18T0405509, 4969027)						
1a	1005.45	4.67	972.56	3.87	C	
1b	1005.63	4.65	972.84	3.08	C	
1μ	1005.54	4.66	972.70	3.47	C	0.02
2a	1007.44	2.94	974.22	2.43	VWC	

2b	1007.50	2.54	974.25	1.97	VWC	
2μ	1007.47	2.74	974.23	2.20	VWC	0.00
3a	1006.22	4.42	973.07	3.22	C	
3b	1006.59	3.95	973.36	2.47	VWC	
3μ	1006.40	4.19	973.22	2.84	C	0.07
4a	1006.10	3.29	973.26	1.89	C	
4b	1006.08	4.20	973.19	2.64	C	
4μ	1006.09	3.74	973.22	2.26	C	0.00
5a	1005.28	5.63	972.50	4.23	C	
5b	1006.43	5.56	973.76	4.19	C	
5μ	1005.86	5.59	973.13	4.21	C	0.67
M_RH: quartz arenite (205 m; 18T0497684, 5055405)						
1a	1005.11	6.97	972.29	4.92	C	
1b	1005.62	4.79	972.81	4.25	C	
1μ	1005.36	5.88	972.55	4.59	C	0.13
2a	1005.00	6.23	972.20	5.44	C	
2b	1005.16	5.07	972.33	4.32	C	
2μ	1005.08	5.65	972.26	4.88	C	0.01
3a	1004.72	6.32	972.10	5.26	T	
3b	1005.29	6.38	972.51	5.90	C	
3μ	1005.01	6.35	972.31	5.58	C	0.16
4a	1004.99	5.82	972.52	4.27	T	
4b	1005.06	5.29	972.35	3.87	C	
4μ	1005.03	5.55	972.44	4.07	C	0.00
5a	1005.01	6.39	972.59	6.73	C	
5b	1006.29	4.26	973.37	3.54	C	
5μ	1005.65	5.32	972.98	5.13	C	0.82

Grain #[a]- μ indicates average spot measurement for grain

Structural State[b] -M-metamict, T-transitional, C-crystalline, VWC- very well crystalline

Table 5: Mont-Tremblant Rift Flank Biotite $^{40}Ar/^{39}Ar$ Data

Step	^{40}Ar (cps)	1σ (aps)	^{39}Ar (cps)	1σ (aps)	^{38}Ar (cps)	1σ (aps)	^{37}Ar (cps)	1σ (aps)	^{36}Ar (cps)	1σ (aps)	^{39}Ar % Total	% $(^{36}Ar)_{Ca}$	Ca/K	1σ (aps)	% $^{40}Ar^{*}$	Age (Ma)	1σ
Sample 04RH, 18T 533474, 5118249. Elevation 598 m, diabase, J= 21.323 + 0.06 x 10^{-3}, integrated age = 928 ± 4 Ma																	
A	105237	410	3401	6	38	8	77	13	18	2	1.35	0.12	0.04	0.01	94.76	876.16	4.71
B	190488	443	5857	8	69	9	63	13	1	2	2.33	2.40	0.02	0.00	99.89	949.49	2.80
C	236822	433	7406	9	91	7	45	12	3	2	2.94	0.40	0.01	0.00	99.60	934.96	2.22
D	86887	429	2754	6	37	7	5	12	1	2	1.09	0.26	0.00	0.01	99.81	926.71	5.68
E	360774	439	11231	10	151	8	12	12	10	2	4.46	0.03	0.00	0.00	99.19	935.26	1.52
F	121214	404	3771	7	62	9	-7	12	2	2	1.50	-0.09	0.00	0.01	99.48	937.76	4.14
G	403481	459	12721	12	178	11	12	12	3	2	5.06	0.12	0.00	0.00	99.79	930.45	1.43
H	935136	707	29683	19	429	14	42	13	5	2	11.80	0.25	0.00	0.00	99.85	925.93	0.83
I	1109383	815	35145	20	487	14	73	13	2	2	13.97	0.96	0.00	0.00	99.94	928.03	0.74
J	853292	684	27057	16	370	14	33	14	4	2	10.75	0.24	0.00	0.00	99.87	926.81	0.83
K	386047	471	12220	12	161	9	27	13	3	1	4.86	0.26	0.00	0.00	99.78	927.44	1.40
L	1199140	846	37987	21	538	19	28	14	4	2	15.10	0.22	0.00	0.00	99.91	927.82	0.71
M	933615	730	29633	16	432	12	34	13	5	2	11.78	0.17	0.00	0.00	99.83	925.79	0.80
N	525113	640	16708	21	237	8	6	13	1	2	6.64	0.25	0.00	0.00	99.96	925.02	1.46
O	36999	1796	1202	4	25	7	16	13	1	2	0.48	0.44	0.03	0.02	99.20	904.47	36.26
P	215513	430	6826	8	98	10	7	14	1	2	2.71	0.19	0.00	0.00	99.85	927.53	2.43
Q	19383	409	612	3	18	5	13	14	4	1	0.24	0.10	0.04	0.04	94.37	889.55	22.91
R	32983	477	975	4	21	5	25	13	2	1	0.39	0.32	0.05	0.03	98.06	965.30	15.08
S	66995	403	2123	5	51	5	21	14	3	1	0.84	0.18	0.02	0.01	98.61	917.99	6.66
T	137056	535	4305	7	55	8	14	14	2	1	1.71	0.23	0.01	0.01	99.62	931.89	3.85
Sample 06RH, 18T 533088, 5118136. Elevation 500 m, meta-granite, J= 21.288 + 0.06 x 10_{-3}, integrated age = 934 ± 4 Ma																	
E	11625	498	282	3	9	5	39	14	4	2	0.05	0.25	0.27	0.10	89.03	1040.53	57.94
F	5587	498	168	3	16	6	59	14	-4	2	0.03	-0.45	0.69	0.17	119.82	1107.35	95.76
G	11765	484	316	3	4	5	46	13	2	2	0.06	0.55	0.29	0.08	94.03	1003.88	53.40
H	51371	528	1468	7	31	5	43	14	6	2	0.27	0.21	0.06	0.02	96.66	978.57	12.51
I	44858	513	1342	6	22	7	-20	12	5	2	0.25	-0.12	-0.03	0.02	96.77	945.24	13.32
J	155569	571	4788	12	80	8	24	13	3	2	0.89	0.20	0.01	0.01	99.36	943.58	4.50
K	82683	494	2472	9	36	6	-9	13	3	2	0.46	-0.07	-0.01	0.01	98.77	960.62	7.28
L	4781040	2654	148646	72	2111	31	193	14	107	3	27.71	0.05	0.00	0.00	99.33	936.03	0.56
M	520188	614	16267	24	150	22	29	15	2	2	3.03	0.40	0.00	0.00	99.89	935.83	1.62
N	629243	666	19660	24	270	7	14	14	3	2	3.66	0.12	0.00	0.00	99.85	936.23	1.36
O	457592	644	14325	18	193	10	-13	13	2	2	2.67	-0.18	0.00	0.00	99.87	934.97	1.70
P	1303955	1086	40689	35	574	16	64	13	9	2	7.58	0.20	0.00	0.00	99.79	936.73	0.96
Q	1563456	1291	48984	40	676	12	-10	14	16	2	9.13	-0.02	0.00	0.00	99.69	933.05	0.90

R	1259732	1039	39504	37	537	11	-22	13	6	2	7.36	-0.10	0.00	0.00	99.85	933.57	0.96
S	4780615	3311	150162	72	2105	25	16	13	15	2	27.99	0.03	0.00	0.00	99.91	932.77	0.62
T	1513326	1446	47382	38	660	24	-27	13	3	2	8.83	-0.29	0.00	0.00	99.95	935.42	0.95
Sample 10RH-01, 18T 554111, 5130842. Elevation 553 m, quartz-monzonite, J= 21.252 + 0.06 x 10^{-3}, integrated age= 977 ± 4 Ma																	
A	72842	480	2833	9	77	8	8	14	20	2	1.59	0.01	0.01	0.01	91.70	732.65	7.43
B	157448	518	5016	10	120	8	9	14	5	2	2.81	0.06	0.00	0.01	99.12	915.63	3.85
C	431432	605	13319	19	275	14	11	14	6	2	7.46	0.05	0.00	0.00	99.58	941.83	1.86
D	344689	560	10371	16	221	7	56	13	-1	2	5.81	-2.12	0.01	0.00	100.07	964.42	2.11
E	841974	779	24851	21	519	16	118	14	2	2	13.93	1.56	0.01	0.00	99.93	977.83	1.08
F	326949	558	9767	18	185	10	57	14	-2	2	5.47	-0.64	0.01	0.00	100.23	971.04	2.29
G	144047	486	4203	11	105	9	23	13	-4	2	2.36	-0.18	0.01	0.01	100.75	992.83	4.23
H	492349	616	14464	19	301	20	85	14	3	2	8.11	0.79	0.01	0.00	99.82	980.57	1.60
I	782723	720	22987	23	470	16	82	14	7	2	12.88	0.31	0.01	0.00	99.72	980.06	1.16
J	276739	493	8185	14	176	10	30	14	1	2	4.59	0.74	0.01	0.00	99.88	975.93	2.36
K	69746	500	2064	7	52	8	-4	15	3	2	1.16	-0.04	0.00	0.01	98.61	965.84	8.42
L	171520	520	5021	11	108	10	20	13	-2	2	2.81	-0.26	0.01	0.01	100.38	987.46	3.90
M	346199	559	10228	18	169	22	31	13	-4	2	5.73	-0.22	0.01	0.00	100.34	980.17	2.24
N	160816	509	4685	11	107	9	27	12	-4	2	2.63	-0.20	0.01	0.01	100.69	993.48	4.18
O	500502	590	14758	19	339	21	25	13	-2	2	8.27	-0.29	0.00	0.00	100.15	980.24	1.59
P	535686	549	15860	20	319	9	20	13	2	2	8.89	0.37	0.00	0.00	99.92	975.41	1.48
Q	93563	446	2842	8	55	5	-22	12	-1	2	1.59	0.60	-0.02	0.01	100.32	959.18	6.17
R	114309	499	3409	9	72	5	9	13	0	2	1.91	0.93	0.00	0.01	99.94	970.10	5.39
S	82976	453	2489	9	35	7	5	12	2	2	1.39	0.08	0.00	0.01	99.36	961.45	7.56
T	37217	520	1077	6	26	8	12	12	-5	2	0.60	-0.07	0.02	0.02	104.07	1024.21	17.02
Sample 10RH-02, 18T 554111, 5130842. Elevation 553 m, quartz-monzonite ,J= 21.252 + 0.06 x 10^{-3}, integrated age= 973 ± 4 Ma																	
A	242906	571	9300	15	265	14	140	14	503	4	4.06	0.01	0.03	0.00	38.12	346.22	4.82
B	185197	572	6973	14	135	11	102	13	12	2	3.04	0.23	0.03	0.00	98.00	794.24	3.13
C	592662	676	19675	20	404	16	172	15	11	2	8.59	0.44	0.02	0.00	99.46	888.78	1.28
D	441548	592	13718	20	268	14	98	14	-2	2	5.99	-1.81	0.01	0.00	100.11	940.99	1.71
E	224992	471	6875	13	133	9	62	14	0	2	3.00	-10.47	0.02	0.00	100.03	952.69	2.70
F	532858	606	16145	20	335	13	74	15	3	2	7.05	0.62	0.01	0.00	99.82	957.36	1.48
G	274886	499	8289	14	178	13	50	15	-2	2	3.62	-0.69	0.01	0.00	100.23	963.96	2.43
H	915957	833	27305	28	622	20	159	15	1	2	11.92	4.19	0.01	0.00	99.97	970.64	1.12
I	602356	642	17963	20	369	16	59	14	0	2	7.84	7.01	0.01	0.00	99.99	970.53	1.33
J	590732	653	17416	23	359	11	48	14	0	2	7.60	-5.66	0.01	0.00	100.01	979.33	1.46
K	371308	556	11037	20	211	11	43	14	-2	2	4.82	-0.59	0.01	0.00	100.17	974.26	2.10
L	484552	574	14176	18	274	13	35	14	2	2	6.19	0.47	0.00	0.00	99.87	984.08	1.54
M	340762	534	9821	13	280	22	56	12	3	2	4.29	0.51	0.01	0.00	99.73	994.43	1.97
N	285168	519	8264	15	197	11	39	14	-2	2	3.61	-0.51	0.01	0.00	100.23	994.00	2.40

O	258633	536	7601	16	192	10	19	13	-2	2	3.32	-0.26	0.00	0.00	100.24	983.48	2.76
P	855740	776	25668	28	579	19	55	14	-1	2	11.21	-2.58	0.00	0.00	100.02	966.43	1.16
Q	196956	508	5958	12	102	13	34	14	-2	2	2.60	-0.47	0.01	0.00	100.31	962.32	3.05
R	50555	464	1552	6	-8	15	11	15	-3	2	0.68	-0.11	0.01	0.02	101.64	961.02	10.28
S	42751	499	1322	7	7	8	-2	15	-4	2	0.58	0.01	0.00	0.02	103.05	966.17	13.49
Sample 13RH-01, 18T 525751, 5102212. Elevation 203 m, augen-gneiss, J= 21.181 + 0.06 x 10^{-3}, integrated age = 940 ± 4 Ma																	
A	184907	558	9061	16	120	10	53	13	61	2	3.61	0.02	0.01	0.00	90.15	593.61	2.79
B	187102	563	6273	13	97	9	44	12	18	2	2.50	0.07	0.01	0.00	97.09	862.94	3.41
C	315091	577	10126	15	139	9	21	12	14	2	4.03	0.04	0.00	0.00	98.71	904.01	2.15
D	303571	522	9579	16	127	10	8	13	4	2	3.82	0.06	0.00	0.00	99.60	923.54	2.20
E	428564	586	13532	18	168	9	27	12	7	2	5.39	0.10	0.00	0.00	99.49	922.28	1.72
F	453942	576	14292	18	256	22	-3	11	5	2	5.69	-0.02	0.00	0.00	99.65	925.52	1.59
G	402843	581	12569	16	179	12	-5	13	0	2	5.01	0.42	0.00	0.00	100.03	934.83	1.77
H	765048	782	24085	25	301	17	67	12	0	2	9.59	10.57	0.01	0.00	99.99	928.09	1.18
I	620776	673	19148	24	272	13	47	13	1	2	7.63	1.73	0.00	0.00	99.96	942.78	1.37
J	338087	542	10468	18	87	24	28	12	-4	2	4.17	-0.20	0.01	0.00	100.35	942.84	2.03
K	306180	524	9419	16	107	14	25	12	-4	2	3.75	-0.19	0.01	0.00	100.37	947.73	2.21
L	366883	532	11172	18	154	16	19	12	4	2	4.45	0.14	0.00	0.00	99.68	950.14	1.94
M	499202	591	15110	23	206	13	17	13	2	2	6.02	0.20	0.00	0.00	99.86	955.94	1.66
N	432772	590	13161	20	182	11	18	13	-1	2	5.24	-0.38	0.00	0.00	100.09	954.17	1.77
O	383392	576	11714	20	158	7	-18	14	0	2	4.67	1.12	0.00	0.00	100.03	950.30	2.00
P	647601	699	19947	23	330	14	10	14	0	2	7.95	-0.83	0.00	0.00	100.02	944.21	1.36
Q	310080	539	9663	16	154	8	-5	13	5	2	3.85	-0.03	0.00	0.00	99.56	932.36	2.23
R	260636	550	8116	16	143	10	-17	13	4	2	3.23	-0.12	0.00	0.00	99.55	932.87	2.67
S	389370	544	12174	16	201	8	-12	14	-1	2	4.85	0.43	0.00	0.00	100.06	933.57	1.81
T	367822	542	11433	18	170	7	-4	14	-4	2	4.55	0.03	0.00	0.00	100.30	939.56	1.96
Sample 13RH-02, 18T 525751, 5102212. Elevation 203 m, augen-gneiss, J= 21.181 + 0.06 x 10^{-3}, integrated age = 929 ± 4 Ma																	
A	669507	641	27468	28	411	10	215	14	65	2	8.21	0.09	0.02	0.00	97.09	732.89	1.07
B	456298	563	14791	20	188	18	-3	14	-1	2	4.42	0.07	0.00	0.00	100.08	907.72	1.58
C	1144318	856	36364	35	474	13	54	15	4	2	10.86	0.43	0.00	0.00	99.91	920.70	0.94
D	694221	672	21818	21	299	16	17	13	-1	2	6.52	-0.54	0.00	0.00	100.04	929.64	1.17
E	619715	657	19191	25	260	11	34	13	-4	2	5.73	-0.23	0.00	0.00	100.20	941.64	1.40
F	508114	560	15847	20	226	14	57	15	-1	2	4.73	-1.15	0.01	0.00	100.08	935.54	1.47
G	179046	509	5584	12	76	6	31	13	-3	2	1.67	-0.29	0.01	0.00	100.50	938.57	3.46
H	209619	505	6571	13	124	19	49	13	-3	2	1.96	-0.47	0.01	0.00	100.42	934.35	2.96
I	764757	682	23431	24	330	11	26	13	2	2	7.00	0.37	0.00	0.00	99.92	947.43	1.12
J	513766	560	16083	20	219	14	3	13	3	2	4.81	0.03	0.00	0.00	99.82	930.90	1.44
K	640890	620	20083	24	250	10	19	13	-3	2	6.00	-0.18	0.00	0.00	100.13	932.50	1.28
L	466162	614	14698	23	188	13	-15	14	1	2	4.39	-0.29	0.00	0.00	99.91	926.33	1.71

M	661172	633	20783	21	277	13	-16	15	3	2	6.21	-0.16	0.00	0.00	99.88	928.37	1.19
N	541917	594	17171	19	219	11	-1	13	4	2	5.13	-0.01	0.00	0.00	99.78	921.86	1.36
O	530075	558	16878	23	219	10	23	14	5	2	5.04	0.14	0.00	0.00	99.74	918.05	1.44
P	525356	566	16787	21	219	10	1	14	1	2	5.02	0.04	0.00	0.00	99.94	916.95	1.44
Q	219236	523	6959	14	101	8	15	14	2	2	2.08	0.19	0.00	0.00	99.70	920.00	2.84
R	634310	648	20149	21	300	12	27	14	-1	2	6.02	-0.89	0.00	0.00	100.04	921.96	1.25
S	377400	577	11868	18	166	12	-1	13	-3	2	3.55	0.01	0.00	0.00	100.27	930.84	1.85
T	70224	503	2167	8	41	6	-15	13	-2	2	0.65	0.26	-0.01	0.01	100.66	947.48	8.63

Notes:

Measured isotopic abundances corrected for baseline, blank, and detector intercalibration. ^{39}Ar and ^{37}Ar are decay-corrected values.

Measured isotopic abundances are not corrected for nuclear interference reactions.

Samples were irradiated in the GSC Rad #68 sample can; irradiation duration 960 MWH, in medium-flux position 8C at McMaster Nuclear Reactor (Cd-shielded).

Decay constants and isotopic abundances after Steiger and Jäger (1977).

Ages calculated relative to PP20 hornblende flux monitor at 1074 ± 5 Ma (1σ, Jourdan et al., 2006)

Nucleogenic interference correction factors (±2σ):

$^{40}Ar^*$ = radiogenic argon

Rift Flank Samples

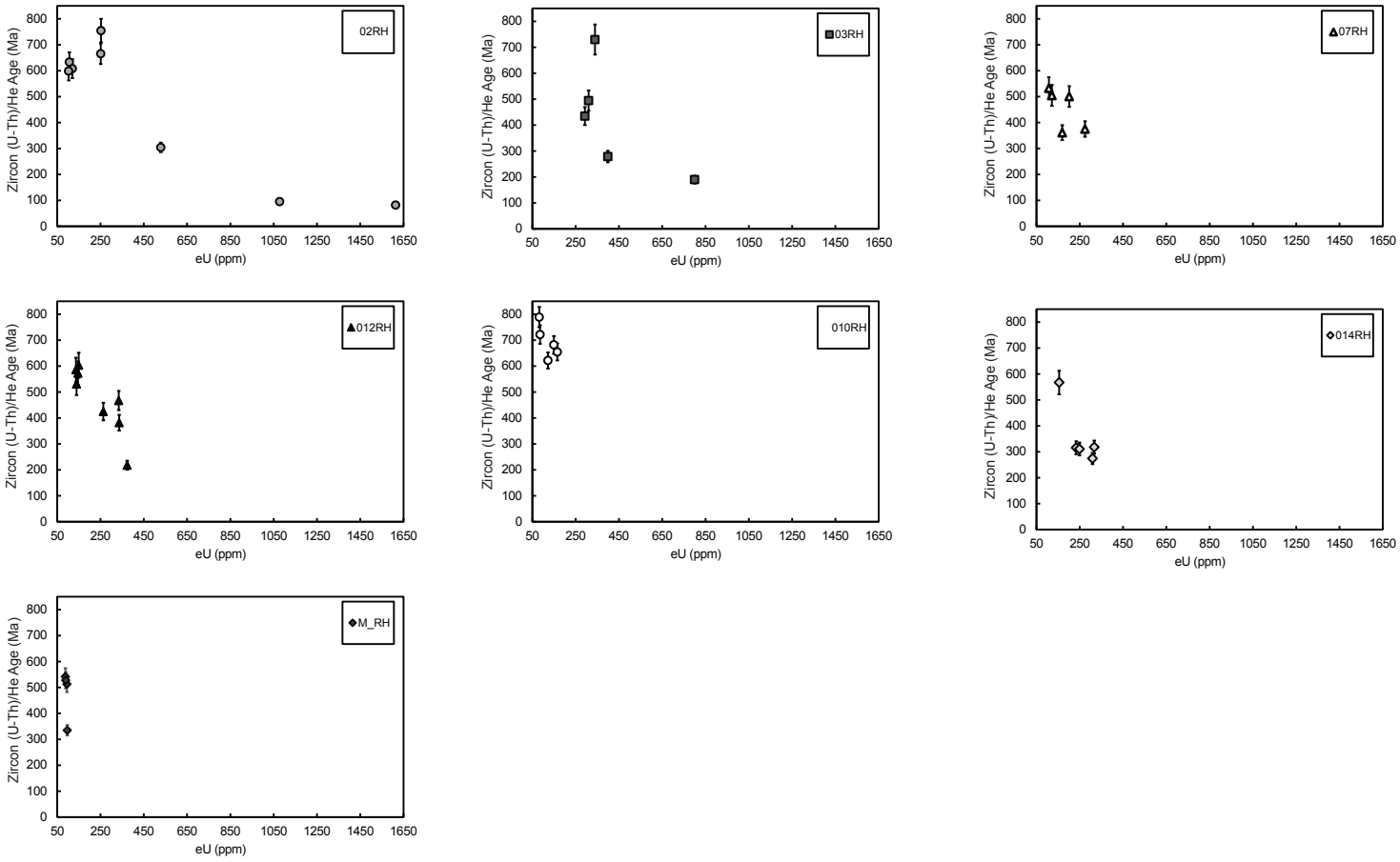

Ottawa Embayment Samples

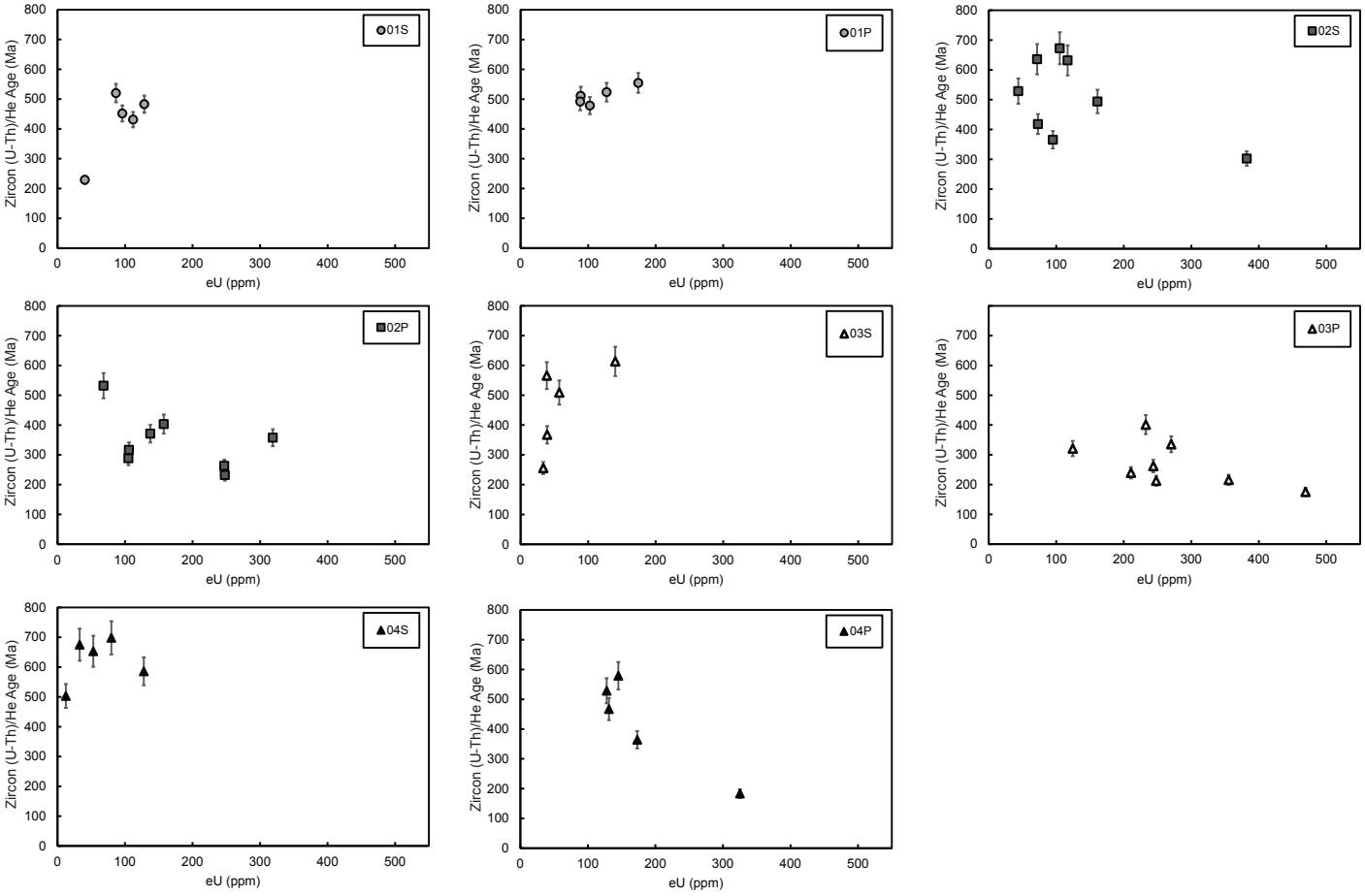

DR1: Zircon (U-Th)/He ages plotted against eU for individual samples from the rift flank and the Ottawa Embayment.

Rift Flank Samples

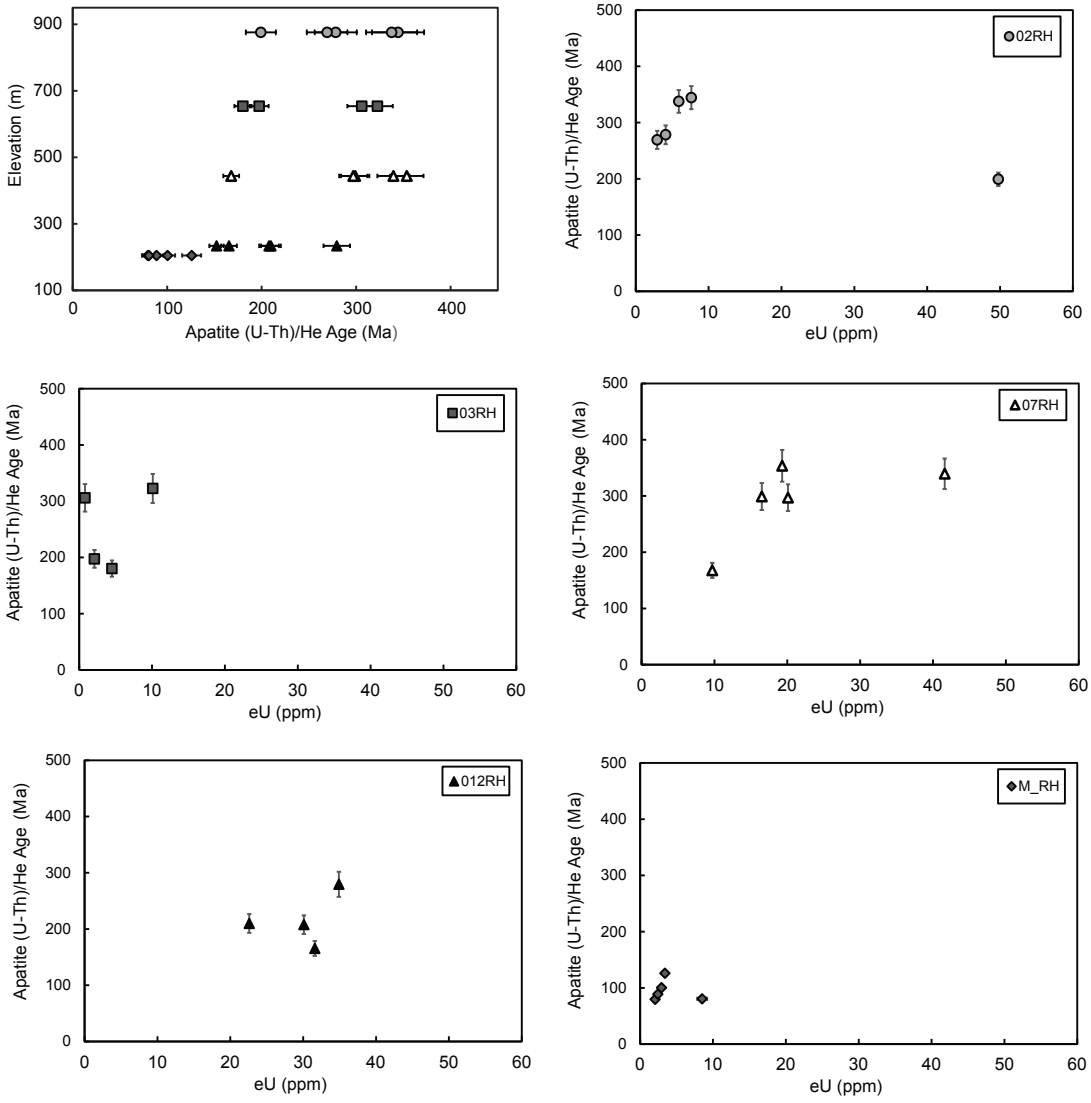

Ottawa Embayment Sample

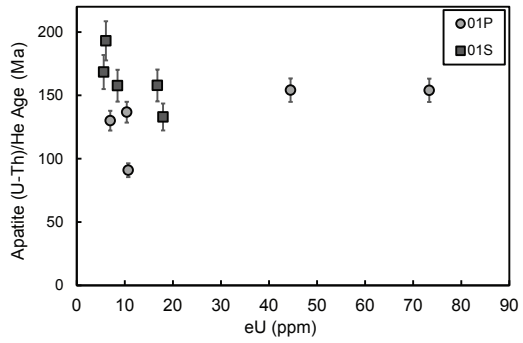

DR2: Rift flank apatite (U-Th)/He age-elevation plot (top left) and individual apatite (U-Th)/He ages plotted against eU for all rift flank and Ottawa Embayment samples containing apatite.

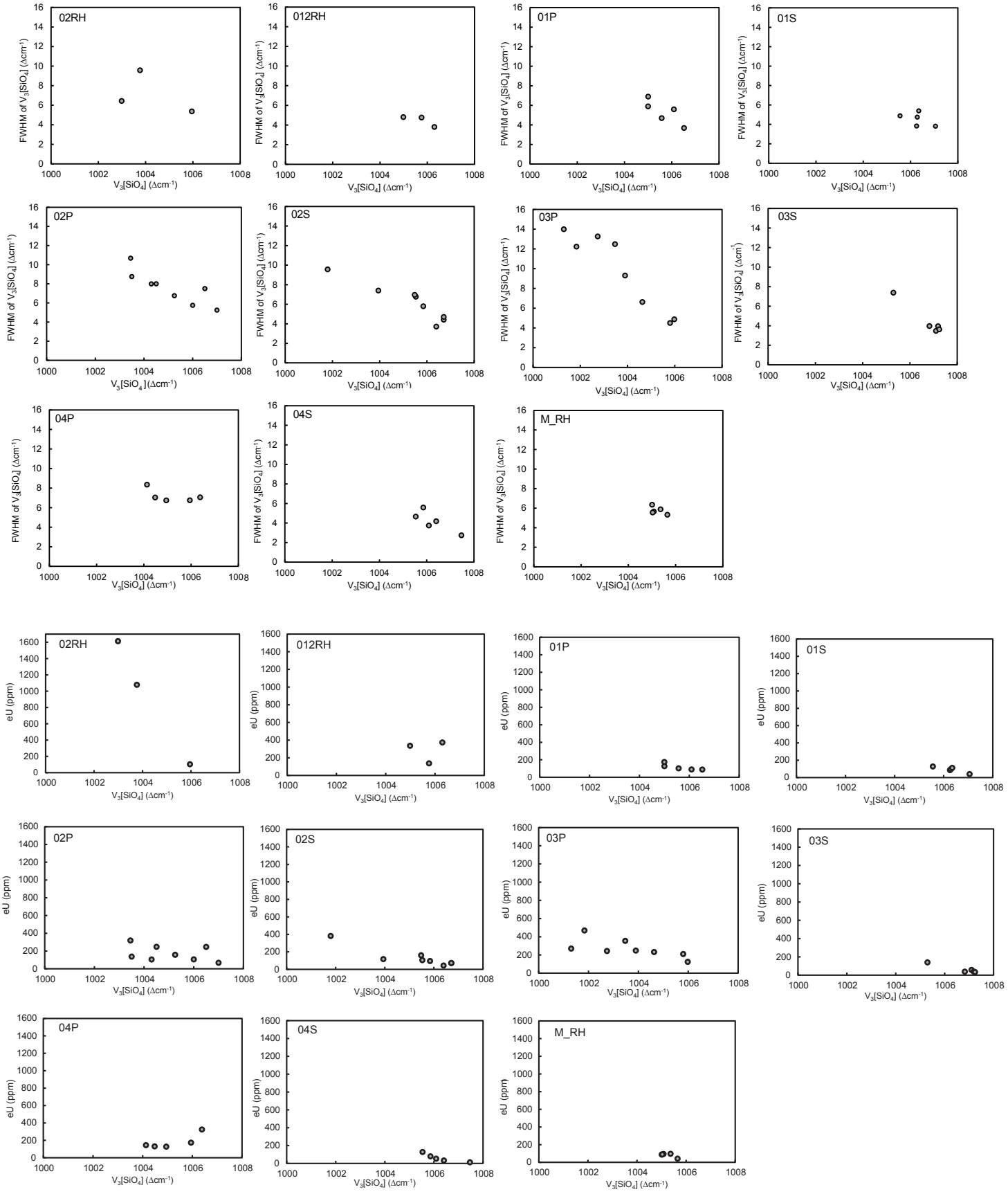

DR3: Zircon raman v_3SiO_4 peak frequencies plotted against their respective full-width-half-maximums (FWHM) and eU for individual samples from both the Ottawa Embayment (01P-04P and 01S-04S) and the rift flank (02RH and 012RH and M_RH).

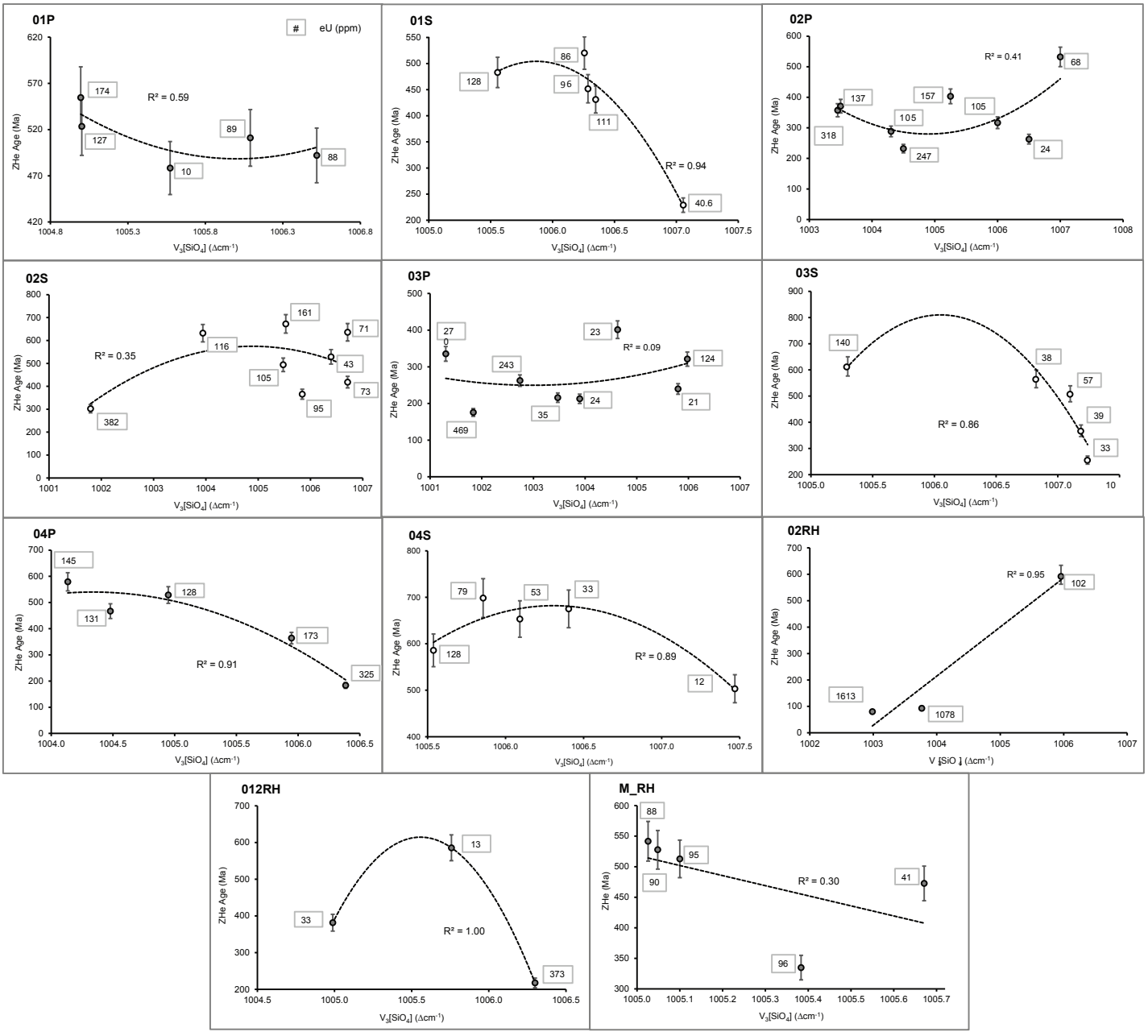

DR4: Zircon raman v_3SiO_4 peak frequencies plotted against (U-Th)/He ages for individual samples from both the Ottawa Embayment (01P-04P and 01S-04S) and the rift flank (02RH and 012RH and M_RH) along with their respective eU values.

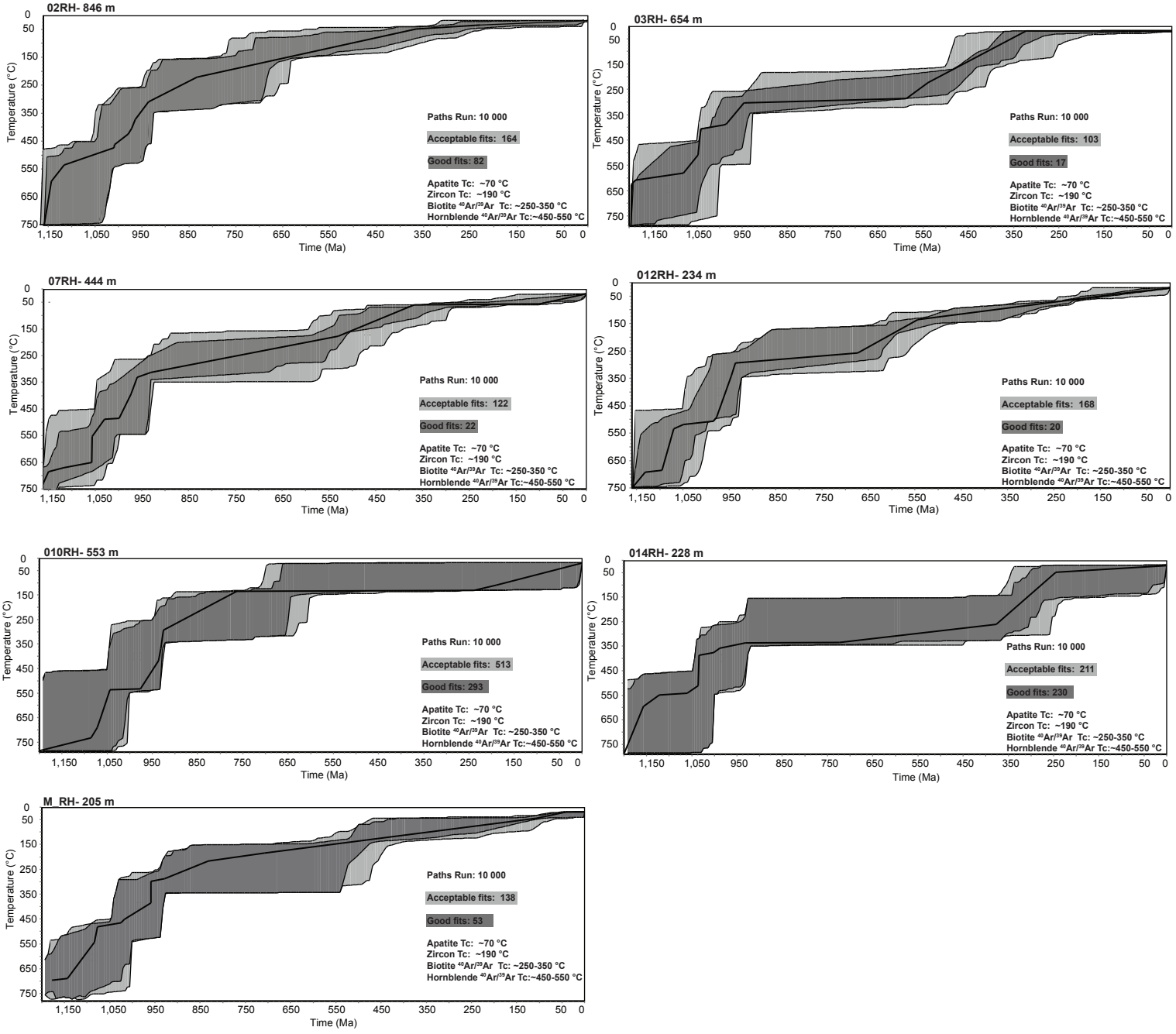

DR5: Inverse numerical models for individual rift flank samples.

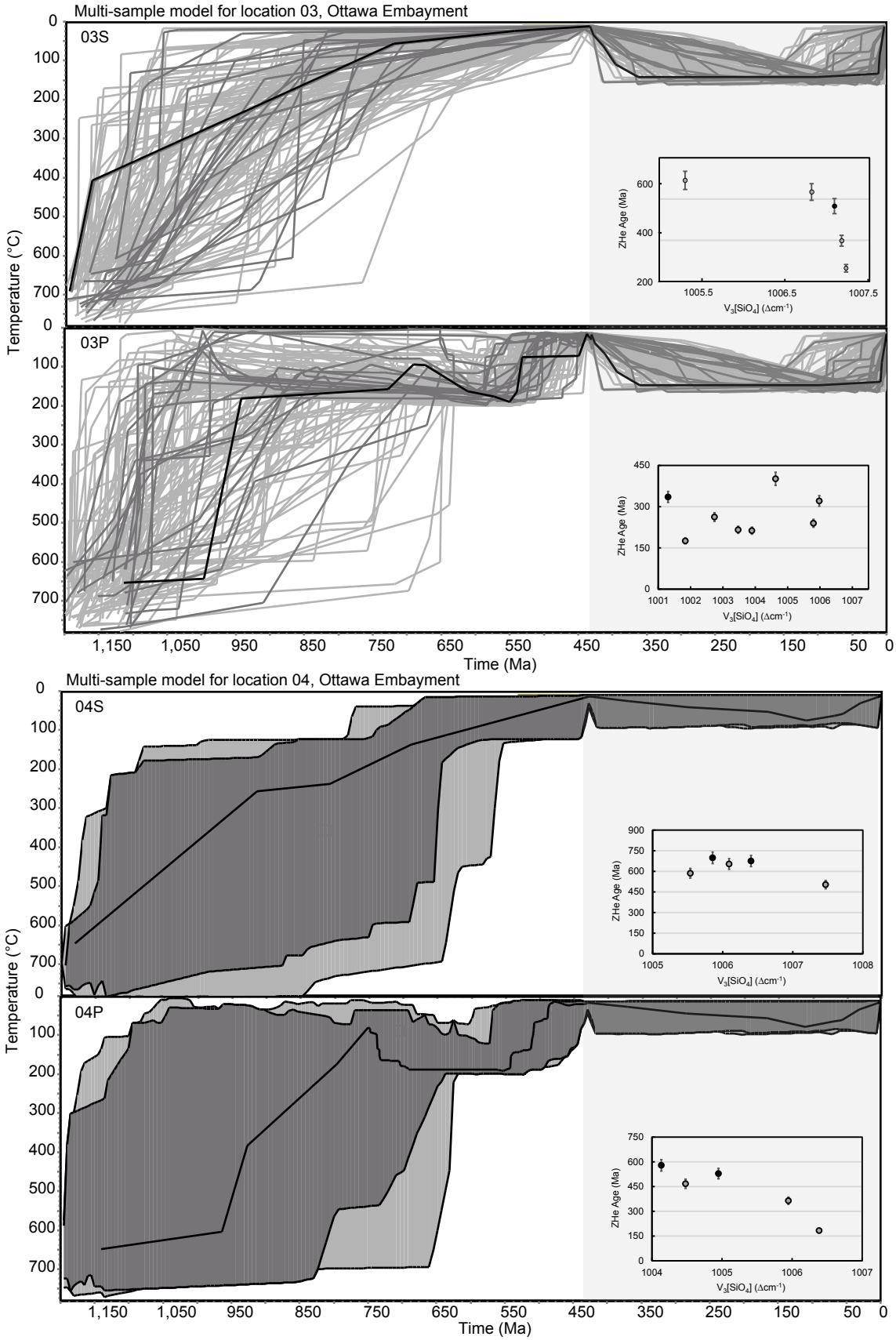

DR6: Inverse multi-sample numerical models for individual Ottawa Embayment samples (03-top, 04-bottom).

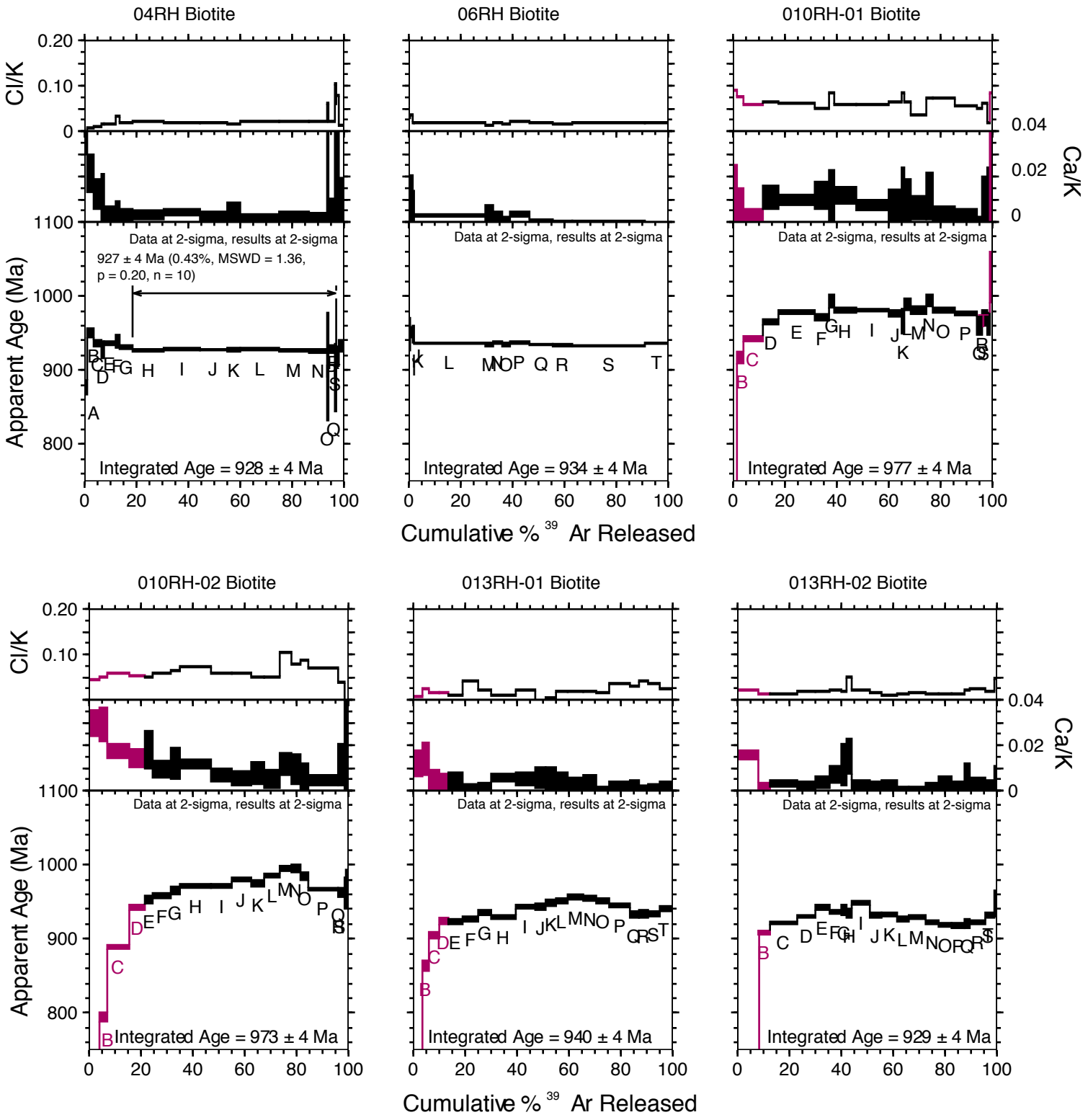

DR7: Ar^{40}/Ar^{30} geogchronology spectra for rift flank samples 04RH, 06RH, 010RH, 013RH.